MOVPE growth of InN analyzed by in-situ spectroscopic ellipsometry

vorgelegt von
Diplom-Chemiker

Massimo Drago

Turin

Von der Fakultät II - Mathematik und Naturwissenschaften

der Technischen Universität Berlin

zur Erlangung des akademischen Grades

Doktor der Naturwissenschaften
Dr. rer. nat.

genehmigte Dissertation

Promotionsausschuss:

Vorsitzender: Prof. Dr. E. Sedlmayr
Berichter/Gutachter: Prof. Dr. M. Kneissl
Berichter/Gutachter: Prof. Dr. W. Richter

Tag der wissenschaftlichen Aussprache: 23. Oktober 2006

Berlin 2007

D 83

Contents

1 Introduction **1**

2 In-situ Spectroscopic Ellipsometry in MOVPE **3**
2.1 Brief theoretical background . . . 3
2.1.1 Basic principle of ellipsometry . . . 3
2.1.2 Dielectric function . . . 5
2.1.3 A classical dispersion model: Lorentz . . . 6
2.1.4 Kramers-Kronig relations . . . 8
2.2 Analysis of real samples . . . 8
2.2.1 Multilayered samples . . . 8
2.2.2 Inhomogeneous layers: effective medium approximation . . . 8
2.3 Ellipsometric measurements on unknown materials . . . 10
2.4 MOVPE and ellipsometry set-up . . . 11
2.5 Ellipsometry used in-situ . . . 14
2.5.1 Surface sensitivity . . . 14
2.5.2 High temperature dielectric function . . . 16
2.6 Ellipsometry on InN/sapphire samples . . . 16

3 Indium Nitride: state of the art **19**
3.1 Properties . . . 19
3.1.1 Structural properties . . . 20
3.1.2 Optical properties and fundamental bandgap . . . 22
3.1.3 Electronic properties . . . 25
3.2 Growth of Indium Nitride . . . 28
3.2.1 Main reference for InN: GaN epitaxy . . . 28
3.2.2 Epitaxy of InN on sapphire substrates . . . 30
3.2.3 MOVPE of InN . . . 31
3.2.4 MBE of InN . . . 35
3.3 The initial growth procedure . . . 35

4 Morphology issues **37**
4.1 Layer peeling off . . . 37
4.2 Parasitic nucleation and droplets formation . . . 44
4.3 Chapter summary . . . 45

5 Thermal stability and annealing **47**
5.1 Thermal stability in different gas ambients . . . 47
5.1.1 Nitrogen ambient . . . 47
5.1.2 Hydrogen ambient . . . 48

5.1.3 Ammonia ambient . . . 49
5.2 Annealing in nitrogen . . . 51
5.3 Chapter summary . . . 57

6 Substrate preparation: nitridation of sapphire 59
6.1 Nitridation at 1050°C . . . 59
6.2 Nitridation kinetics . . . 65
6.2.1 Variations of ammonia partial pressure . . . 65
6.2.2 Variations of temperature . . . 67
6.3 Sapphire nitridation for InN growth . . . 70
6.4 Chapter Summary . . . 75

7 Nucleation and growth 77
7.1 Nucleation . . . 77
7.2 Growth rate . . . 79
7.3 Effects of growth temperature on crystal textures . . . 80
7.4 Optimizing growth . . . 82
7.5 Growth with low ammonia flow . . . 86
7.6 Growth on GaN nucleation layers . . . 87
7.7 Chapter Summary . . . 91

8 Dielectric function 93
8.1 Room temperature dielectric function . . . 93
8.2 Effects of roughness and metallic In . . . 95
8.3 High-temperature dielectric function . . . 97
8.4 Examples . . . 102
8.5 Chapter summary . . . 102

9 Summary 105

A Extrapolation of the InN dielectric function 107
A.1 Evaluation of the measured spectra . . . 107
A.2 Estimation of roughness . . . 110
A.3 Effects of the InN/sapphire interface . . . 110
A.4 Extrapolation . . . 112
A.4.1 Approach I: line shaping of ε_2 . . . 112
A.4.2 Approach II: harmonic oscillators for ε_2 . . . 113
A.4.3 Approach III: Effects of the fundamental bandgap . . . 114
A.5 Summary . . . 115

Acknowledgements 117

Bibliography 119

1. Introduction

Research and technological advancements in electronic materials have modified, in the last 50 years, our views, our attitudes and our way of living. Tools and gadgets like personal computers, mobile phones and LEDs are just examples of vast numbers of electronic devices that have contributed to the so called *electronic revolution*. In this context, the nitride based LEDs and laser diodes are vivid examples: the *blue light* was the result of a technological breakthrough in 1994 and caused a revolution in optoelectronics.

Epitaxial film technology was well established for several material systems, red and green LEDs were already available since the mid-seventies. Considerable efforts were then put into producing a marketable (with high efficiency and long lifetime) blue/violet emitting diode. Most of the efforts were dedicated in the direction of the II/VI compounds. Surprisingly for most, the first (and only, up to now) efficient blue light emitting diode was based on InGaN thin film technology. The breakthrough had an impact on every day life: wide screen multicolor displays, blue and (with phosphors) white LED for illumination (especially in the automotive sector), even green LEDs and new LED-based traffic lights invaded all cities very soon. Recently, SONY has commercialized an LED-based television and the *blue ray* compact disc technology, with a strong increase in the information that can be stored. The foreseeable improvements in power, in the emitting surface of the diodes and in the color of the emitted light (still too *artificial*) will lead to the substitution of the standard tungsten lamp for illumination: our houses will be soon illuminated by LEDs, that are brighter and more energy saving.

At the time of the discovery, basic research on nitride semiconductors was not as advanced as for the other standard III/V (i.e. arsenides, phosphides). After the first commercial InGaN-based blue LED, scientific research on nitrides has dramatically increased, with a strong scientific interest arising from the technological breakthrough.

The bandgap of GaN lies in the ultraviolet. In order to produce green and blue LEDs one needs to incorporate Indium in an alloy with GaN. By increasing Indium in the InGaN alloy, one has to face several problems which generally leads to the detriment of the grown layer and to a drop of the device performance. By completely replacing Gallium with Indium, one ends up in a binary material which is very difficult to grow: InN. For almost 10 years since the GaN breakthrough, its *cousin* InN received very little attention and very little was known about it mostly because of the difficulty in producing single crystalline, uniform material. At that point, the most often reported value for the fundamental bandgap of InN was 1.9 eV [1], measured in 1986. Quite late in the history of semiconductors, in 2002 it was suggested that the bandgap of InN is actually less than half (0.8 eV in [2], more recently 0.67 eV in [3]) than what was commonly accepted! A growing scientific community has gathered in the last 3 years to study this virtually new, and therefore exciting material also

because of the possibilities InN gives in terms of technological applications. Beside optoelectronics and multi-junction solar cells in InGaN alloys [4, 5], binary InN is very promising also for high energy, high power electronic devices [3, 6]. Scientific knowledge and the understanding of the material properties is being accumulated at this moment, before any InN based device is operative and this is obviously expected to be a strong catalyst for technological breakthrough.

How could it happen that a basic semiconductor property was so much overestimated for more than 20 years and is even now a matter of discussion? The main reason lies in the materials that were available for investigation. As mentioned, only very recently (last 5 years) single crystalline InN thin films exist, grown with either Molecular Beam Epitaxy (MBE) or Metal-Organic Vapour Phase Epitaxy (MOVPE), while free standing crystals are not yet available.

Understanding of the growth process of a new material is not only necessary in order to study the material properties but it is also important in order to produce a working electronic device. The technique already in use for all the GaN based technology is MOVPE. The state of the art of the InN layers grown by MOVPE, at the start of this work, was characterized by several issues. The layers were still very thin (about 100 nm) and, when grown thicker, deep holes with lateral size of some micrometers were forming. Basic properties like thermal and chemical stability as well as the growth dynamics were still unknown.

In this exciting frame, this work has the aim to study the fundamental steps and issues related to the growth of InN in MOVPE. To accomplish this, predominantly in-situ optical control with spectroscopic ellipsometry (SE) is used, which provides a valuable tool in order to understand the dynamics of the growth process.

The experimental methods and the state of the art for InN are discussed in the first two chapters. The first chapter will report on the characterization method (spectroscopic ellipsometry) and briefly with the growth method (MOVPE), while Chapter 2 deals with InN properties, providing the necessary background on the material. The results are outlined in Chapter 4-8. Chapter 4 outlines issues related to the morphology of MOVPE InN layers. Chapter 5 deals with thermal stability of InN. It provides the basic knowledge which is necessary in order to develop a successful growth strategy for InN. Chapter 6 deals with the first step of epitaxy of InN on sapphire: the nitridation of the sapphire substrate. Nitridation of sapphire is studied in-situ with ellipsometry, leading to the best nitridation procedure for epitaxy of InN layers. Chapter 7 deals with the development of an optimal strategy for growth of layers with improved properties. Chapter 8 deals with the optical properties of InN between 1.6 and 6.4 eV, developing a model for the dielectric function based on analysis of the properties of MOVPE grown InN layers. Details of the development of the model are given in the Appendix. Chapter 9 summarizes the results of this work.

2. In-situ Spectroscopic Ellipsometry in MOVPE

This chapter deals with the experimental methods used in this work: spectroscopic ellipsometry (SE) will be the focus, with a view also on the MOVPE technique and on the implementation of ellipsometry during epitaxy. Investigations on the dynamics of epitaxy are the key to understand and to improve growth. In-situ studies of epitaxial growth are the most appropriate way to study growth dynamics. For this purpose, SE is a very powerful optical technique which can be used during MOVPE of nitides.

The main aim of this chapter is to introduce tools which are necessary for in-situ optical investigation during growth of a compound semiconductor. For this reason, a brief theoretical introduction in optics and ellipsometry is necessary and the basic tools of *optical modelling* [7] will be also treated here. The problem of measuring optical properties on a unknown material with the intent of improving its growth will be also discussed. The experimental set-up will be then shortly described and the tools necessary for investigating a material during growth will be presented. The last section outlines the criteria for the interpretation of in-situ ellipsometric measurements on InN/sapphire layers.

2.1 Brief theoretical background

2.1.1 Basic principle of ellipsometry

Maxwell's four equations express how electric charges produce electric fields (Gauss' law), the experimental absence of magnetic monopoles, how currents and changing electric fields produce magnetic fields (Ampere's law), and how changing magnetic fields produce electric fields (Faraday's law of induction). These mathematical relations connect the quantities $\underline{E}$ (electric field), $\underline{D}$ (dielectric displacement), $\underline{J}$ (current density), $\underline{B}$ (magnetic induction) and $\underline{H}$ (magnetic field) . The solution of the Maxwell equations for a plane wave propagating along the z-axis provides for the electric field $\underline{E}$:

$$\underline{E} = \mathbf{e}_x E_x e^{i(\underline{k}\cdot\underline{r}+\omega t)} + \mathbf{e}_y E_y e^{i(\underline{k}\cdot\underline{r}+\omega t+\Delta)} \tag{2.1}$$

where $\mathbf{e}_x$ and $\mathbf{e}_y$ are unity vectors parallel to the x-axis and to the y-axis, respectively, E_x and E_y are field amplitudes, $\underline{k}$ and $\underline{r}$ are the wave vector and the position vector, ω is the angular frequency, t is time. The angle Δ is the phase difference of the y-component (second term) with respect to the x-component.

Light is said to be polarized if the values E_x, E_y and Δ are univocally defined (and not statistically evenly distributed). The state of polarization of the light can be then defined by two angles, Δ and Ψ, where the latter is so defined:

$$\tan\Psi = \frac{E_x}{E_y} \tag{2.2}$$

The angle tanΨ measures the proportion of the amplitudes of the electric field components E_x and E_y. In this system of coordinates polarization of light is linear when E_x or E_y are zero, or when the phase shift Δ is zero. Circular polarization occurs for values of tanΨ=1 and $\Delta = n \cdot \frac{\pi}{2}$ (n=1,3,5...), for other values the polarization is elliptical.

When discussing ellipsometry, the plane of incidence is taken as reference and the axes x and y becomes p, parallel to the plane of incidence and s (from the German *senkrecht*) perpendicular.

The principle of ellipsometry is illustrated in Fig. 2.1. By reflecting a beam of light of known polarization (usually linear polarization) off a sample, and measuring the polarization change upon reflection (usually elliptical after reflection) SE measures the changes in polarization through the ellipsometric parameters tanΨ and cosΔ.

After reflection from the sample, the parameter tanΨ measures the proportion of the amplitudes of the electric field components E_p and E_s, which are related to the amplitude ratio of the reflection coefficients r_x and r_y. The parameter cosΔ is the phase shift between the two components induced by the reflection coefficients r_x and r_y. Ellipsometry is a specular optical technique (the angle of incidence equals the angle of reflection). The ellipsometric parameters are related to the optical properties of the material investigated through the complex reflectance ratio [9] ρ:

$$\rho = \frac{r_p}{r_s} = \tan\Psi \cdot \exp(i\Delta) \tag{2.3}$$

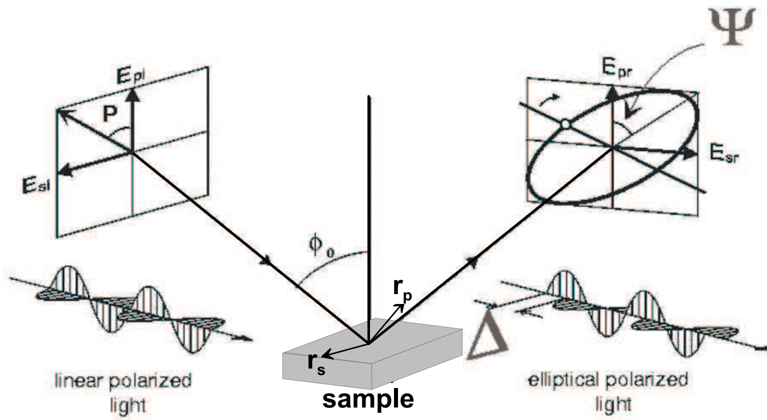

Figure 2.1: *Principle of ellipsometry. Linear polarized light changes upon reflection into, generally, elliptical polarized light. The change in polarization is defined by the reflection coefficients r_p and r_s. The latter are defined by the angle of incidence and by the optical properties of the sample. Figure taken from reference [8].*

Given ρ and ϕ_0 (the angle of incidence), the effective (or pseudo) dielectric function $\langle\epsilon\rangle$ is defined by ignoring the surface structure (reconstruction morphology, contamination, etc.) and can then be derived via the Fresnel equations:

$$\langle\epsilon\rangle = \sin^2\phi_0[1+(\frac{1-\rho}{1+\rho})^2\tan^2\phi_0] \tag{2.4}$$

This analytical process is also sometimes called "two phase model" since it takes into account only one interface (between phase I *vacuum* and phase II *sample*, neglecting any effect originating from the surface of the sample (reconstruction, contamination, roughness). Equation 2.4 is derived analytically and describes the optical properties of the sample, but it should not be confused with the *dielectric function* ε, which is defined for a material. The macroscopic origin of the dielectric function is given in the next subsection.

2.1.2 Dielectric function

The dielectric function is defined by the interaction of electromagnetic fields with matter by using the material equations [10]. For the materials investigated in this work the magnetic effects can be neglected. When an electric field $\underline{E}$ (like an electromagnetic wave) is applied to a dielectric, it causes a polarization $\underline{P}$. The result is a dielectric displacement $\underline{D}$:

$$\underline{D} = \varepsilon_0\underline{E} + \underline{P} \tag{2.5}$$

$\underline{P}$ is a function of $\underline{E}$ and can be expressed as its polynomial expansion using a set of dielectric susceptibilities χ_n as expansion terms. By neglecting all terms higher than the first order (linear optic approximation), one can write equation 2.5 as:

$$\underline{D} = \varepsilon_0\underline{E} + \varepsilon_0\chi\underline{E} \tag{2.6}$$

and by defining:

$$\varepsilon = 1 + \chi \tag{2.7}$$

we can finally write the expression for $\underline{\mathrm{D}}$ as:

$$\underline{D} = \varepsilon_0\varepsilon\underline{E} \tag{2.8}$$

In the simple case of materials which are isotropic in the bulk (i.e. cubic materials) ε is a complex function of energy: ε=ε_1+iε_2 with ε_1 being the real part and ε_2 the imaginary part. ε is also in simple relation with the complex diffraction index $\tilde{n}$, being:

$$\varepsilon = \tilde{n}^2 = n - i\kappa \tag{2.9}$$

$$\varepsilon_1 = n^2 - \kappa^2 \tag{2.10}$$

$$\varepsilon_2 = 2n\kappa \tag{2.11}$$

where n is the refraction coefficient and κ is the extinction coefficient.

In the more general case of non-isotropic materials, the dielectric function ε defined in equations 2.7 and 2.8 is a 3×3 tensor. In the case of wurtzitic materials (like the α-nitrides) the dielectric tensor becomes:

$$\tilde{\varepsilon} = \begin{pmatrix} \varepsilon_{xx} & 0 & 0 \\ 0 & \varepsilon_{yy} & 0 \\ 0 & 0 & \varepsilon_{zz} \end{pmatrix} = \begin{pmatrix} \varepsilon_e & 0 & 0 \\ 0 & \varepsilon_o & 0 \\ 0 & 0 & \varepsilon_o \end{pmatrix} \tag{2.12}$$

where ε_e is the extraordinary component of the dielectric tensor and ε_o is the ordinary component. In the case of this work, all measurements are carried out on the (0001) plane (c-plane) of InN and the projection of the extraordinary component on this surface is zero. The p-component of the incident electromagnetic wave in the ellipsometry sketch of Fig. 2.1 and at its respective reflection coefficient, r_p can be decomposed into two components. The one component is parallel to the surface plane, the other is perpendicular. The latter is in principle coupling with the extraordinary component of the dielectric tensor. In practice, the contribution of its interaction is negligible with respect to the contribution of the component parallel to the surface plane [9]. This means that only the ordinary component of the wurtzite InN can be measured.

2.1.3 A classical dispersion model: Lorentz

One of the most simple approaches to simulate the response of matter to an electromagnetic wave is to consider a single electron moving in the potential of a single ion. This leads to the Lorentz model, or harmonic oscillator model, which is used later in this work to simulate certain electronic transitions in InN. It is relevant anyway to mention that the situation in a crystal is more complicated.

The potential in a crystal is the periodic potential of the ions. Typically the one-electron approximation is still used and in a potential defined by Bloch waves the energy dispersion is calculated versus the k-vector in the Brillouin zone of the crystal structure. There are different possible approaches for calculating the band structure of a crystalline material, from semiempirical to *ab-initio* theories. The resulting band dispersion can be used to calculate the electronic transitions. Again several approaches are possible. The Joint Density of State model calculates for example the dielectric function as a sum of contributions from allowed interband transitions at specific points in the Brillouin zone, also called *critical points* of the Brillouin zone. The reader interested in further details is referred to [10].

The advantage of the Lorentz model is that it is very simple. Furthermore, the harmonic approximation serves in certain situations to efficiently fit electronic transitions occurring in semiconductors. Excitons, for example, have a Lorentz behaviour [10] and some band to band transitions are also fit best by Lorentz oscillators [11].

In the Lorentz model, we consider the electron in the parabolic potential of a single ion. The electron is interacting with an external electric field given by equation 2.1. It is also called Lorentz model and describes a damped, driven harmonic oscillator whose differential equation reads

$$m\ddot{x} + m\Gamma\dot{x} + m\omega_0^2 x = eE(\omega) \tag{2.13}$$

for one dimension, where x is here the position of the electron, m is the (effective) mass of the electron, Γ is the damping factor, ω_0 is the resonance frequency and E is the applied electric field. From equations 2.8 and 2.13 the dielectric function can be calculated and reads

$$\varepsilon(\omega) = 1 + \frac{\omega_p^2}{\omega_0^2 - \omega^2 - i\Gamma\omega}. \tag{2.14}$$

In the case of many electronic states, a linear combination of harmonic oscillator can be used, which leads to:

$$\varepsilon(\omega) = 1 + \omega_p^2 \sum f_j \frac{1}{\omega_j^2 - \omega^2 - i\Gamma_j\omega} \tag{2.15}$$

where

$$\sum f_j = 1 \tag{2.16}$$

In Fig. 2.2 different resonance frequencies ω_0 and different damping factors Γ produce different curves for the dielectric function. In particular, increasing damping factors result in increasing broadening. In a real system the damping might have

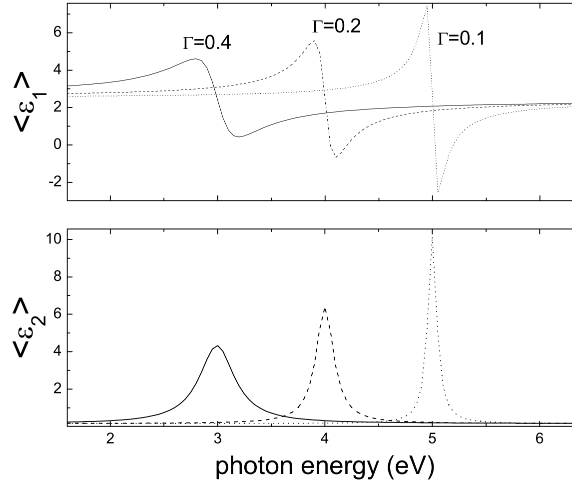

Figure 2.2: *The dielectric function of an harmonic (Lorentz) oscillator is calculated for different resonance energies (3 eV, 4 eV and 5 eV) and for different damping factors Γ (0.4, 0.2 and 0.1, respectively). Decreasing damping leads to sharper peaks.*

different origins, as for example increased temperature or presence of defects in the material.

2.1.4 Kramers-Kronig relations

By pure mathematical arguments (Cauchy-Riemann differential equations), it is possible to demonstrate that imaginary and real part of the dielectric function are dependent on each other, via the so called Kramers-Kronig relations (see for example [12]). In other terms, it is possible to calculate either the real or the imaginary part of a complex function when at least one of the two is known. ε_1 or ε_2 must be known for all photon energies. Due to the symmetry of the dielectric function one is allowed to perform the integration on the positive energies only. Consequently, the calculus can be completely successful only if one of the two parts is known over the whole energy range. A model for the dielectric function is called Kramers-Kronig consistent if it fulfills this relation.

2.2 Analysis of real samples

2.2.1 Multilayered samples

Heteroepitaxial growth creates, from the point of view of optics, a *multilayered* sample: the growing layer, the substrate and finally vacuum represents a 3-layered sample structure. Fig. 2.3 shows on the left the 2-layer model from which the effective dielectric function was calculated (equation 2.4), on the right the 3-layer model which can be applied in the case of heteroepitaxial growth. The bottom layer is always assumed to be semi-infinite, which means that, below, no other interface or surface contributes to the signal. This is realized in the case of an absorbing material which is thick enough to absorb all the light before it reaches the next surface/interface. As the figure shows, in the 3-layer model the electromagnetic wave goes through two interfaces and is reflected at the second interface. This can give rise to interferences with the light reflected at the vacuum/sample interface.

When the sample under investigation is composed of a larger number of layers the analytical solution becomes more complicated. The problem can be approached for example by decomposing the calculation in iterations of several 3-layer models. In Fig. 2.4 the calculation for a 6-layer model is schematically decomposed into 4 iterations. In the first iteration a 3-layer model calculates the effective dielectric function of the 2 bottom layers. The result is used in the second iteration as bottom layer in the new 3-layer model, where the 4th layer from the bottom is now also used. The iteration continues until in the last calculation vacuum is to be used as top layer. The result is equivalent to the analytical solution of a multilayer model.

2.2.2 Inhomogeneous layers: effective medium approximation

The value of the dielectric function for layers (or media) where two or more materials are mixed can be derived again by solving the microscopic electric field and the microscopic displacement field per unit volume. The effective medium approximation

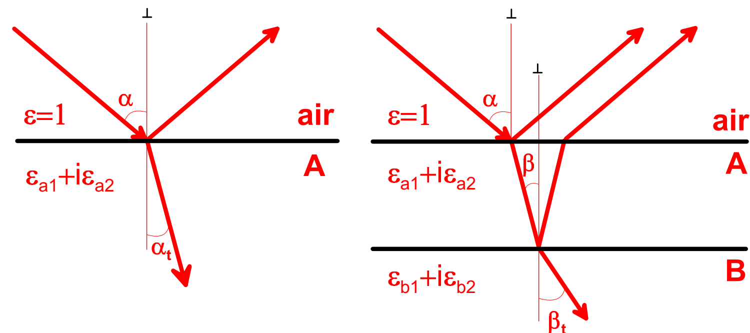

Figure 2.3: *Schematic representation of a 2-layer model (left) and of a 3-layer model (right). The interfaces are assumed to be perfect (abrupt). Thus, in the 3-layer model the light reflected by interface A/B is coherent with the light reflected by interface air/A and they can give rise to Fabry-Perot interferences.*

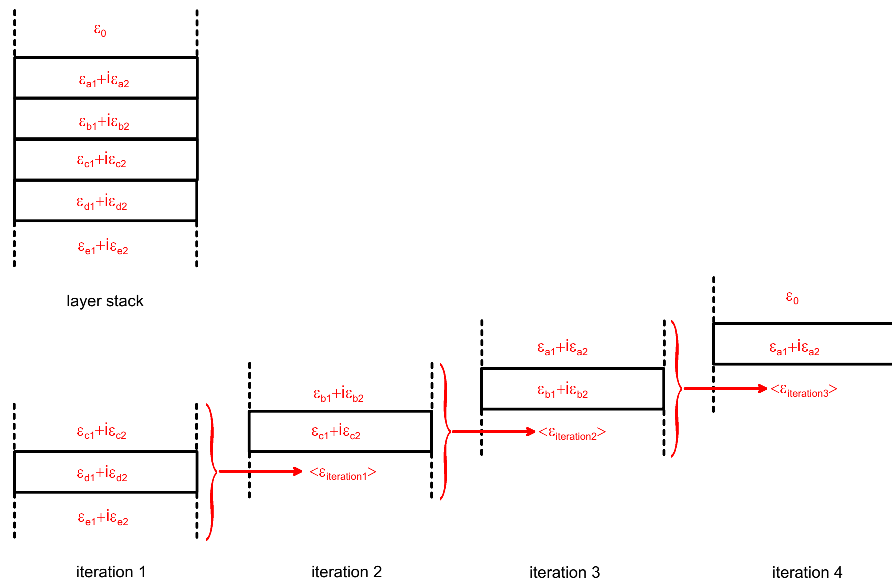

Figure 2.4: *Iterative approach for the calculation of the optical properties of a multilayered sample.*

(EMA) is the averaging over the total volume in order to obtain the dielectric properties of the *effective* medium. The condition for using these theories is that the size of the regions of single material are large enough (on the microscopic scale) to possess their own dielectric properties but are still smaller than the wavelength of the light.

It can be easily shown that the screening charge in the boundaries between the regions plays a fundamental role in the constitution of the dielectric properties of the effective medium, which in turn is not just simply depending on the microstructure [7]. Any inhomogeneous medium can then only be accurately described by the specific distribution of inhomogeneous regions. A more practical, *standard* representation for an inhomogeneous layer constituted by two materials "a"and "b"is given by the following [7, 13]:

$$\frac{\varepsilon - \varepsilon_h}{\varepsilon + 2\varepsilon_h} = f_a \frac{\varepsilon_a - \varepsilon_h}{\varepsilon_a + 2\varepsilon_h} + f_b \frac{\varepsilon_b - \varepsilon_h}{\varepsilon_b + 2\varepsilon_h}. \tag{2.17}$$

ε_h is a "host"dielectric function which can take the values of ε_a or ε_b if the layer consists of "b" inclusions in "a" or viceversa: this leads to the Maxwell-Garnet approximation. Alternatively, ε_h assumes the value of ε in the case of a Bruggemann approximation (the term on the left becomes zero).

The Maxwell-Garnett model assumes spherical inclusions of material "b" in the host "a" (or viceversa) and can be further refined for example by assuming elliptical geometry of the inclusions. The Bruggemann model is simpler (treats the two materials equally, without specifying the host) but it is well suited for example for the approximation of rough surfaces. In this case, material "a" is simply vacuum while material "b" is the bulk material.

2.3 Ellipsometric measurements on unknown materials

The dielectric properties of a material are expressed in terms of a *dielectric function* ε, but ellipsometry can measure only an *effective dielectric function* $\langle\epsilon\rangle$. It means that the ellipsometric measurement of a sample is not a mere measurement of the dielectric properties of a material, even if the sample is nominally made of a single material. For in-situ measurements, where the sample is grown in high purity gas environment, we can assume a negligible contamination. The dielectric properties of the surface will still be different from the bulk dielectric properties because of: (i) surface termination and reconstruction, (ii) surface morphology. In case of heteroepitaxial samples (the focus of this work, since the InN samples have been grown on sapphire or on GaN/sapphire templates) the measurement can be influenced by (iii) the dielectric properties of different layered materials in the sample, (iv) the thickness of each of the different layers present in the layer stack and by (v) the conformation (roughness) of each interface. This list of characteristics of the investigated sample can be defined as the *geometric properties*, or simply *geometry* of the sample.

Knowledge about the growth process and other characterization techniques can provide information on sample geometry (i.e. known growth rate can indicate the

thickness of the layers, AFM measurements can give an indication on surface roughness, etc.). This allows to set a starting model of the layer stack as close as possible to reality. Eventually, unknown parameters of the sample *geometry* can be determined. A requirement for the model calculation of the *effective dielectric function* $\langle\varepsilon\rangle$ is the knowledge of the *material dielectric function* ε, i.e. of the dielectric properties of each material present in the layer stack.

It is important to stress again that the dielectric function is a *material* property. As mentioned previously, ellipsometry measures directly the *effective* (or pseudo-) dielectric function. Practically, this will never coincide with the material dielectric function ε even if measured on a sample constituted by (at least namely) a single material because the surface will always have dielectric properties different from the bulk.

Since the dielectric properties of a material depend also on the concentration of intrinsic defects, a dielectric function cannot be univocally defined for a material if this is not a perfect single crystal. The material grown and investigated in this work is InN, which is not yet available in excellent crystal quality. Furthermore, InN fundamental properties, its bandgap and therefore its dielectric function are still uncertain.

In conclusion, at the beginning of this work the dielectric properties of the material InN could not be easily extrapolated by the effective dielectric function measured by ellipsometry. This because of the (a) not well defined *geometry* of the sample and (b) not well defined quality of the InN layers. On the other hand, the rich information presented by the effective dielectric function could be used from the start to study InN *while* growing, giving an unbeaten insight into the dynamics of the growth process and leading to its optimization. Only at the end of this work, after a critical improvement of the quality and a large set of measurements we were able to evaluate ϵ_{InN}, which is therefore presented in the last chapter.

2.4 MOVPE and ellipsometry set-up

Metal-organic vapor phase epitaxy (MOVPE) is a low-pressure up to atmospheric-pressure growth technique which makes use of organic-metallic precursors and is successful for the growth of high quality semiconductor crystals. It is the technique of choice for several industrial applications and, despite of the difficulties in epitaxy of nitride crystals, is also the method used for the production of GaN based electronic devices [4].

The general principle of MOVPE is shown in Fig. 2.5 while the sketch of the reactor is shown in Fig. 2.6. The MOVPE reactor used in this work is a standard horizontal reactor produced in year 1983 by EPIQUIP. With MOVPE (also often called MOCVD, metal-organic chemical vapor deposition) it is possible to grow high quality single crystals since 1968 [14]. Commercial systems for the growth of nitride based LED's and Laser diodes are still based on the same principle, but they have evolved significantly. They are based on vertical or horizontal gas flow with planetary susceptors (i.e. the samples are rotated along axes parallel to the gas flow). For more information on commercial systems the reader is invited to check the following internet sites [15–17], while for a deeper reading on MOVPE to the following books

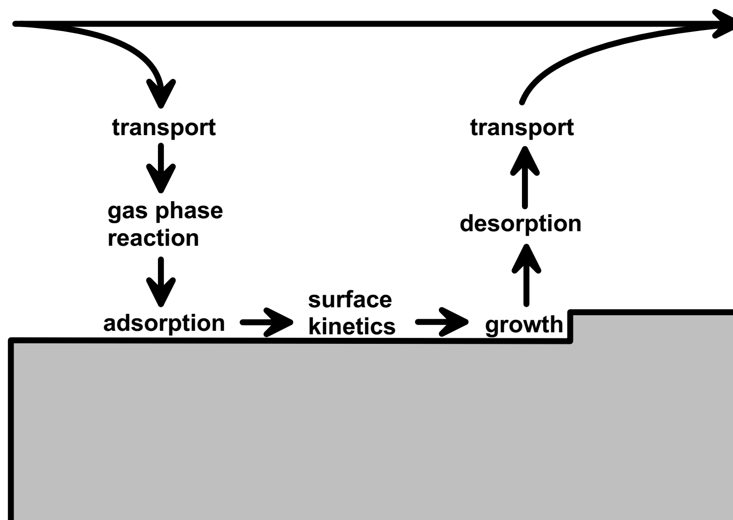

Figure 2.5: *Principle of MOVPE. Sources in the gas phase enter the reactor heated to high temperature (typically from 500°C up to 1200°C for nitride materials). Typical sources are metal-organic precursors for group-III elements, like tri-methyl-Indium and hydride precursors for the group-V elements, like ammonia. During the heating of the sources while they approach the reactor, several gas phase reactions may already occur, for example formation of radicals. Transport of material through the gas phase leads to contact of the molecules/radicals with the surface of the substrate. Adsorption may occur, which might lead to catalytic decomposition of the gas source and to growth. Ideally, carbon present in the metal-organic precursors desorbs and leaves the reactor.*

[9, 18].

The in-situ ellipsometer was developed by equipping the horizontal MOVPE reactor with three low strain windows for optical investigations. It is a scanning-type ellipsometer consisting of rotating polarizer, sample, analyzer (RPSA). It covers the spectral range of 1.6-6.5 eV (775-190 nm), using a 75 W xenon arc lamp. MgF_2 Rochon prisms are used as polarizers since they are sufficiently transparent up to 9 eV, making in principle possible, with an adequate light source, the extension of the measurement range up to 9 eV in a nitrogen purged atmosphere. A double monochromator efficiently reduces stray light effects. While scanning the spectrum, neutral density filters and color filters are used to keep the intensity below the overload limits of the detector (UV-enhanced Si diode) and to suppress higher orders of the monochromator gratings, respectively.

This set-up is very accurate for measurements on InN and GaN because of the choice of the angle of incidence (~65°), which is close to the *pseudo*-Brewster angle for these materials. Consequently, the complex reflectance ratio is maximized and the signal-to-noise ratio minimized.

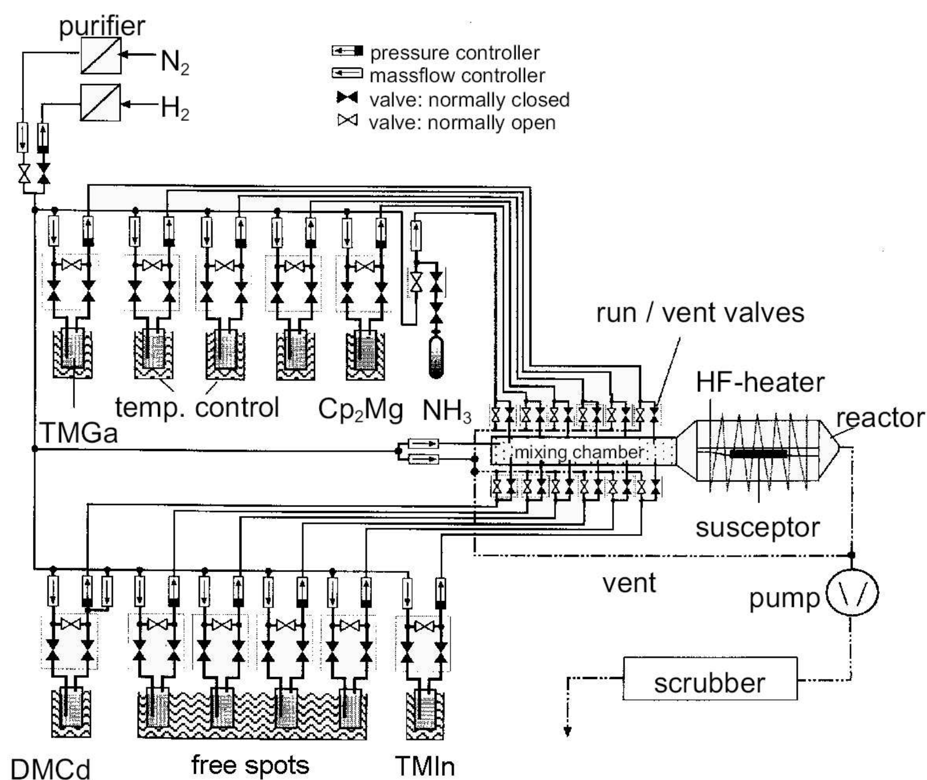

Figure 2.6: *Sketch of the Epiquip MOVPE reactor used in this work for epitaxial growth of InN. Some of the parameters to control are: the flow of the carrier gas (typically nitrogen or hydrogen) through the bottles containing the metal-organic precursors (commonly named* bublers*), the pressure in the bubblers to control the saturation, the temperature of the bubblers, the pressure in the reactor, the total flow of the carrier gas, the flow of the hydride gas precursor, the total pressure in the reactor. Precursors are driven by two valves: the first valve allows the precursors to get into the mixing chamber, the second valve chooses between the vent (which leads directly to the pump bypassing the reactor) and the reactor. A copper coil run by high power radio-frequency current is heating a graphite susceptor up to 1075°C. The sample lies on the graphite susceptor where it is investigated during growth by in-situ SE (see Fig. 2.7). After the reactor and the pump a scrubber is necessary to eliminate the residual reactive, toxic and poisonous species which are residuals of the growth reaction or the portion of the sources that did not react.*

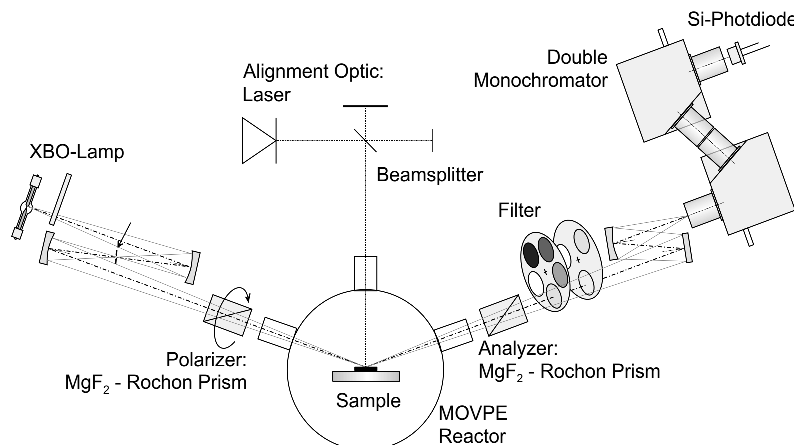

Figure 2.7: *Schematic of the spectroscopic ellipsometer implemented in the MOVPE horizontal reactor. A cross section of the reactor shows the 3 low-strain windows: two for the ellipsometer, the third for the alignment laser.*

To monitor the changes in the angle of incidence and in the zero value of the analyzer due to changes in pressure and in temperature, an alignment laser is used at the window perpendicular to the sample.

2.5 Ellipsometry used in-situ

There are countless reports on in-situ studies of surface adsorption from the early times of ellipsometry, but in-situ growth studies have become possible only with the advent of fast computing electronics. The first studies of growth monitoring were on the growth of AlGaAs heterostructures on GaAs in 1978 [19, 20]. Closed-loop growth control was reported shortly after for the growth of parabolic quantum wells [21]. Nitride materials have also been studied. For example Ψ-Δ trajectories were measured during heteroepitaxial growth of AlGaN quantum wells [22]. The effects of a nitrogen plasma on the surface of sapphire [23] and of SiC were also studied [24].

Ellipsometry can reveal *during growth* the thickness of layered structures, the dielectric properties of the materials in the stack, the composition of alloys and finally the properties of the surface. The following two subsections deal with important points for in-situ ellipsometry: the sensitivity of ellipsometry to morphology and chemistry of the surface and the material dielectric function at high temperature.

2.5.1 Surface sensitivity

The most important information on the growing sample during epitaxy is the state of the topmost monoatomic layers. These can be defined as *surface* of the sample (though it is always debated *how many* of the topmost monoatomic layers are the surface). The surface is in fact changing during growth and morphology, chemistry

and different reconstructions play an important role in the growth process. They can for example strongly influence the quality of the growing layer. During MBE, in a UHV environment, it is possible to use electron-based investigation techniques which are *surface specific*, in the sense that the signal they measure can only originate from characteristics of the surface. In MOVPE, where standard pressures are in the range of millibars, the mean free path of electrons is too short for any application. At these pressures one can still use optical techniques, like SE.

SE is in general not surface specific, and the sensitivity of ellipsometric spectra on the surface is strongly affected by the *penetration depth* of the light. The penetration depth is a measure of how deep an electromagnetic wave can penetrate into a material. It is a characteristic of the material and of the wavelength and is quantitatively defined as the inverse of the absorption coefficient, where the latter is defined by the Lamber-Beer law. In the regions of high absorption of the growing material the penetration depth of the light can be as small as some nanometers. For example, at the higher interband transitions of some crystalline semiconductors one finds $\sim$4 nm for Si, $\sim$5 nm for GaAs, $\sim$6 nm for InP [7]. In this energy range, submonolayer surface modifications have a strong influence on the measured ellipsometric angles, making ellipsometry extremely sensitive to the surface monolayer. This high sensitivity is not reached in standard reflectance measurements.

Indium Nitride and in general the nitride semiconductors in their most stable modification all crystallize in the hexagonal structure. Thus, normal incidence optical techniques that require an isotropic bulk (reflectance anisotropy spectroscopy, for example) cannot be used. Thus, ellipsometry has become the optical technique of choice for their in-situ growth investigation.

The dielectric function is sensitive to the topmost surface layers when the penetration depth of light is low, i.e. at the higher electronic interband transitions, as mentioned previously. It was found experimentally that the amplitude of $\langle\varepsilon_2\rangle$ at these energies is inversely proportional to the roughness or to the thickness of an oxide overlayer. By using the words of D. Aspnes: *the bigger, the better* [7]. Thus, the amplitude of $\langle\varepsilon_2\rangle$ at energies close to the higher interband transitions is a monitor for the quality of the surface: any increase in amplitude is toward a smoother surface while any decrease is towards a rougher surface. This interpretation might not always be true in the case of epitaxy of InN, as will be shown in the last chapter of this work, which deals with a model for the dielectric function of InN.

Ellipsometry has shown to be very sensitive to thin overlayers and to be able to recognize different surface reconstructions in the case of, for example, GaN [25]. In this work Ga-polar GaN surfaces were investigated in MOVPE and in UHV conditions. In the latter, Low Energy Electron Diffraction (LEED) was used to identify two GaN surface reconstruction, the Ga-rich 1×1 and the nitrogen rich $\sqrt{3}\times2\sqrt{3}$R30°. $\langle\varepsilon\rangle$ measured in UHV was then compared with $\langle\varepsilon_2\rangle$ measured in MOVPE and the two surface reconstructions were identified in the gas ambient of MOVPE, where LEED or other typical methods of surface science cannot be applied.

The measurement of the parameter set $\tan\Psi$, $\cos\Delta$ provides a surface sensitive tool, since $\tan\Psi$ is mostly sensitive to changes in surface chemistry while $\cos\Delta$ is mostly sensitive to surface roughness and generally to the thickness of a very thin overlayer. In the case of $\cos\Delta$ a thin overlayer will induce a phase shift between

the two components of the electromagnetic wave, as well as if the overlayer is just a rough surface. In the case of tanΨ the changes of surface chemistry will change the dipoles on the surface. This in turn influences both the magnitudes of r_p and of r_s. tanΨ is then responding to this change because of its definition (see equation 2.2). In turn, the phase shift will only be weakly affected by the change of chemistry in the surface. The bulk contribution originating from the component of the dielectric tensor perpendicular to the surface can usually be neglected (see [9], pages 238, 239).

2.5.2 High temperature dielectric function

Layers in MOVPE are grown at high temperature, ranging from a minimum of 300°C up to 1100°C. The dielectric function of a semiconductor changes with temperature. Electronic transitions at critical points of the band structure experience a damping with increasing temperature and in most cases a red shift [26] with the exception of some Lead-VI compounds which show an unusual blue shift [27]. According to Varshni [28] the energy shift of the critical points follows a semi-empirical law:

$$E_{cp}(T) = E_0 - \frac{\alpha T^2}{T+\beta}. \tag{2.18}$$

The parameter E_0 of equation 2.18 is the transition energy at T=0 K, α and β are empirical constants and T is the absolute temperature in Kelvin. The constant α is related to the electron-phonon interaction and β is closely related to the Debye temperature. Other empirical formulations have been given, for example, by Allen and Cardona [29] but *ab-initio* theory approaches to explain the changes in the dielectric function at high temperature have not been developed yet.

At sufficiently high temperature one can normally neglect the parameter β, so that equation 2.18 becomes:

$$E_{cp}(T) = E_0' - \alpha T. \tag{2.19}$$

The parameter E_0 of equation 2.18 cannot be evaluated (therefore it appears with a prime in equation 2.19).

Experimental results on the dependence of the dielectric function on temperature for several semiconductors is reported in [30]. For InN there are only reports on the bandgap at low temperature [31] (bandgap at room temperature was ∼0.7 eV). Chapter 8 deals also with studies of the critical points between room temperature and 500°C for InN.

2.6 Ellipsometry on InN/sapphire samples

It is relevant now to discuss briefly the effective optical properties of InN layers grown on sapphire and the criteria of interpretation of the in-situ ellipsometric spectra presented in this work. Prior to this, we shortly discuss the optical properties of sapphire.

Sapphire is the substrate used for epitaxial growth in this work. It is a transparent material in the energy range of the in-situ ellipsometer. The substrate can be still considered semi-infinite since the backside of the wafer is non-polished. In fact, the

light reaching the rough back-side of the sapphire substrate is then scattered and absorbed by the black susceptor where the sample is placed. The signal to noise ratio is rather low for measurements on sapphire, especially if it is compared to measurements on absorbing layers. The high noise level originates on the one hand from the low intensity of the total reflected light. On the other hand, it is difficult to measure a semi-transparent material growing on another transparent material. More precisely, transparent materials have a $\cos\Delta=\pm 1$ (a phase shift of 0° or 180°), which means a very low change in the intensity modulated by the rotating polarizer in the utilized ellipsometry set-up[1].

When growing InN onto the surface of the sapphire substrate, the signal to noise ratio improves strongly. In Fig. 2.8, top, we show a typical effective dielectric function (imaginary part) of a 100 thick InN layer grown on sapphire. The main contributions to $\langle\varepsilon_2\rangle$ at higher energies (above ~4 eV) originate from the InN interband electronic transitions. These are the three peaks appearing above 4 eV. With few exceptions, all the MOVPE InN layers grown at the TU-Berlin show higher interband transitions E_1, E_2 and E_3 at 4.9 eV, 5.3 eV and 6.1 eV at room temperature, in good agreement with

[1] A possible solution would be the implementation of a quarter wave retarder plate, which will shift the phase by 90° allowing a much more accurate measurement. The retarder is anyway wavelength-dependent. Furthermore, the addition of a new optical component is complicated in a compact in-situ set-up, where space-compromises are pushed to the limits. Anyway, the present ellipsometry configuration has supplied valuable measurements on sapphire samples as well.

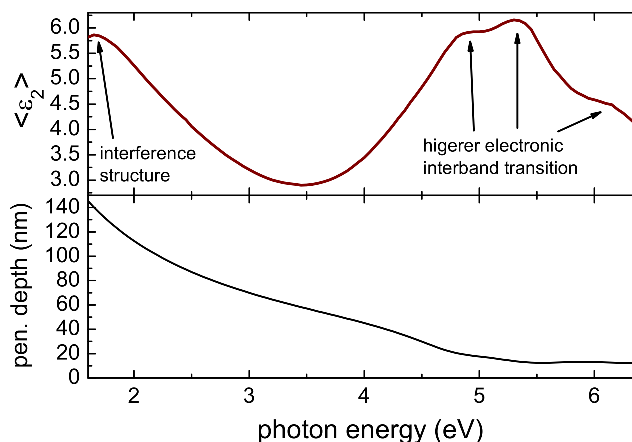

Figure 2.8: *In the spectrum on the top, example of a typical ellipsometric measurement of the effective dielectric function (imaginary part) of a ~100 nm thick InN layer. Below ~4,eV interference structures are dominant. Above ~4 eV the electronic interband transition of InN are only influenced by characteristics of InN bulk and surface. This holds, since the penetration depth of the light (spectrum at the bottom) in InN is high below 4 eV and low above 4 eV (lower than 20 nm).*

other ex-situ results [32, 33] and with ab-initio calculations [34]. Their amplitudes serve as a monitor for the crystalline and surface quality of the epitaxial layer (as discussed in section 2.5). This holds for the layers discussed in this work (all thicker than ∼100 nm), since the penetration depth of the light at the interband transition energy is below ∼20 nm, as shown in Fig. 2.8, bottom.

The penetration depth of light for InN shown in Fig. 2.8, bottom[2] at energies below the interband transitions is high enough to allow interferences for InN layers for thicknesses below ∼400 nm. Thus, between 1.6 eV and around 4 eV these InN layers will show interferences in optical spectra. From the period of the interferences we can calculate the layer thickness (i.e. the growth rate), while the amplitude of the interferences depends on the homogeneity of the InN layers. In Fig. 2.8, below 4 eV there is a large interference structure with a peak in the infrared. It indicates an InN layer thickness of ∼100 nm.

[2]Penetration depth was at first, with rough approximation, guessed by the effective dielectric function. This shown in Fig. 2.8 is an anticipation of the results of Chapter 8.

3. Indium Nitride: state of the art

Using the words of Prof. Bechstedt, University of Jena: "... it is extraordinary that, at the beginning of the third millenium, the bandgap of InN is still un-known!". He pronounced this sentence at the international workshop of nitrides held in Aachen in 2002. In the same session, Prof. Davydov from the Joffe Institute in St. Petersburg showed his results on the optical characterization (photoluminescence, transmission and reflection measurements) of recently grown, high quality InN epitaxial layers. These results were pointing to a very narrow bandgap, of a value around 0.8 eV. Professor Bechstedt himself presented *ab-initio* calculation of the band-structure in excellent agreement with Davydov experiments. The former accepted value ranged from 1.9 to 2.2 eV, more than a factor of two larger than the new proposed one. The interest toward InN increased dramatically, led by the curiosity of basic research scientists but also because of promising predictions of the properties of this material: solar cells, high frequency, high power devices and optoelectronic devices based on InN are predicted to have top performances.

This chapter deals with the material InN. It will review the basic properties of this material, with a critical eye on the *bandgap story* since the discussion on InN has evolved very rapidly in the last 4 years and it is safe to adopt a careful approach. The second section presents a review of literature results on growth of InN. Finally, one of the first growth procedure used in this work for MOVPE InN is given. It can be cosidered the starting point for this work.

3.1 Properties

InN is the group III / group V (III/V) binary compound semiconductor with the largest anion/cation size ratio (not considering Thallium compounds, which are not largely studied)[1]. As a consequence of this large difference in size, the polarizabilities of the two atoms are also very different. Polarizability is the relative tendency of the electron cloud of an atom to be distorted from its normal shape by the presence of a nearby ion or dipole, or, in general, by an external electric field. In other terms, it is the *softness* of the valence electron orbitals. Large atoms tend to have high polarizability, small atoms low polarizability. As a rule of thumb, atoms prefer to bind other atoms with similar polarizability. In this view, Indium and Nitrogen will have a low affinity because of the large size ratio.

Nitrogen has a Pauling electronegativity of: 3.04, while Indium has a Pauling electronegativity of: 1.78 [37]. For a completely covalent bond the difference in electronegativity δEN is 0, which is the case of homo-atomic bindings. The indicative

[1] Atomic Indium diameter: 0.4 nm; atomic Nitrogen diameter: 0.15 nm ([35] and references therein). Elsewhere, atomic Indium diameter: 0.324 nm, atomic Nitrogen diameter: 0.148 nm [36]

	E_b(eV)	ΔH(eV)
AlN	-11.669	-3.13
GaN	-9.058	-1.08
InN	-7.970	-0.21

Table 3.1: *Binding energies [38] and formation Enthalpies [39] for III/nitrides wurtzite.*

threshold between covalent and ionic binding is δEN=1.7, larger values of δEN indicate ionic bonds. The difference δEN=1.26 refer to the first ionization, and indicates that the binding between Nitrogen and Indium is relatively covalent. The ionic component in the bond is anyway among the strongest when compared with other compound semiconductors, therefore, the co-existence in the same lattice of such large cations and such small anions will lead to repulsion between the cations.

The former considerations hint already that the formation of an InN crystal should not be extremely favorable. Table 3.1 shows calculated values for nitride semiconductors, E_b is the binding energy taken from [38] and ΔH is the Enthalpy of formation taken from [39]. The binding energy of InN is the lowest among the nitride compounds and its formation energy is extremely small. Thus, it can be predicted that InN is extremely difficult to grow.

3.1.1 Structural properties

InN is wurtzitic in its most stable thermodynamic phase, its space group is $P6_3mc$. This phase is also called α-InN. Wurtzite is formed by two interpenetrating hexagonal close packed lattices (hcp), where each lattice is formed by one of the two elements. The close packed layers can stack over the starting position A by filling two different positions named B and C. The hcp structure has an ABABAB sequence of alternating close packed layers (where face centered cubic, also close packed has a sequence of ABCABCA). The coordination number is 12 with 6 nearest atoms in the plane of a layer, 3 nearest atoms in the layer above and 3 nearest atoms in the layer below. The geometry of the binding between the two elements is tetrahedric, which means that each atom has 4 nearest neighbors of the other atom-type. Wurtzite structure is compared to zincblende in Fig. 3.1, where it is shown that it has a lower symmetry with respect to zincblende (based on face centered cubic). The independent lattice parameters for wurtzite are two, named a and c. The lattice parameter c lies parallel to the direction of the stacking of the closed packed planes and parallel to the crystallographic direction identified by the Miller's indexes (0001). This is then equivalent to the (111) direction in cubic symmetry. The lattice parameter a lies perpendicular to the (0001) direction and is defined along 6 equivalent directions at 60° angle one from each other, one of them being $(1\bar{2}10)$. The notation for hexagonal structures is clearly redundant (only two of the first three indexes, defined on the [0001] plane are independent) but it has nevertheless become of common use. Often the redundant third Miller index is omitted and direction $(10\bar{1}2)$ is indicated as (10.2).

An sp^3 hybridization of both Indium and Nitrogen atoms leads to a tetrahedral bonding. One of the tetrahedric bonds is parallel with the c-axis, and the lattice pa-

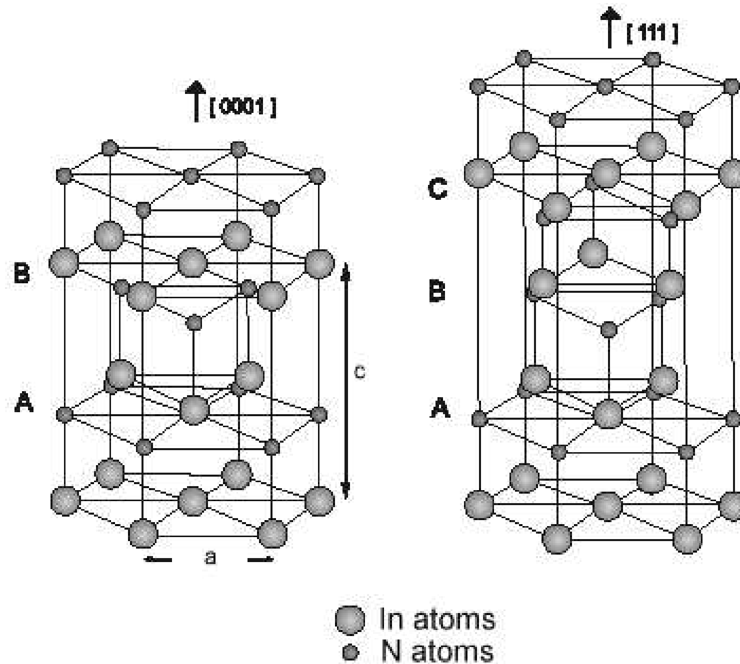

Figure 3.1: *Crystal structure of wurtzite (left) and of zincblende (right) shown along the equivalent (0001) and (111) crystallographic directions. The closed packed planes are in evidence for both structures to show the stacking of the planes A, B and C. Plane C does not exist in the wurtzite structure. The principal crystal directions for wurtzite,* a *and* c*, are also shown. The figure is taken from reference [40].*

rameter u is defined as: u=$(c/a)^2$=0.375. The atomic distance between Nitrogen and Indium and therefore the parameter u is in principle defined by the crystal symmetry. For wurtzite one obtains u=3/8=0.375. In practice, internal fields originating from the crystal polarity and from the anisotropy may deform the tetrahedron, resulting in a different lattice parameter u. This is the case for InN, with u=0.379 [41].

Face centered cubic (fcc) is the second most stable modification [42]. Phase transition hcp to rocksalt occurs at a pressure of 12.1 GPa with a volume reduction of 17.6 percent [43].

Huza and Han [44] did grow the first InN powders and measured X-ray diffraction (XRD), identifying the wurtzitic structure and measuring the lattice constants. More recent measurements of the lattice constants on single crystalline wurtzitic InN layers gave: a=0.35365 nm; c=0.57039 nm [2]. These values differ from the values published previously (see, for example [1, 44, 45]) which were, on the other hand, measured on powder or polycrystalline InN.

Reports on cubic InN are very few and the material is rich in stacking faults defects and inclusions of hexagonal volumes. Surprisingly, cubic InN was found to grow on

r-plane (01$\bar{1}$2) sapphire [46] with lattice constant a=0.4986 nm.

3.1.2 Optical properties and fundamental bandgap

Most often cited values of the fundamental bandgap of InN were first reported in 1986 [1]. Absorption measurements on materials grown by magnetron sputtering did show an absorption edge lying at around 1.89 eV for layers with excellent electronic properties. Anyway, the authors were not able to reproduce the result and did not observe near band-edge photoluminescence in this sample. A photoluminescence peak was observed only 18 years later, after demonstration of the first epitaxial, single crystalline films grown by plasma-assisted molecular beam epitaxy (PA-MBE). Anyway, the luminescence peak was measured at much lower energy and it was corresponding to a much lower absorption edge for these InN layers with improved quality [2]. As shown in figure Fig. 3.2 both absorption and photoluminescence spectra agreed with a fundamental bandgap lying below 0.9 eV and soon these results were confirmed by other laboratories [47, 48]. Similar measurements on Indium rich $In_xGa_{1-x}N$ alloys were in agreement with the narrow bandgap. The new bowing parameters of the fundamental bandgap for this alloy [49, 50] were also much smaller and more realistic than the bowing parameter which were assumed with the large (~2 eV) InN bandgap. The reasons for larger bandgaps measured earlier were also discussed. According to [50], the large formation of oxide on the surface of sputtered InN samples led to a mixture of InN and In_2O_3. The latter has the fundamental bandgap at ~3.5 eV and absorption measurements on this mixture would lead to values which are intermediate, explaining the scattering of the values reported on not epitaxial (sputtered) material before 2002.

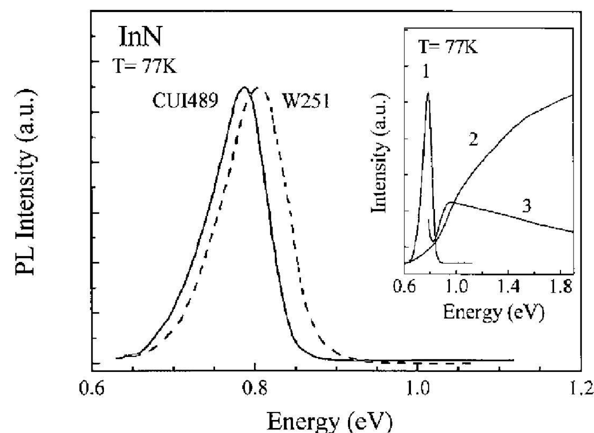

Figure 3.2: *Photoluminescence spectra on two different InN epitaxial layers (CU1489 and W521). In the inset, photoluminescence (1) from one of the two layers (CU1489) is shown again in comparison with absorption spectra (2) and with photoluminescence excitation (3). The figure is taken from Davydov et al. [2], where for the first time a narrow bandgap was proposed for InN.*

Soft X-ray absorption and emission experiments can indicate the energy position of the valence band and of the conduction band with respect to the vacuum level. InN layers were investigated by this technique and the energy difference was used to indicate the fundamental energy gap at ∼0.7±0.1 eV [3]. Though the error appears to be somewhat larger and the authors fail to give an indication for the Fermi level, this result clearly hints at a narrow bandgap for InN.

It is well accepted that for compound anion-cation semiconductors the fundamental bandgap increases as the anion (or cation) atomic number decreases. This is sometime called the bandgap-common-cation-rule, or -anion-rule. If the narrow bandgap is accepted, for III/V semiconductors InN is the only exception. In this case, in fact, InN bandgap of ∼0.7 eV would be much smaller than InP bandgap, lying at 1.46 eV. The exception is not unique among semiconductor compounds since it occurs also for ZnO and ZnSe (E_0=3.4 eV for ZnO and E_0=3.8 eV for ZnSe, respectively). By using an LDA-based semiempirical method, authors of reference [51] have shown that in both cases, for InN and for ZnO, the larger difference in electronegativity (i.e. the higher ionic component of the bond) with respect to other semiconductor compounds leads to reduction of the expected value for the fundamental bandgap.

Ab-initio Density Functional Theory (DFT) was for a long time unable to calculate correctly the bandstructure of InN. In the Local Density Approximation (LDA) a typical problem was a *negative bandgap*, which was obtained in different works (see for example [38]). According to [42] the main reason lies in the role of the repulsion between the Indium 4d electrons and the Nitrogen 1p electrons, which arises when the Indium 4d electrons are considered as valence electrons. By *freezing* the Indium 4d electrons into the core the calculated bandgap value reads 0.8 eV. A similar approach was used to explain the narrow bandgap of ZnO as well [52]. The band structure calculated for InN by *ab-initio* from reference [42] is shown in Fig. 3.3 and the corresponding dielectric function calculated in the independent-particle approximation is shown in Fig. 3.4. A measurement of the effective dielectric function by spectroscopic ellipsometry (from reference [33]) is shown in Fig. 3.5.

Despite wide agreement for a bandgap narrower than 1 eV, there are publications which report again larger values also for epitaxial InN layers. In reference [53], after spacially-resolved cathodoluminescence, the luminescence peak at 0.8 eV was correlated with InN regions rich in metallic Indium. Absorption spectra measured at 0.35 K were interpreted via classical Mie scattering theory to account for Indium clusters and the result indicated an absorption edge of 1.4 eV. According to [54, 55] after transmission and absorption measurements the bandgap was at ∼1.2 eV. In the same letters the authors suggested that the photoluminescence peak measured on other InN layers might rather originate from recombination where an energy level originating from defects is involved, similar to what is generally called *yellow photoluminescence* from GaN layers with low crystal quality. Further work supports their findings [56]. Measurements performed with valence electron energy loss spectroscopy (VEELS) from other authors indicate an even larger bandgap, lying at ∼1.7 eV [57].

The anisotropy of the dielectric function of InN was measured by spectroscopic ellipsometry over a large energy range from 0.7 eV up to 10 eV in reference [33] and from 3 eV up to 30 eV in reference [58] on InN layers grown on a-plane sapphire.

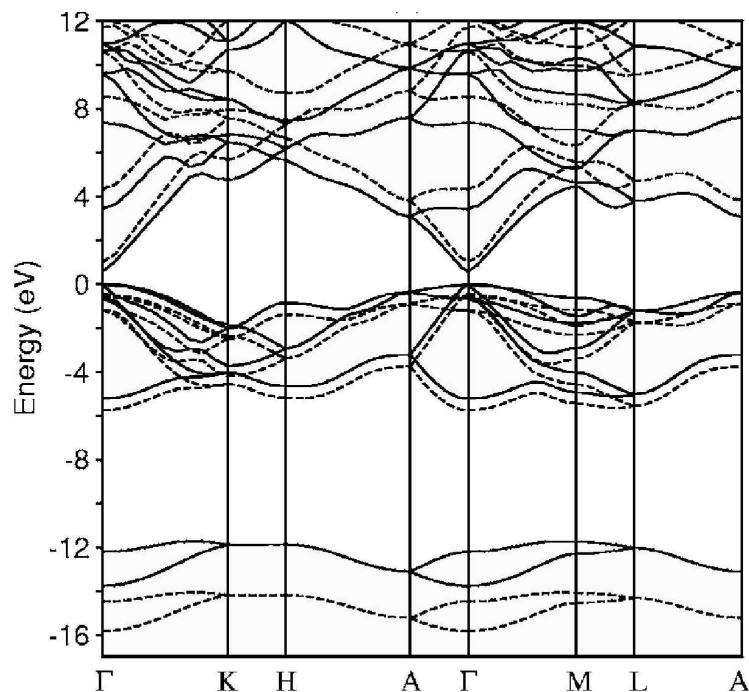

Figure 3.3: *Wurtzite InN bandstructure calculated via Kohn-Sham equation (solid lines) and via quasiparticle approximation (dashed lines). The figure is taken from reference [42].*

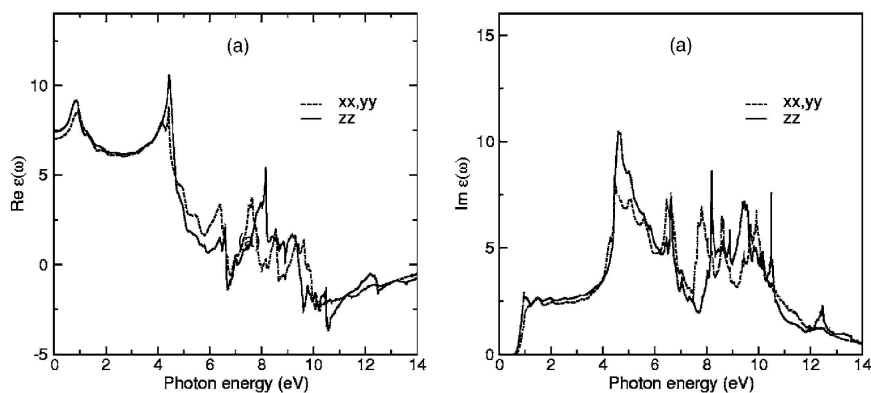

Figure 3.4: *Calculated dielectric function of wurtzite InN. Both the ordinary (dashed lines) and the extraordinary (full lines) component of the dielectric tensor are shown in real (left) and imaginary part (right). The figure is taken from reference [42].*

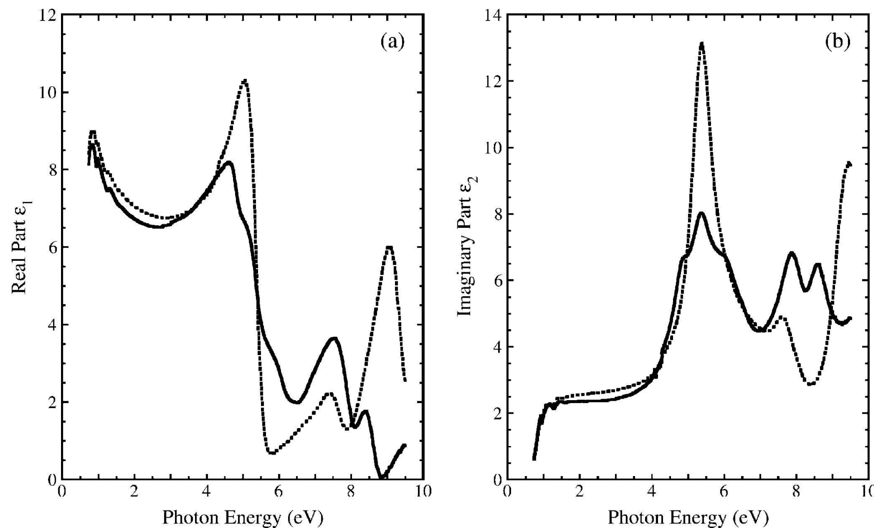

Figure 3.5: *Measured dielectric function of wurtzite InN, from samples grown on sapphire a-plane. The ordinary (full lines) and the extraordinary (dashed lines) component of the dielectric tensor as well as the real (left) and imaginary (right) parts are shown. The figure is taken from reference [33].*

3.1.3 Electronic properties

InN has been predicted to have remarkable electronic properties. In particular, its peak drift velocity and breakthrough fields are the highest among all the semiconductors [6], while mobility of the electron carriers is the highest among the nitride compounds. Their result is shown in Fig. 3.6, where drift velocity of nitride semiconductors is plotted versus electric field. These calculation were performed with an InN bandgap value of circa 2 eV, but the general trend of Fig. 3.6 was confirmed by more recent experimental results and new Monte Carlo calculations on InN based on the narrower bandgap of 0.7 eV [59], where transient Raman spectroscopy and Monte Carlo calculations using the narrower bandgap value for InN agree for electron velocities with a cutoff at around 2×10^{8}cm/s. Considering also its high mobility of 4000 cm^2/Vs [60] (the highest among the III/nitride semiconductors, see table 3.2), InN is the best candidate for the fabrication of ultrafast electronic devices.

Material	Electron mobility (cm2/Vs)
AlN	300 [61]
GaN	1000 [61]
InN	4000 [60]; 4400 [61]

Table 3.2: *Electron mobilities calculated for III/nitride wurtzite at room temperature.*

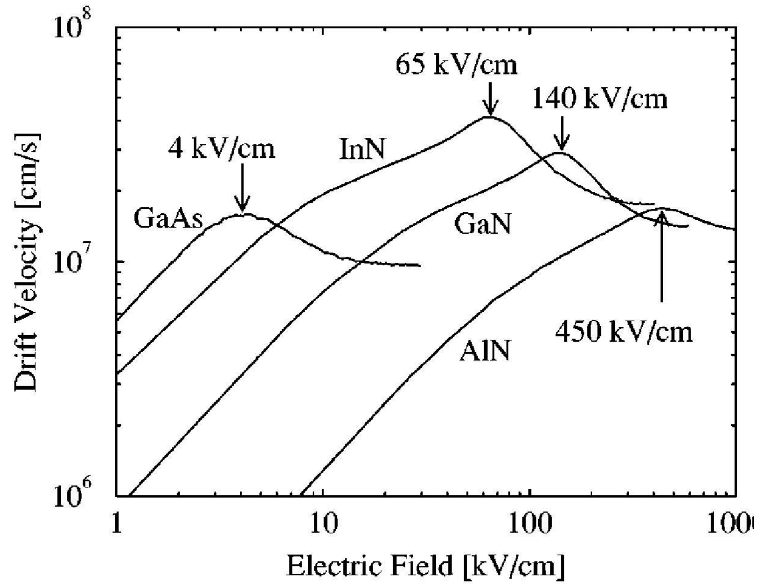

Figure 3.6: *Monte Carlo calculations of the electrical properties of nitride semiconductors in comparison with GaAs. InN displays the highest peak drift velocity. Taken from reference [6].*

Although the theoretical predictions are very promising, epitaxial InN layers are up to now always n-type with a very high background electron concentration. The growth of p-type material, which is necessary for any relevant device application is not feasible as long as the background n-doping is not reduced below 10^{17} electrons/cm^3. There is still much discussion on the origin of the background donor concentration in InN. Oxygen atoms at the nitrogen positions are a possible candidate, since they would act as donors and they are possibly present as impurities during the growth process. The common belief that nitrogen vacancies are the main origin of the high number of donors (similarly to GaN [4]) was challenged by recent experiments finding instead predominantly Indium vacancies [63]. These were detected by low-energy positron annihilation and were dominant with respect to nitrogen vacancies in the investigated MBE grown InN layers. The Indium vacancies were also found to be correlated with carrier concentration and electron mobility.

The main contribution to the residual n-doping in InN epitaxial material, anyway, does not seem to originate from defects, but from a strong accumulation of electrons on the surface. Hall measurements on a series of InN layers with different thickness did show a strong correlation of both mobility and concentration of residual donors with layer thickness [64]. The thicker the layer under investigation, the lower was the number of electrons and the higher was the mobility of the carriers. Valence band XPS indicated that the Fermi level of the surface lies $\sim$1.4 eV above the maximum of the valence band, corresponding to $\sim$0.7 eV into the conduction band at the surface [65]. This indicates already downward band-bending and electron accumulation. Further proofs of the accumulation layer is given in [62] where the authors have measured

High Resolution Electron Energy Loss Spectroscopy (HREELS) on InN layers after cleaning of the surface with atomic hydrogen. *Ab-initio* calculations indicates that since the conduction band minimum in InN is extremely low in energy, the branch point energy E_b (also known as the charge neutrality level and the Fermi stabilization energy, which is the crossover point from donor type to acceptor type surface states) is located at the Γ-point. This calculation predicts correctly the location of the Fermi level at the surface as calculated from the electron plasma at the conduction band probed by HREELS measurements [66], giving experimental evidence and theoretical explanation of the electron accumulation layer at the InN surface, as shown in Fig. 3.7. The measured density of electrons on the surface is higher than for any other III/V semiconductor: $\sim 2.5\times10^{13}\,\mathrm{cm}^{-2}$ and giving rise to an electric field of $4.6\times10^{8}\,\mathrm{Vm}^{-1}$ at the surface and band bending of $\sim 0.74\,\mathrm{eV}$, according to reference [62].

A strong indication that oxygen contamination at the surface is responsible for enhancing the electron concentration at the surface is given in [67]. The authors report on resistance measurements and simultaneous sputtering with Ar^{+} ions under grazing incidence that, shown by Auger measurements, removes oxygen contamination. The InN surface shows a largely increased resistivity after cleaning from oxygen atoms. The resistivity recovers when oxygen is again absorbed.

The effects of this strong electron accumulation layer onto the properties of InN are not fully understood yet. It is possible that the accumulation layer is responsible for the strong resistance to radiation of InN and of Indium rich nitride alloys reported in reference [5]. The effects of the accumulation layer on epitaxy of InN have not been investigated yet and neither will be in this PhD thesis, but it is worthwhile to take

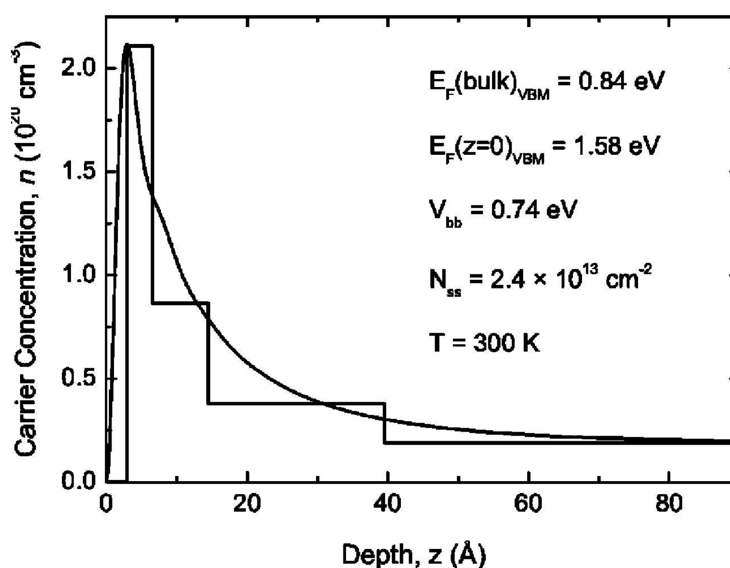

Figure 3.7: *Calculation of the carrier concentration profile close to the surface (straight solid line) compared with the profile obtained from HREELS measurements. Taken from reference [62].*

note of this InN property also for future growth investigations.

3.2 Growth of Indium Nitride

InN is not found in nature. It was synthesized initially as a powder [44, 68]. InN materials investigated in the 1980's and 1990's were mostly polycrystalline films grown by magnetron sputtering [1]. Today it can be hetero-epitaxially grown as thin film on various substrates and templates. Although most results are on sapphire and GaN/sapphire templates (see section 3.2.2) there are also works on GaP [69, 70], GaAs [71, 72], Si [73], SiC in MBE [74] or MOVPE [75]. Table 3.3 summarizes the lattice mismatch of InN to various substrates. The epitaxial techniques successfully used so far are Molecular Beam Epitaxy (MBE) and Metal-Organic Vapour Phase Epitaxy (MOVPE). Free-standing, thick (hundreds of μm) InN single crystals have not been grown yet.

Substrate	Mismatch with InN
Sapphire (0001) [76]	-25.4
Sapphire (0001)* [76]	29.3
GaN (0001) [77]	10
GaAs (0001) [77]	11.5
Silicon (111) [77]	8
GaP (111) [77]	8

Table 3.3: *Lattice mismatch of InN to various substrates. The second value of sapphire (*) refers to the lattice mismatch when the unit cell of InN is 30° rotated in-plane with respect to the sapphire unit cell (see Fig. 3.9).*

3.2.1 Main reference for InN: GaN epitaxy

GaN displays several similarities to InN, among them the growth on extremely mismatched substrates. Therefore, GaN growth is a point of reference for the InN growth experiments.

In spite of the large mismatch (16%), the GaN growth procedure developed on sapphire substrates in the early nineties allowed the production of the first nitride based blue LEDs [4]. Due also to their low price (even with the competition of GaN substrates for homoepitaxy) sapphire substrates are still largely used nowadays [78]. We will present here only the MOVPE process, since this is the growth technique used in this work.

The GaN 4-steps growth procedure on sapphire [4, 79, 80] is summarized in Fig. 3.8. The first step is the nitridation of sapphire. This is performed normally at high temperatures (above 1000°C) and using ammonia as nitridating specie. A possible alternative is simple annealing of the substrate at similarly high temperature in a reducing atmosphere (generally hydrogen). In the case of GaN, both nitridation and annealing leads (after careful optimization of the MOVPE parameters) to successful growth of excellent GaN layers. As will be shown later (Chapter 4) in the

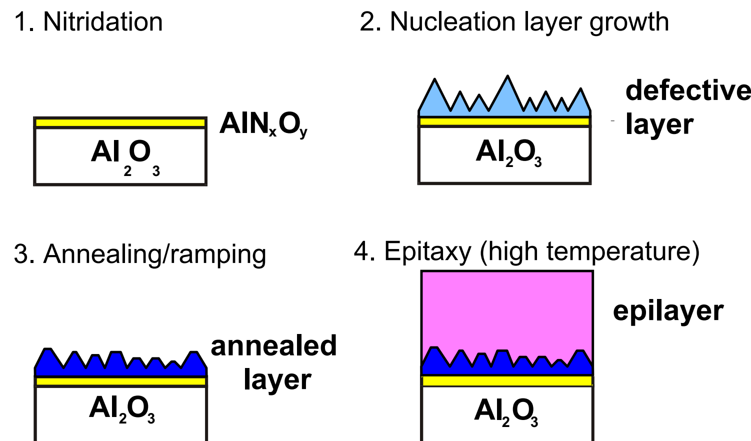

Figure 3.8: *Growth procedure of GaN on sapphire in 4 steps: 1) sapphire nitridation, 2) growth of a defective (low temperature) nucleation layer, 3) recrystallization of the nucleation layer through annealing at high temperature, 4) growth of the epitaxial layer. Taken from [81].*

case of InN, sapphire nitridation is the only preparation leading to single crystalline epitaxial layers.

The second step is the growth of a nucleation layer, at low temperatures (normally 550°C for GaN). Such a layer has the role of *concentrating* defects that will necessarily form in a highly mismatched system. The epitaxial layer will then, in optimal conditions, contain a much smaller amount of defects (generally below $10^{10}\,\mathrm{cm}^{-2}$) and allow fabrication of high performance device structures. The absence of such a defective nucleation layer leads normally to a more homogeneous distribution of dislocations, vacancies and other defects along the whole depth of the epitaxial GaN layer, up to the surface, which is not optimal. In fact, the best crystalline properties should be found at the surface of the GaN template.

The nucleation layer presents poor morphologies and a large amount of cubic and amorphous inclusions. This would in general lead to poor morphologies into the epitaxial layer and to stacking faults. The third step is therefore annealing of the nucleation layer at high temperatures (above 1000°C) under ammonia stabilization (GaN decomposes above 950°C). Annealing leads to a phase transition from cubic to hexagonal and to a smoothing of the surface [82], resulting in state-of-the-art GaN epitaxial layers grown through the fourth step, the epitaxial growth.

The high growth temperature in the last step is necessary for good crystal quality (resulting from high mobility of the atomic species on the surface) and for an adequate activation of the ammonia molecules. The V/III ratio, i.e. the mole ratio between NH_3 (ammonia, the V-precursor supplying nitrogen atoms for the growth) and TMGa (Trimethyl-Gallium the III-precursor supplying Gallium atoms), is typically 2000 [79, 83]. This is considered to be already rather high in comparison with other more studied III-V compounds (for example, GaAs can be grown with V/III ratio down to 5 [84]).

The process developed for epitaxy of GaN presents some concepts that can be very instructive for the development of a successful growth process for InN. On the other hand, the new material presents new challenges and, at the end of this work, it will be shown that these concepts must be applied in a different way to grow high quality InN layers.

3.2.2 Epitaxy of InN on sapphire substrates

Despite a large lattice mismatch of 28% on sapphire [76], most of the results concerning MOVPE of InN published in the last two years were obtained on sapphire as a substrate, either nitridated before InN growth [85, 86] or with a GaN or AlN nucleation/buffer layer ([87–89] in MOVPE, [90, 91] in MBE). The reasons for this choice lies mainly in the well developed GaN technology that uses sapphire as substrate. Also, a step-procedure similar to the one developed for GaN epitaxy on sapphire can be adopted for InN growth. Therefore, in this work InN epitaxy was developed on sapphire substrates .

The symmetry of sapphire is trigonal (space group: $R\bar{3}c$), lower than wurtzitic hexagonal symmetry (space group: $P6_3mc$). As a consequence, there are two possible ways nitride crystals can grow epitaxially on (0001) sapphire surfaces. The first possibility is obvious: the nitride crystals grow with their unit cell oriented in the same way as the sapphire unit cell. The second possibility is outlined in Fig. 3.9: a rotation of the nitride unit cell of 30° on the c-plane, corresponding to the crystallographic relation: $(10\bar{1}0)_{nitride} \parallel (11\bar{2}0)_{sapphire}$. The lattice mismatch in the two possible orientations is different and is listed for growth of nitrides on sapphire in table 3.4.

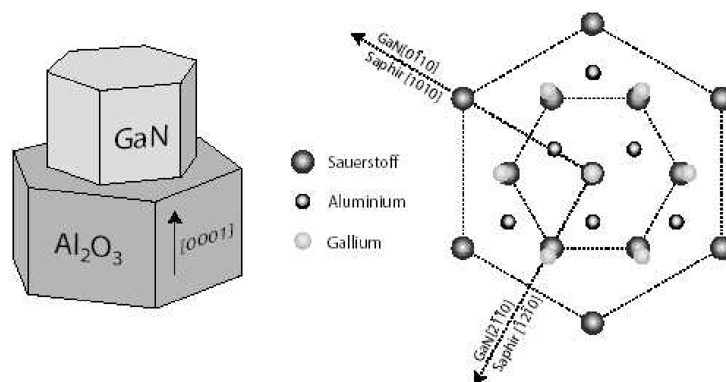

Figure 3.9: *On the left, a 3-dimensional view of the orientation of the wurtitic GaN structure on the sapphire substrate. There is a 30° in-plane rotation. The 2-dimensional projection is shown on the right. Figure taken from [92].*

Because of the smaller mismatch, when AlN or GaN are epitaxially grown on (0001) sapphire surfaces, their unit cell is rotated 30° with respect to the unit cell of sapphire. The same orientation is found in thin AlN layers obtained by nitridation of

	$(10\bar{1}0)_{nitride} \parallel (10\bar{1}0)_{sapphire}$	$(10\bar{1}0)_{nitride} \parallel (11\bar{2}0)_{sapphire}$
Mismatch to InN	-25.4%	29.3%
Mismatch to GaN	-33.0%	16.0%
Mismatch to AlN	-34.6%	13.3%

Table 3.4: *Lattice mismatch of nitride materials to sapphire in the two possible orientations. Taken from [76].*

the (0001) sapphire surface [93].

InN is a different case. Since $(10\bar{1}0)_{InN} \parallel (10\bar{1}0)_{sapphire}$ has a lattice mismatch comparable to $(10\bar{1}0)_{InN} \parallel (11\bar{2}0)_{sapphire}$, InN layers grown on c-plane sapphire contain nuclei with unit cells oriented with both the possible directions [76]. In fact, InN grown on (0001) sapphire without nitridation is polycrystalline [94, 95].

On the other hand, InN grown on nitrided sapphire (0001) surfaces grows single crystalline, because it grows epitaxial with respect to AlN resulting in $(10\bar{1}0)_{InN} \parallel (11\bar{2}0)_{sapphire}$). Thus, sapphire nitridation is necessary prior to growth of InN.

3.2.3 MOVPE of InN

InN epitaxy represent an even tougher challenge than GaN epitaxy. Beside the problems that are implicit in the lack of a matched substrate, InN has an even higher nitrogen equilibrium pressure than GaN [96]. This leads to low thermal decomposition temperatures, as low as 550°C [97]. In addition, ammonia requires very high temperatures in order to react. In fact, even if from a thermodynamic point of view ammonia (the Nitrogen precursor) should decompose[2] already at room temperature, due to a high activation energy it is very stable even at much higher temperatures. In the case of homoepitaxy of GaN, the growth rate is kinetically limited up to temperatures as high as 800°C, as shown in Fig. 3.10 [98]. Below that temperature the growth rate is kinetically limited because of incomplete ammonia decomposition. Alternative precursors for Nitrogen are hydrazine and its various derivatives, but, to the best knowledge of the author, there are no successful reports of InN growth with any derivative of hydrazine. TMIn is chosen as Indium precursor. A very important parameter for the growth is the V/III ratio (in this case the molar ratio between NH_3 and TMIn). The first reports of successful InN growth insisted on a very high V/III (starting from 10^5 and as high as 10^6) to suppress In droplets. An important

[2]The term *decomposition* is widely used in this context by several other authors, but it should be actually carefully considered. Ammonia decomposition in the gas phase leads to the formation of hydrogen and nitrogen molecules. This process does not supply nitrogen atoms for the growth of nitride materials because molecular nitrogen is extremely stable; on the contrary, ammonia is *activated*, in the sense that it first reacts to radical $\cdot NH_2$. Radicals can form either in the gas phase after reacting with other radicals (for example originating from the less stable metal-organic V-compound precursors) or after a catalytic process on the surface. Afterward, with a similar mechanism, the $\cdot NH_2$ radical looses the remaining hydrogen atoms and when on the surface it has a chance to reach the right lattice position and to contribute to the growth. As an alternative, ammonia molecules could also find the Nitrogen lattice position and loose the hydrogen atoms afterwards. The process is in fact, not simple and not exactly a *decomposition*.

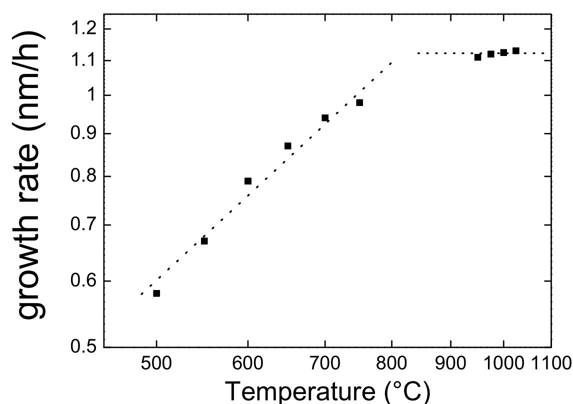

Figure 3.10: *Growth rate of GaN at different temperatures by using 0.135 mol/min ammonia and 17 μmol TEGa at 100 mbar reactor pressure. The growth rate is kinetically limited up to ∼800°C. Since TEGa is completely decomposed below the investigated temperature range by beta-elimination, ammonia decomposition is limiting the growth rate. Datapoints taken from [98].*

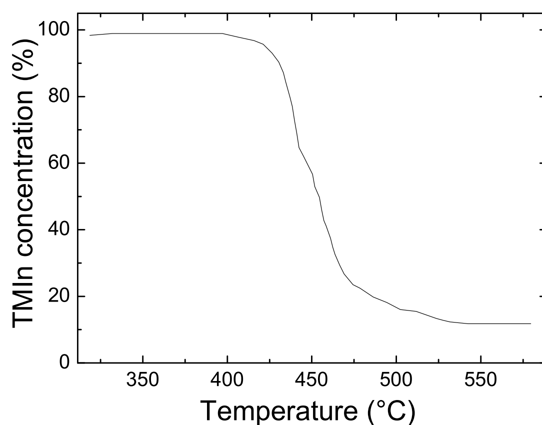

Figure 3.11: *Pyrolisis of TMIn as observed from UV-spectroscopy at 200 nm. Data taken from reference [99].*

contribution came from Maleyre et al. where the lowest V/III ratio of 5×10^3 was demonstrated for successful growth of InN [85] (see Fig. 3.13 on page 35).

The temperature window for MOVPE of InN is very narrow and it is a critical parameter. Almost every study on MOVPE of InN demonstrates a strong dependence of the growth rate and of the material properties on the growth temperature. Unfortunately, any comparison of the growth temperatures in different MOVPE reactors is difficult, due to the unique characteristics of every single MOVPE reactor and especially to the method of measuring temperatures [100, 101]. It is anyway very useful to examine closely the existing results.

InN electrical properties (Hall measurements) are best at the highest successful growth temperature of 600°C as reported by Keller et al. [102]. A strong dependence between the InN surface morphology and the growth temperature was reported by Yamamoto et al. [103]. They show that the highest growth temperature of 650°C leads to larger grains and smoother morphology. Growth from 520°C to 590°C in a system with increased velocity of the reactant gas is reported by Yang and co-authors [104]. They demonstrate a morphology dependence similar to the one given by Yamamoto et al. [103], resulting also in best crystallographic properties, as shown by the full width at half maximum (FWHM) of X-ray rocking curves of the (0002) reflection, for temperatures around 550°C. Photoluminescence (PL) and Hall mobility/carrier concentration are best at the highest growth temperature of ~600°C as reported from Sugita et al. [105]. Yamamoto et al. examined this topic again in 2004, studying samples grown between 450°C and 620°C. Again, best electrical and optical properties are found for layers grown at high temperature, respectively 600°C and 620°C [106]. Maleyre et al. do not report about temperature studies, their growth temperature is 550°C [55, 85]. Finally, in the range 540°C to 580°C Jain et al. [89] indicated 560 °C as the best growth temperature after characterisation by X-ray diffraction along the (0002) direction. At the highest investigated temperatures growth is often not observed at all due to InN desorption. Most often the results summarised above indicate the highest investigated/allowed temperatures (or close to) as best for InN.

The unwanted peeling off (also called delamination) of parts of the InN layer from sapphire substrates is a well known subject. Though it is apparently related to epitaxial growth in general, it is only reported in literature for MOVPE growth [88, 89, 107, 108]. Residual strain in thin InN layers grown on thin AlN/sapphire nucleation layers was characterised by Jain et al. [108] who reported that the InN layers are subject to tensile strain during growth. Since the lattice mismatch with both sapphire and AlN is actually positive (+28.6% and +11.5%, respectively) compressive strain was expected. The authors concluded that such tensile strain must be due to the coalescence of the crystallites but they could not conclude on the actual layer peeling off mechanism. Layer peeling off was occurring at 0.2 GPa tensile stress, since AlN does not delaminate at a stress of 1 GPa adhesion of InN on sapphire can be considered very poor. In their cases the layer peeling off occurred typically at a thickness around 200 nm. Almost every publication found in the literature suggests a GaN [88] or an AlN [89] nucleation or buffer layer to prevent the peeling off effect. On the other hand Maleyre et al. are able to grow thick layers (up to 1 μm) directly on nitridated sapphire without InN peeling off [85]. They also reported later that such InN layers possess better electronic properties than layers grown on any other nucleation layer (in MOVPE systems), as determined by Hall measurements [55].

Normally InN is grown at low pressures, ranging from 100 mbar to 200 mbar.

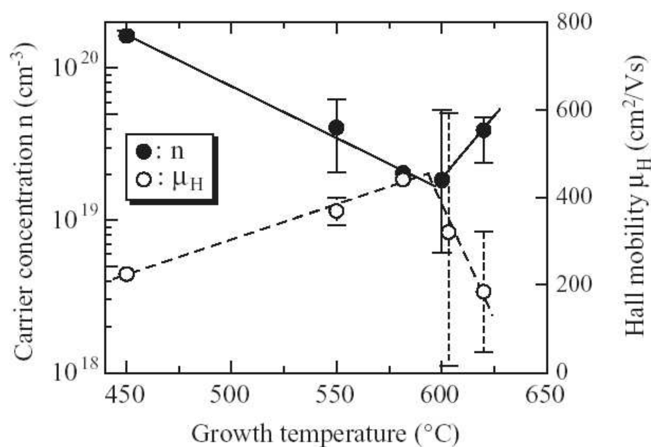

Figure 3.12: *Hall measurements on InN layers grown at different temperature. Highest carrier mobility and lowest carrier concentration is achieved for layers grown at 600°C These results are well correlated with photoluminescence measurements which can be found also in reference [106].*

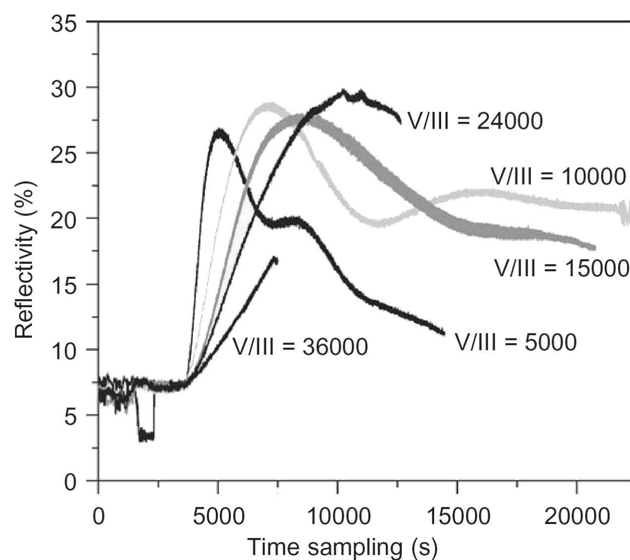

Figure 3.13: *Reflectivity measurements during InN growth on sapphire with different V/III ratios. The period of the oscillations becomes smaller by decreasing the V/III ratio and the amplitude of the oscillations decreases with the increasing thickness of the growing InN layer. The lowest V/III ratio (5000) leads anyway to a quick drop in reflectance, which is probably due to roughening of the surface. Taken from [85].*

Recently, Yamamoto et al. reported improvements for growth at atmospheric pressure [109].

3.2.4 MBE of InN

Molecular Beam Epitaxy (MBE) is a crystal growth technique which operate at pressures compatible with Ultra High Vacuum (UHV) systems. The most important difference between MBE and MOVPE for growth of InN is the nitrogen source. While MOVPE uses ammonia, MBE typically uses a nitrogen plasma (plasma assisted, PA-MBE). The supply of Nitrogen atoms from a plasma does not depend on the substrate temperature, which can be kept below 550°C, when InN is desorbing. For this reason PA-MBE turns out to be an efficient method for the growth of InN layers, with much progress in the last 6 years [90, 110]. Presently the best InN epitaxial layers (i.e. highest mobility, better morphologies, best crystallinity) are grown with this technique. There is also a claim of successful p-doping for MBE grown InN layers [111] by Magnesium acceptors (though the problem of the high electron accumulation at the surface has not been solved yet).

3.3 The initial growth procedure

When InN activity started at the TU-Berlin, there were only few literature reports on epitaxy of InN. The first challenge was the growth of an epitaxial, single crystalline layer which could be used as a starting point. The use of spectroscopic ellipsometry led to fast determination of a set of parameters which led to InN layers with good optical properties. These, together with crystalline properties were in very good agreement with other recent investigations on InN. The author achieved these first results in collaboration with Dr. T. Schmidtling and further discussion can be found in [81, 95]. The growth parameters used typically in these first epitaxies are summarized in table 3.5.

PARAMETER	NUCLEATION	EPITAXY
Temperature (°C)	400	500
Pressure (mbar)	100	100
TMIn (mmol/min)	$7 \cdot 10^{-4}$	$1.4 \cdot 10^{-3}$
ammonia (mmol/min)	41	41
V/III ratio	60000	30000
growth rate (nm/Hr)	30	60
typical thickness (nm)	15	100

Table 3.5: *Details of the MOVPE parameters used for the InN layers investigated in this chapter. After growth of the nucleation layer, the temperature was increased to 500°C where the main layer growth took place. This procedure was adopted for the first growth runs.*

Where not otherwise specified, the investigations reported in this and the next chapters refer to growth experiments using the procedure outlined in table 3.5.

The reason for the small thickness of these layers (circa 100 nm) lies on strong deterioration of the InN surface when the layers were grown thicker than ∼120 nm. Also, the crystal quality was not yet optimal (FWHM of the X-Ray diffraction rocking curve on the (0002) reflection was typically ∼1°) and the surface was often covered by small droplets of metallic Indium and by small crystallites. Additionally, due to the high V/III ratio (used to decrease the chance of forming metallic Indium droplets on the surface of the growing layer) the growth rate for these layers was very low. Anyway, before the optimization of the growth parameters and the development of a more advanced growth procedure, fundamental issues like the formation of large defects (holes) and the thermal stability had to be clarified. These topics are discussed in the following chapters.

4. Morphology issues

Morphology of InN layers is a severe issue. InN layers appear very often with large holes, crystallites and Indium droplets. Because of the importance of this problem, the discussion of the results starts with a chapter dedicated to it.

4.1 Layer peeling off

Highly mismatched systems can produce unwanted lifting of parts of the epitaxial layer due to a discontinuous substrate/layer interface resulting finally in the formation of cracks. These cracks increase in size and lead to formation of large holes in the InN layers. The consequent deterioration of the epitaxial layer is severe. This phenomenon is often called *layer peeling off*, or *layer delamination*. As reported in chapter 3 the tensile strain accumulated by coalescence of the initial nuclei seems to be the origin of the layer peeling off [108]. Since often the mismatch between substrate and epitaxial layer is not only in the lattice constant but also in the thermal expansion coefficient (the case of InN/sapphire), from ex-situ analysis it is difficult to determine when peeling off occurs, if during growth or during cooling down to room temperature. Therefore, this paragraph presents an in-situ analysis of InN peeling off together with ex-situ characterization for completeness.

In Fig. 4.1 transients of the reflected light intensity and of the imaginary part of the pseudodielectric function $\langle \varepsilon_2 \rangle$ at 5 eV, recorded during growth at 500°C, are given. The intensity of the reflected light (Fig. 4.1, top) is the measured value of the Stokes parameter usually labelled S_0 [112], that measures the sum of the intensity of the light having all possible polarization. In this sense, it is clear that S_0 is proportional to reflectivity measured at a non-normal angle of incidence.

The intensity of the reflected light in Fig. 4.1 shows initially a dependence from the layer thickness due to features originating from Fabry−Perot interference and remains subsequently almost constant up to about 200 minutes growth duration. $\langle \varepsilon_2 \rangle$ shows essentially the same behaviour. In particular, V/III ratio was varied between 9×10^5 and 3×10^5, temperature of nucleation and of growth from 450°C and 530°C. At t_1 , corresponding to a layer thickness of about 150 nm, a sudden decrease occurs. The reflectivity drops and does not recover while $\langle \varepsilon_2 \rangle$ shows a sudden drop and then recovers roughly to the original value. Both indicate a deterioration of the layer.

This behavior is surprising if one expects the normal evolution of the transient under standard epitaxial growth conditions. At the energy of the transient one would expect only slow increase or decrease of the intensity of the reflected light and of $\langle \varepsilon_2 \rangle$, which means respectively an improvement or a deterioration of the surface and of the crystalline properties. The behavior of the transients in Fig. 4.1 is clear indication of some drastic event for the quality of the growing InN layer.

Scanning Electron Microscope (SEM) images taken from a sample grown up to t_1

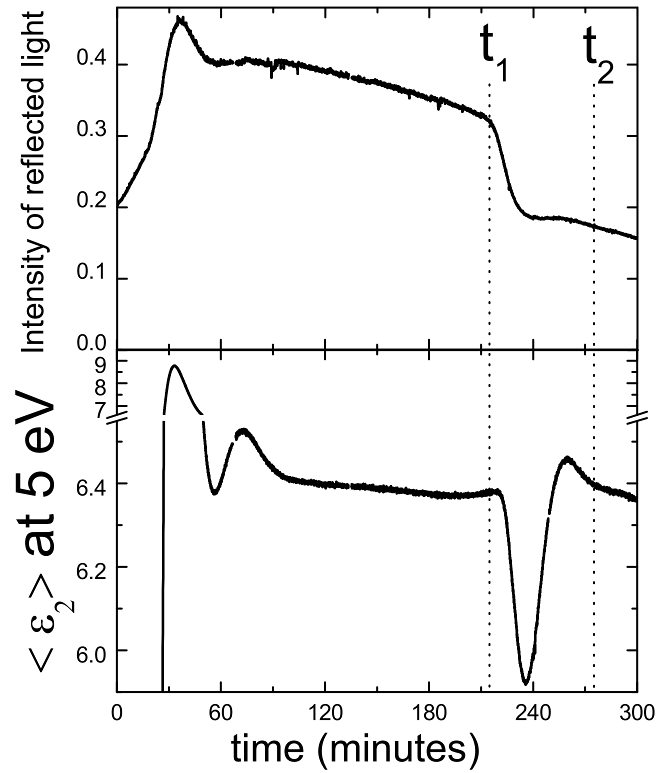

Figure 4.1: *Transients of the intensity of the reflected light (top) and of the effective dielectric function $\langle \varepsilon_2 \rangle$ (bottom) recorded in-situ at fixed energy (5 eV) and 500°C growth temperature. Time t_1 (InN layer thickness ~120 nm) and t_2 (InN thickness ~150 nm) refer to surface morphologies shown in Fig. 4.2.*

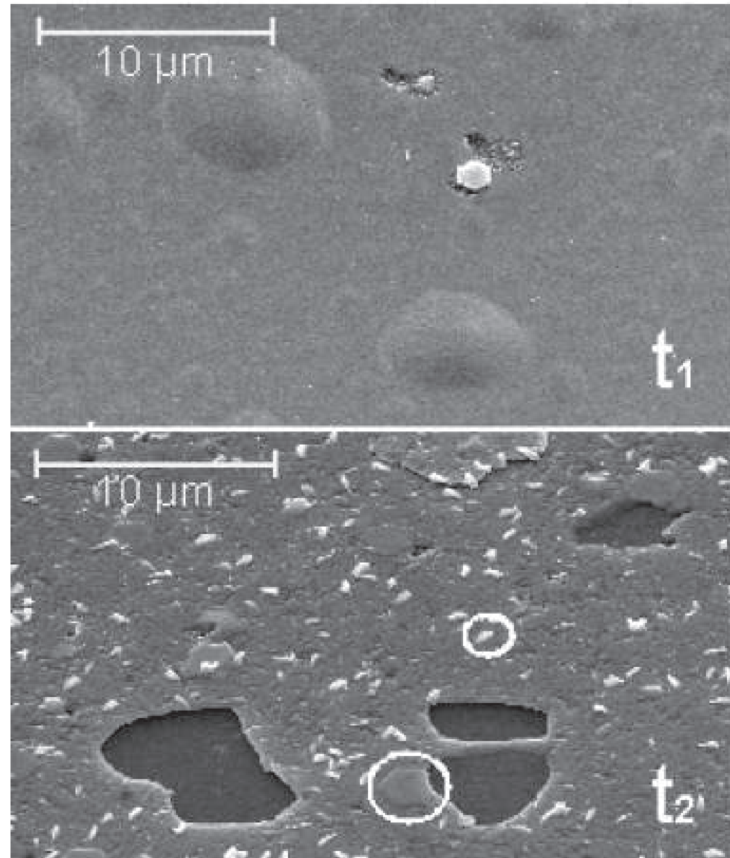

Figure 4.2: *SEM images showing InN surfaces at different thicknesses: ∼120 nm at growth time t_1 and ∼150 nm at t_2. t_1 and t_2 refer to the growth time and to the thicknesses indicated in the transient in Fig. 4.1. At t_1 (top) the surface partially bulges, some evidence of peeling off is present. At a later time t_2 (bottom) the layer is disrupted by holes. Crystallites of different size and shape are marked by white circles.*

show that the surface partially bulges (Fig. 4.2 top). This feature is not observed in thinner layers (i.e. at shorter growth times) and indicates an onset of peeling off of parts of the layer. Hence, holes originating from the peeled off material are found in thicker layers with a longer growth time, t_2 as an example (Fig. 4.2, bottom). Thus, the decrease of the reflected light intensity (Fig. 4.1, top) is a result of roughening on the micrometer scale due to the occurrence of holes in the layer, while the recovery of $\langle \varepsilon_2 \rangle$ (Fig. 4.1, bottom) after t_1 is due to the growth of a new InN layer on the bare sapphire substrate in the holes. The recovery is almost complete and by this, $\langle \varepsilon_2 \rangle$ shows also to be unaffected by roughness on the micrometer scale.

The critical thickness for the onset of the peeling off depends on the growth parameters like temperature and growth rate and may occur already at 100 nm. It should be noted that the peeling off was always observed for InN samples thicker than 150 nm (grown longer than t_1 referring to Fig. 4.1), and ellipsometry was crucial in determining the critical thickness. The adhesive strength of the low temperature InN nucleation layer layer is apparently too low to counteract the strain in the layer accumulated up to 150 nm. It can be also concluded that the peeling off of the InN layer occurs already during growth, due to the lattice mismatch between InN and sapphire and not during cooling down, due to the thermal expansion difference between layer and substrate.

Given these facts, there has been a strong focus on the suppression of the layer peeling off for the InN/sapphire system. A positive result was achieved by using Nitrogen as carrier gas instead of Hydrogen during nitridation of the sapphire nitridation with ammonia. Scanning Electron Microscopy (SEM) and optical microscopy investigations show that when Nitrogen is used as carrier gas the concentration of holes of large dimensions ($>3\,\mu m^2$) decreases by more than a factor of 20 (to less than 1 per $1.5\times10^3\,\mu m^2$). Holes of smaller dimensions ($<1.5\,\mu m^2$) are still present, indicating that the correct surface preparation of the sapphire substrate remains a critical issue for achieving improved InN crystal quality. Fig. 4.3 shows typical SEM morphologies for two InN layers ∼350 nm thick as grown on sapphire after nitridation performed with hydrogen (top) and nitrogen (bottom). Proper substrate surface preparation and the nucleation determines in fact the degree of adhesion of the epitaxial layer onto the substrate.

Also the effects of different initial growth conditions (nucleation) were studied: ammonia and TMIn have been introduced into the reactor at the same time, or one of the two with a certain time delay. The layer peeling off resulted to be independent from the different initial nucleations after optical microscopy investigations. The use of different nucleation temperatures (namely 375°C, 400°C, 500°C and 530°C) also did not influence the layer peeling off. Nucleation above 540°C leads in our case to very rough morphologies and In droplet formation on the surface. Finally, there was no dependence of the layer peeling off from the studied nucleation conditions. The nucleation results are discussed in more detail in Chapter 7.

In summary, it can be concluded that several attempts to vary growth condition, i.e. buffer layer, carrier gas composition, initial nucleation and nucleation temperature did not result in the complete suppression of peeling-off of InN.

InN layers with thickness above 300 nm were grown without layer peeling off on a GaN buffer 300 nm thick. In this case, a more continuous InN/GaN interface may be

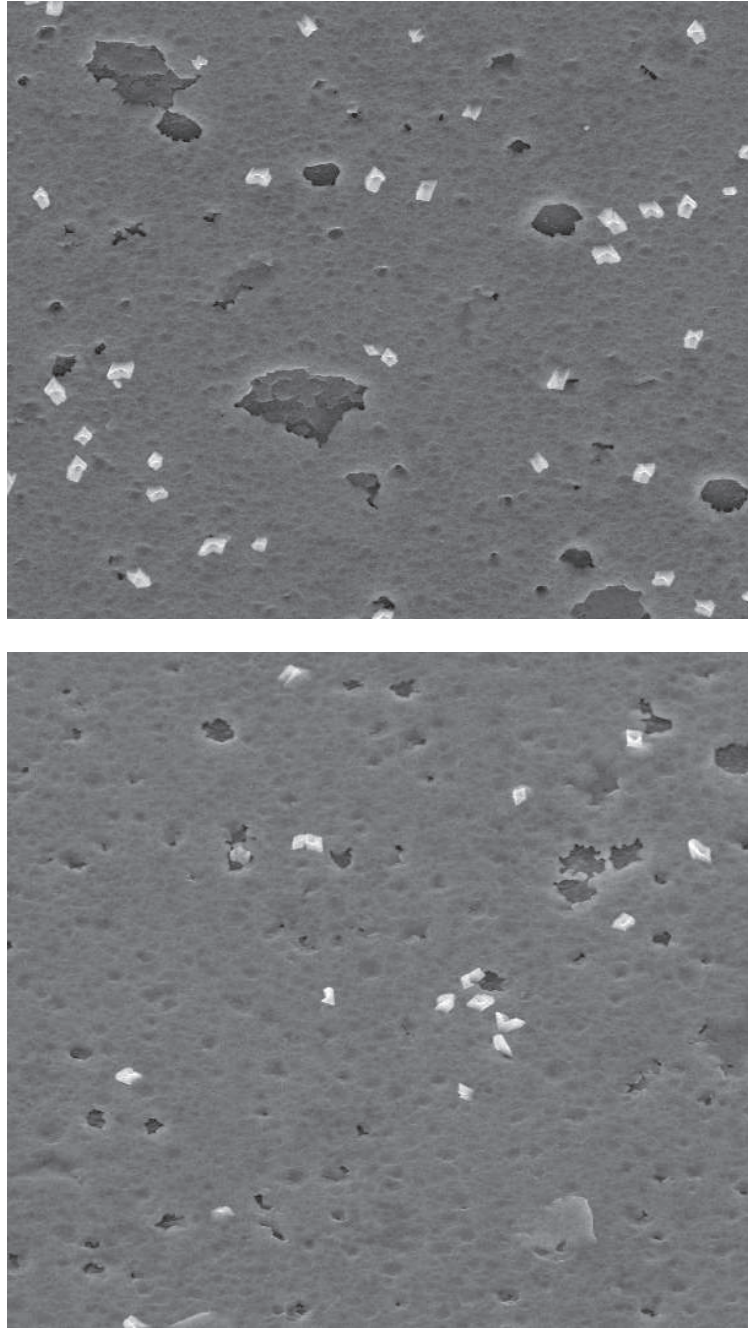

Figure 4.3: *$(15\times15)\,\mu m^2$ SEM images showing surfaces of InN layers grown with different nitridation of the sapphire substrates. For the InN surface pictured on top, nitridation was performed using hydrogen as carrier gas: the surface is characterized by large holes in large numbers, together with several smaller crystallites (white). For the InN surface pictured below, nitrogen was used as carrier gas during nitridation of sapphire: the number and size of the macroscopic defects is strongly reduced.*

responsible for suppression of peeling off of the InN layer (at least up to 300 nm). This is shown in a typical cross-section SEM image of this layer in Fig. 4.4. The InN/GaN interface seems to be continuous and there is no hint of layer peeling off. The growth of InN on GaN is anyway not free of challenges, and the GaN surface grown prior to the InN growth is often not as well defined as the sapphire nitridated surface. The reader can find more details on the growth of InN on GaN templates in Chapter 7.

The ammonia flux was also varied to determine its effects on layer peeling off when growing on sapphire. Due to the low growth rates achieved with the high V/III ratios, a generally high flux of precursors (both ammonia and TMIn) is used to ensure higher supersaturations, thus higher growth rates. The ammonia flux was reduced (and, as a consequence, the V/III ratio was also reduced) by a factor of three (from 3 L/min down to 1 L/min). All the other parameters were, in this case, constant through the whole growth (i.e. no nucleation layer). This procedure (fixed parameters through all the growth) normally leads to layer peeling off at ~120 nm when 3 L/min ammonia are used. With 1 L/min ammonia two different InN layer were grown with a thickness of 300 nm and 350 nm, respectively. They reveal high growth rates (~220 nm/hour: 2 times larger than when 3 L/min ammonia are used) and virtually no layer peeling off, as determined by optical microscopy and by AFM: as shown in Fig. 4.5 the surface is free of the large defects due to layer peeling off. High ammonia fluxes were in fact found to lead to lower growth rates [113] and, as will be shown in the next paragraph, InN is unstable under ammonia stabilization at high temperatures. This leads to the conclusion that ammonia in high concentration etches the InN layer, leading in the

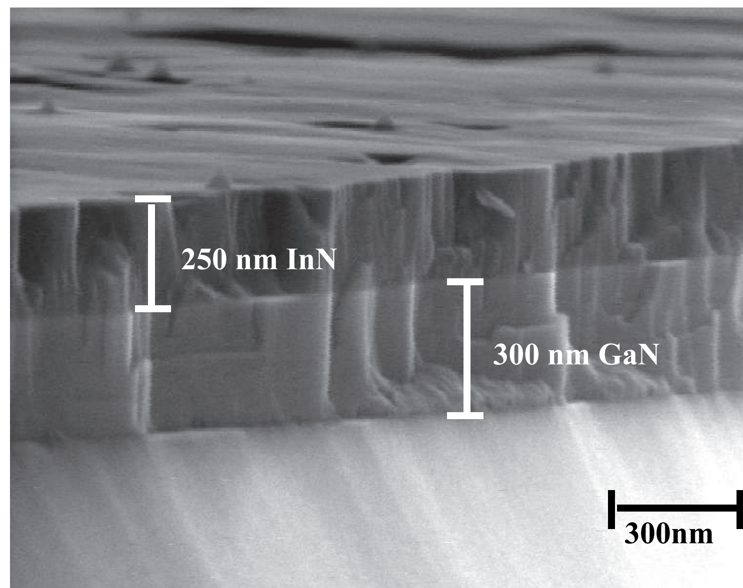

Figure 4.4: *250 nm thick InN grown on top of a 300 nm thick GaN template. The InN/GaN interface appears to be continuous, the surface of InN do not show layer peeling off.*

early stage of growth to a non-continuous substrate/InN interface and to layer peeling off at coalescence.

On the other hand, the measured effective dielectric function of these layers shows significant differences with respect to samples grown with high ammonia flux. This section has focused on the layer peeling off and will be concluded here, by stressing the importance of keeping low the total flow of ammonia during nucleation of InN on sapphire. The properties of these layers, grown with a low ammonia flux, will be discussed in more detail later, in Chapter 7.

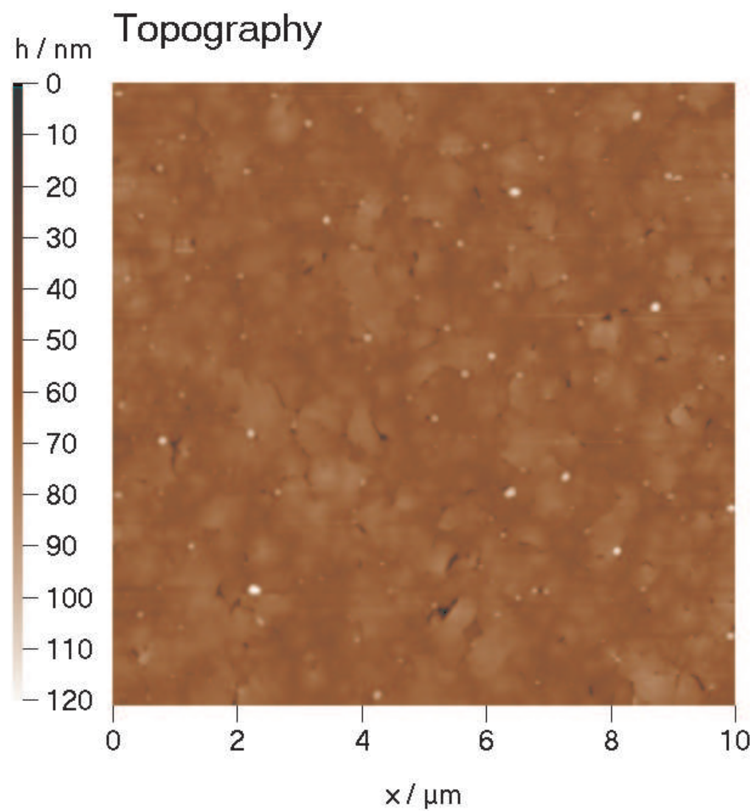

Figure 4.5: *AFM image of an InN/sapphire layer grown at 520°C using a low flux of ammonia: 1 L/min (V/III ratio was 10×10^5). The (10×10) µm^2 image on the left shows no peeling off. rms roughness on (1×1)µm^2 images is ∼3 nm. Morphology is dominated by large terraces. The round shaped spots are probably metallic Indium droplets.*

4.2 Parasitic nucleation and droplets formation

The surface morphology displayed in Fig. 4.2 (bottom) shows flat hexagonal crystallites with a large diameter in the μm range and irregular smaller crystallites. The large holes originating from layer peeling off (described above) could become seeds for parasitic nucleation resulting in three-dimensional growth of the flat hexagons, as indicated by the hexagonal crystallite marked in Fig. 4.2 (bottom). In fact a large number of the hexagonal crystallites can be found in samples grown beyond the onset of the layer peeling off (t_1), with a density of 10^7 cm^{-2}, while for samples grown just below the peeling off edge (like the sample showed in Fig. 4.2, top) they occur with a lower area density, below 10^4 cm^{-2}, and are completely absent in thinner samples. The irregular crystallites are about 10 times smaller in size than the hexagonal ones and have a broad size distribution. SEM images of samples with various thicknesses show that some arise already at initial stages of the growth, others later due to parasitic nucleation. Here temperature plays an important role to control the appearance of such defects. A growth temperature increase of ΔT=20°C reduces the density of these defects by two orders of magnitude, from 5×10^7 cm^{-2} to 5×10^5 cm^{-2}.

Another typical issue of the morphology of InN layers is represented by the formation of metallic Indium droplets. An example of droplets imaged by SEM is shown on Fig. 4.6. Typically, a small V/III ratio leads to formation of droplets of metallic Indium, followed by 3-D growth and roughening of the surface. Though this issue was not thoroughly characterized, the droplet formation is normally not a problem above a V/III ratio of 3×10^5. Different ammonia fluxes might influence this limit, as well as other growth parameters might also do. Ellipsometry is in principle very powerful in the recognition of thin overlayers and droplets as well, but for a correct interpretation of the spectra measured in-situ the dielectric properties of InN must be known.

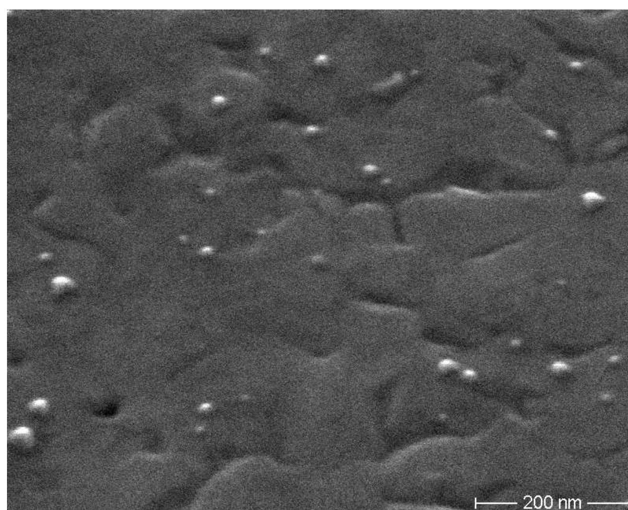

Figure 4.6: *SEM image of an InN/sapphire layer grown at 500°C using a V/III ratio of 3×10^5. The round shaped spots are metallic Indium droplets.*

4.3 Chapter summary

We have discussed the most prominent morphology problems of MOVPE grown InN layers. Layer peeling off can be strongly reduced by using nitrogen as carrier gas during nitridation of the sapphire substrate. It can be suppressed by using a low flux of ammonia during nucleation of InN on sapphire. Alternatively, InN grown can be grown on GaN/sapphire without peeling off (up to 300 nm thick InN layers). Higher growth temperature can reduce the formation of crystallites from parasitic nucleation, while a high V/III is critical in order to suppress the formation of Indium droplets.

5. Thermal stability and annealing

This chapter deals with the thermal stability of InN in different gas ambients (nitrogen, hydrogen and ammonia) of MOVPE. Knowledge of this issue is critical in order to improve the properties of InN epitaxial layers in MOVPE. The second part of this chapter concentrates on an annealing experiment in nitrogen ambient, which results to be the most suitable. The aim is to evaluate the annealing as a possible growth step in the growth procedure of InN, analogous to GaN growth.

5.1 Thermal stability in different gas ambients

Thermal stability of InN is found to be extremely low due to the high atomic Nitrogen equilibrium pressure [96]. Thus, to find optimal growth conditions it is extremely important to determine under which conditions, of temperature and of gas ambient, is possible to control the surface of the epitaxial layer. In a MOVPE reactor the most common gas ambients are the carrier gases nitrogen and hydrogen. Beside them, ammonia is also important for nitrides since it is the precursor of atomic Nitrogen. Thus, this section presents studies of the thermal stability of InN upon different conditions of temperature and gas ambient. It is also interesting to find annealing conditions where the thin InN epitaxial layer might smoothen and re-crystallize, (similar to GaN [82, 114]) to give rise to a surface with characteristics which are ideal for the growth of the thicker InN epitaxial layer on top.

Thermal stability experiments were performed in the MOVPE reactor at 100 mbar and monitored in-situ with spectroscopic ellipsometry. Since air exposed InN layers show irreversible changes in the optical properties [115] we focus here on the annealing of freshly grown samples. Optical spectra of these InN layers generally resembles the one shown in Fig. 2.8, showing interferences appearing above the bandgap and below the higher electronic interband transitions. The results are presented in terms of the imaginary part of the effective dielectric function $\langle \varepsilon_2 \rangle$.

5.1.1 Nitrogen ambient

When InN is heated in nitrogen at 100 mbar and temperatures up to 520°C, a thermally induced red shift and broadening of the interband transitions is observed. This process is completely reversible. As shown in Fig. 5.1, during annealing at 540°C the interferences below 4 eV are changing. This suggests a reduction of the layer thickness due to desorption. Exposing the layer up to 20 minutes to a maximum temperature of 540°C results in a slow increase of the amplitude of the interband transitions. Annealing longer than 20 minutes always leads to a subsequent decrease of the amplitude, indicating a deterioration of the layer. Above 540°C the sample deterioration begins

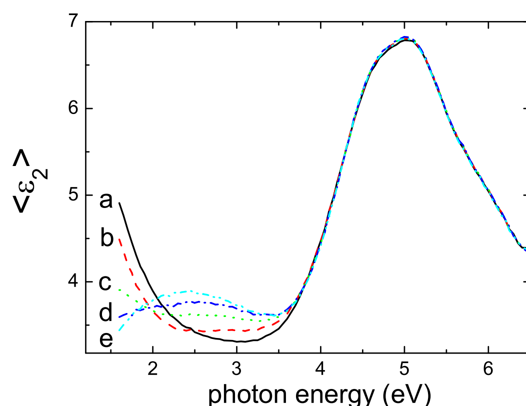

Figure 5.1: *Spectra of $\langle \varepsilon_2 \rangle$ during annealing of InN/sapphire in a nitrogen ambient. Spectrum (a) was measured at 530°; (b) after 1 minute at 540°C; (c) after 7 minutes; (d) after 13 minutes; (e) after 19 minutes. The change in the low energy range (below 4 eV) indicates a change in thickness. The slight increase at ∼5 eV shows decreasing roughness or improving crystal quality.*

already after much shorter exposure time (e.g. after 5 minutes at 550°C). The effects of thermal annealing of InN at 540°C are discussed in detail in section 5.2.

5.1.2 Hydrogen ambient

Figure 5.2 shows a transient of $\langle \varepsilon_2 \rangle$ at a fixed photon energy of 5 eV, i.e. in the E_1 and E_2 energy range. The temperature was increased linearly with time as indicated on the scale above the spectra. The evolution of the transient can be divided in three different regions. In the first region a linear increase of the amplitude is observed. This trend originates from the red shift of the interband transitions and is not related to structural changes. The second region shows a clear change of the transient evolution: at T∼340°C the amplitude of $\langle \varepsilon_2 \rangle$ starts to decrease slowly with a progressive slope at increased temperature. Inspection of the samples after this phase shows surfaces covered with Indium droplets. In the third region the carrier gas has been switched to nitrogen. An apparent recovery in the amplitude is observed, despite a further increase in the temperature. It should be noted, however, that recovery was not complete and a partial surface damage remained. It might seem surprising that hydrogen is affecting layer stability already at these low temperatures (below 400°C). But so far, there are no reports of good quality InN layers grown by MOVPE using hydrogen as carrier gas [77, 116]. In fact, according to thermodynamic studies, hydrogen is expected to limit InN growth [117]. Therefore, hydrogen etches InN at temperatures lower than the desorption temperature determined in nitrogen ambient.

In addition to the in-situ transient, in Fig. 5.3 room temperature spectra of $\langle \varepsilon_2 \rangle$

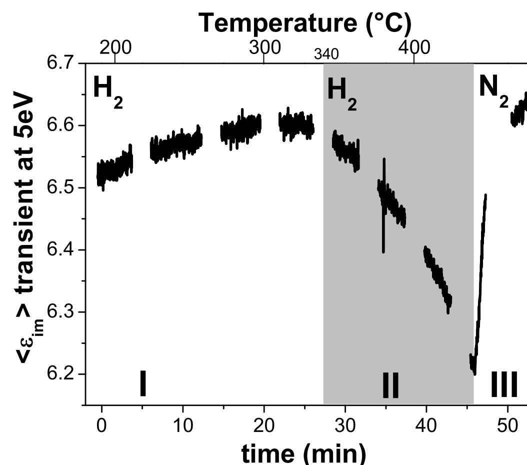

Figure 5.2: *Transient at 5 eV of $\langle\varepsilon_2\rangle$ during annealing of an InN layer in a hydrogen ambient. In region I the change in the optical properties is only due to the reversible shift and broadening of the interband transitions with increasing temperature. In region II, at a temperature of ~340°C, the amplitude drops, indicating deterioration of the layer. In region III the properties recover partially when the hydrogen ambient is exchanged with an inert nitrogen ambient. Inspection of the surface after annealing reveals increase of roughness and droplets*

show the effect of annealing in hydrogen. The thicker line belongs to the InN layer as grown. The dashed line belongs to $\langle\varepsilon_2\rangle$ of the layer after 15 minutes at 330°C in hydrogen ambient. Since the amplitude of the high interband transitions decreased strongly we can conclude that the InN layer deteriorated. A partial recovery is possible after annealing at 540°C in a nitrogen ambient showing that annealing in nitrogen ambient is more advantageous.

5.1.3 Ammonia ambient

The effect of ammonia on InN layers was studied by supplying 5 to 75 mbar partial pressure, in a total pressure of 100 mbar in nitrogen ambient. Layers exposed to ammonia were never found to show improved morphology or better optical properties with respect to untreated layers. Irreversible changes in $\langle\varepsilon_2\rangle$ spectra and a decrease of the interband transition amplitudes occurred at temperatures as low as 520°C at high ammonia partial pressure (75 mbar), as shown in Fig. 5.4. Droplet formation occurred also generally faster than in experiments without ammonia. The temperature onset for desorption in the presence of ammonia is between 520°C and 550°C, slightly earlier compared to nitrogen ambient. This fact is not surprising, since the growth rate was recently found to be inversely proportional to ammonia flux [113].

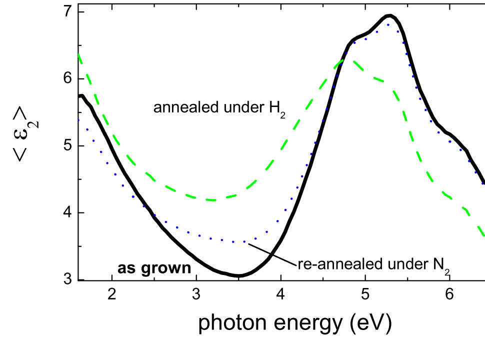

Figure 5.3: *In-situ spectra at room temperature of an InN layer as grown (full line), annealed in hydrogen up to 325°C (dashed), re-annealed in nitrogen at 540°C (dotted). Hydrogen reduces the amplitude of the higher interband transitions. Even by further annealing in nitrogen, there is no complete recovery of the initial amplitude.*

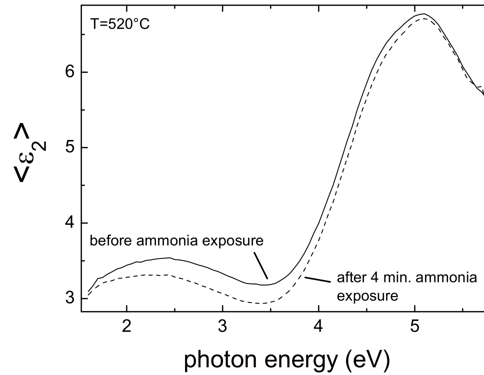

Figure 5.4: *In-situ spectra at 520°C of an InN layer as grown (full line) and after annealing in ammonia ambient for 4 minutes (dashed). Ammonia composition in the gas phase was 75%, 25% was nitrogen and total pressure was 100 mbar. The amplitude of the signal in $\langle \varepsilon_2 \rangle$ decreases over the whole energy range, indicating deterioration of the InN layer.*

Figure 5.5 summarizes the thermal stability of InN. Hydrogen etches the InN layer already at 350°C whereas in nitrogen ambient, which is completely inert, InN is stable up to ∼520°C. Ammonia, generally used to stabilize for example GaN well above its desorption temperature [81] in the case of InN appears to be ineffective in improving the InN thermal stability.

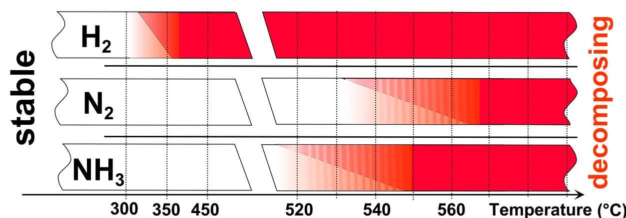

Figure 5.5: *Summarizing sketch of the thermal stability of InN in different ambients. In white areas InN is stable, in dark areas InN decomposes. In hydrogen InN decomposes above 340°C, in nitrogen above 540°C, in ammonia above 520°C.*

5.2 Annealing in nitrogen

Analogous to GaN epitaxy, high temperature annealing of a thin InN nucleation layer can lead to smoothing of the nucleation layer, as well as recrystallization of amorphous and cubic material. It can be a critical preparation for the epitaxial growth of high quality material on top of the annealed nucleation layer. After studies of the thermal stability of InN it is clear that the most suitable ambient for a high temperature annealing of the layers is nitrogen, since hydrogen and ammonia (which contains Hydrogen atoms as well) lead to earlier decomposition of the InN layers. Therefore, this section is dedicated to the effects on InN layers of annealing in nitrogen ambient.

The in-situ ellipsometric spectra measured during annealing of InN at 540°C were shown in Fig. 5.1. The amplitude at the high interband transitions do not change noticeably, while the interference structures slowly changes. This indicates reduction of the InN layer thickness, i.e. InN desorption. The amplitude at the high interband transition remains constant, which means no increasing of roughness during desorption. Thus, the desorption occurs layer by layer.

The spectra after 20 minutes annealing and cooling to room temperature are shown in Fig. 5.6. The energy range of the room temperature spectra is extended by ex-situ measurements performed with a commercial ellipsometer (SENTECH GmbH) operating in the near infrared, from 0.8 to 1.5 eV. There is good agreement between in-situ and ex-situ measurements.

The spectrum of the *annealed* sample is compared in Fig. 5.6 with its reference, labelled *as grown*. Both, *annealed* and *as grown* samples were grown in the same experiment, but only one of the two was annealed. The other one was used as reference. Observation of the spectra in the low energy range confirms a reduced thickness during annealing and a somewhat reduced amplitude of the interference structure. The latter probably originates from larger sample inhomogeneities generating a loss of phase coherency. On the other hand, above 4 eV, the interband transition amplitude increased considerably after annealing. The in-situ data did not show such improvement during the annealing at 540°C (at least until the last spectra measured after 19 minutes, see Fig. 5.1), mainly due to the damping of the critical points at high temperature. The improvement may originate from either the reduction of bulk defect density, or a reduction of surface roughness.

It is important to note that during annealing the InN layer undergoes a phenomena

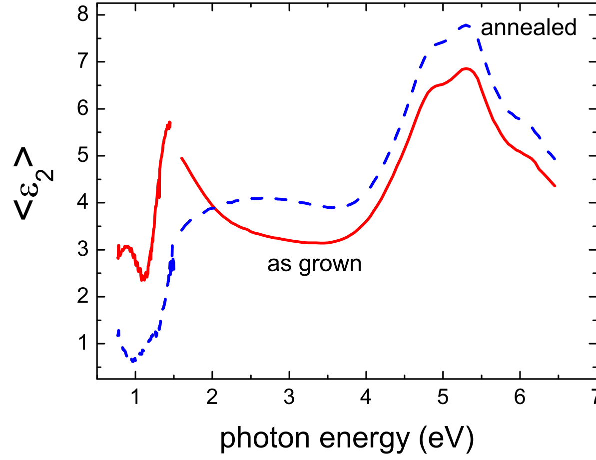

Figure 5.6: *Room temperature spectra of the sample as grown (solid line) and after annealing (dashed line), on the same position on the wafer. The measurement was performed with two different ellipsometers. Together with a decrease of thickness, the high interband transition have increased amplitude after annealing.*

close to the peeling-off described in the previous paragraph. In fact, SEM images of the InN layer after annealing shows a *bulging*, similar to Fig. 4.2. It was previously pointed that the lattice mismatch to the sapphire substrate is the origin of the stress inducing bulging and peeling off of the layer during growth. On the other hand, during annealing the changes in temperature induce additional stress, originating from the difference in thermal expansion of InN and sapphire. This additional contribution may already induce bulging in 100 nm thick layers, and therefore be responsible for layer bulging during annealing.

The XRD rocking curves (ω-scans) of the (00.2) reflections in Fig. 5.7 of the annealed samples display a broadening with respect to the reference (not annealed). Due to the scan geometry of the rocking curve, crystal planes belonging to parts of the InN layer that are "bulging"(i.e. that are bent with respect to the sample surface with a certain angle) are partially contributing to the X-rays reflection. Therefore, the curve of the annealed material is broader. The scans show an offset of the peak center between the annealed and the reference samples. This is due to a different alignment like a slight tilt (offset) of the sample on the sample holder. Such an offset is generally present in ω-2θ-scans (see Fig. 5.9) but not in 2θ-scans (Fig. 5.8). In 2θ-scans the angle is then only depending on the Bragg condition and one can calculate the lattice constant of the material under investigation. For ω-scans and ω-2θ-scans the peak shift can be due to alignment, thus it is not relevant.

2θ-scans are performed with a channel cut analyzer after the sample. This leads

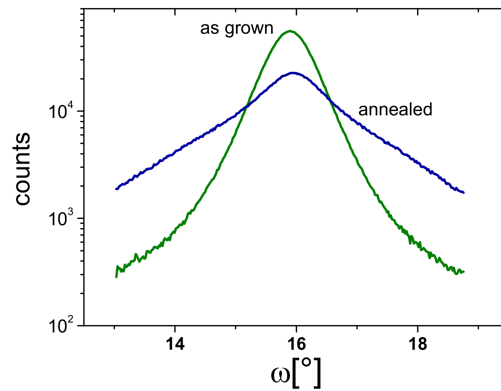

Figure 5.7: *XRD ω-scan of the annealed InN layer and of the reference layer. The measured curve of the annealed layer is broadened respect to the reference. The relative shift of the peak-center is due to a measurement offset.*

to a selection of the diffraction crystal planes, excluding the parts where the bulging occurs. In this case Fig. 5.8 shows no shift of peak position, but only a reduced overall intensity due to reduced thickness and to the missing contribution of the parts of the layer that are bulging.

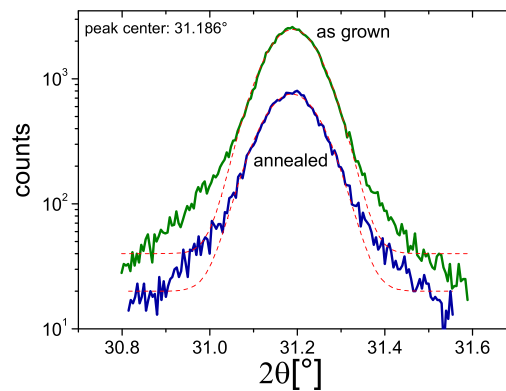

Figure 5.8: *XRD 2θ-scan of the annealed InN layer and of the reference layer. The two measured curves show, within measurement error, the same value for the peak center, indicating no change of the lattice constant of the layer due to annealing. Dashed lines are Gaussian fits.*

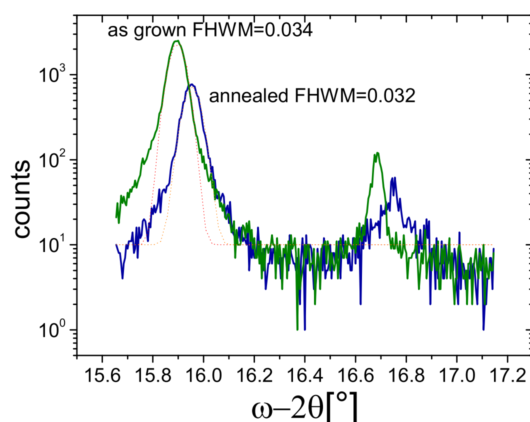

Figure 5.9: *XRD ω-2θ-scan of the annealed InN layer and of the reference layer. The two curves are shifted to each other because of a measurement offset. Each measurement shows a larger peak (left) due to the (00.2) InN reflection and a smaller peak (right), assigned to polycrystalline InN. After annealing, the FWHM of the InN peak shows only minor changes, as well as the amplitude ratio with the peak of polycrystalline InN .*

Finally, also ω-2θ-scans were measured, shown in Fig. 5.9. By using again a channel cut analyzer after the sample (as for the 2θ-scan), for the ω-2θ-scan the broadening of the X-ray reflection depends only on the perfection of the crystal planes parallel to the surface and not on the parts of the layer that are out of plane (i.e. bulging). The FWHM of the peaks is very similar for the annealed sample and for the reference. The peak visible on the right of both the graphs is often reported in literature and it was at first assigned to the cubic reflection of metallic Indium [53]. It has been recently argued that it actually belongs to different orientations of InN, in other words a sign for the content of polycrystalline material in the epitaxial layer [118]. In both cases it is due to extended defects in the layer and it can be taken as a measure of the crystalline quality. In the measurements shown in Fig. 5.9 the height ratio between the InN (00.2) peak and the foreign peak is comparable for reference and annealed sample, leading to the conclusion that no phase transition occurs at the detection level of X-Ray diffraction.

The annealed layer and the corresponding not-annealed reference were also investigated by TEM analysis [119]. In the reference layer (Fig. 5.10, top) it is possible to see three regions characterized by different contrast. The bottom region is the sapphire substrate. The intermediate region, around 100 nm thick, is the InN epitaxial layer. The top layer is an amorphous layer, probably formed by amorphous InN with inclusions of metallic Indium. In the annealed sample (Fig. 5.10, bottom) the amorphous overlayer is absent, resulting in an overall thinner InN layer with a smoother surface. Reference [119] reported also a photoluminescence study of the two

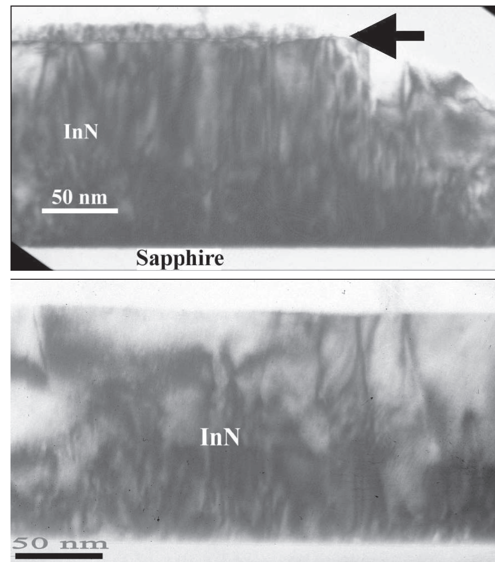

Figure 5.10: *TEM images of a cross section of the annealed InN layer (bottom) and of the reference layer (top). The reference layer is characterized by a defective, amorphous overlayer which is absent on the nitrogen annealed layer.*

InN samples, showing a slight increase of the intensity of the photoluminescence peak at about 0.9 eV after annealing. The last notable point of the two TEM images is that there is no hint of a re-crystallization due to annealing.

Hence, we conclude that the amplitude increase observed in the in-situ SE spectra does not originate from improvements of structural bulk properties.

Finally, Fig. 5.11 shows the surface morphology before (a) and after annealing (b). Two kinds of defects can be observed: grooves of the not yet completely closed layer and small crystallites with sizes of tens of nanometers. The latter almost completely disappeared on the annealed sample (Fig. 5.11 b), and the groves tend to close, obviously via coalescence by material transport. The overall result is a decrease in the surface roughness.

With the results of the ex-situ characterization and the $\langle \varepsilon_2 \rangle$ room temperature spectra in Fig. 5.6 it is possible to draw conclusions on annealing of InN in nitrogen ambient. The decrease in amplitude of the structures related to interferences below 4 eV in Fig. 5.6 can be addressed to layer bulging, also detected by SEM. Bulging causes an effective inhomogeneity, reducing phase coherence and dampening the interference structures. The interferences in the SE room temperature spectra show also a decrease in thickness of the InN layer, as indicated also by the spectra measured in-situ at 540°C (Fig. 5.1). This was confirmed by TEM cross section images, which have shown that a defective overlayer was removed by annealing, actually reducing the overall thickness of the InN layer and also by SEM images, which have shown the elimination of metallic Indium droplets and crystallites. Above 4 eV the amplitude of the high

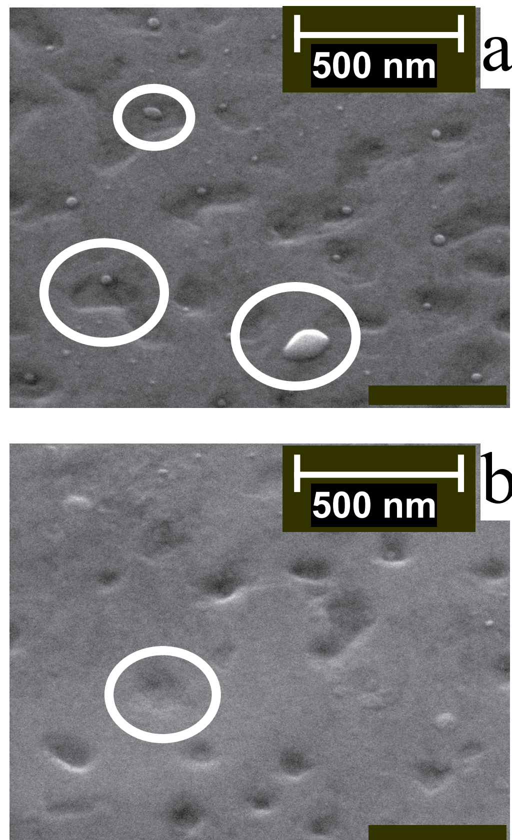

Figure 5.11: *SEM images of the surface of the annealed InN layer (a) and of the reference layer (b). The reference layer is characterized by droplets and crystallites of various size which are eliminated during annealing. Holes are visible in both images. They result from the not yet complete coalescence of the initial nuclei. The depth of the holes in the annealed layer seems to be smaller probably due to material transport which smooths the surface.*

interband transition did rise after annealing and TEM analysis showed the removal of the defective, rough overlayer (probably formed by metallic Indium and/or by polycrystalline/amorphous InN). As a consequence, the overall layer crystallinity also improved because of desorption of bad quality material. Anyway, it was not possible to detect any change in the lattice constant from 2θ-scans, neither a significant change in the peak broadening of the ω-2θ-scans. Thus, it is not possible to conclude towards a re-crystallization of the layer as it occurs, for example, during high-temperature annealing of GaN (GaN recrystallization occurs at temperatures as high as 900°C [82]). This is also due to the relatively good crystal quality of the as grown layers used for annealing, which were grown at 520°C. Concluding, the annealing of InN can be seen as a possible step in the direction of growth of InN, since smoothing of the

surface of a low-temperature grown nucleation layer leads closer to ideal conditions for growth of InN with improved quality.

5.3 Chapter summary

Thermal stability of InN was studied. The result is summarized in Fig. 5.5. Nitrogen results as the most suited ambient for annealing of InN layers. The annealing experiment at 540°C for 20 minutes have shown that surface morphology of InN can be strongly improved by annealing.

6. Substrate preparation: nitridation of sapphire

Nitridation is not only essential for the growth of InN on sapphire. The quality of GaN can be also improved using nitridation. For epitaxy of GaN layers the optimization of sapphire nitridation with ammonia proved to be crucial, yielding best results for short nitridation times (45 s to 60 s) at 1050°C [120, 121]. Progress in InN epitaxy requires establishement of an optimal nitridation procedure as well. This is even more critical than for GaN since it is shown experimentally that nitridation is necessary in order to grow single crystalline InN [95].

Sapphire nitridation can be performed in different ways, for example using cold nitrogen plasmas as sources of atomic nitrogen [23], but for standard MOVPE conditions ammonia is generally used (see for example [93], [122]).

Nitridation with ammonia forms a thin AlN layer on the sapphire surface [93, 122, 123]. The epitaxial orientation of the thin AlN layer with respect to the c-plane of sapphire corresponds to a 30° rotation of the nitride (0001) plane (c-plane) [93].

Literature data on the effects of nitridation on the properties of InN epitaxial layers are not complete. A 40 min nitridation in ammonia at 1000°C reported in earlier work leads to the best InN electrical properties [124]. More recently, 1075°C was found to be better than 1150°C [55]. In this last work, the InN samples were of higher thickness and improved quality, but for a final conclusion, temperatures lower than 1075°C should be investigated again.

This chapter is then divided into two parts: the first part will deal with the study of sapphire nitridation with ammonia using in-situ SE for different durations and at different temperatures in order to understand the chemistry and the dynamics of the process (paragraphs 1 and 2). The results will be discussed in terms of tanΨ and cosΔ since this representation is convenient to identify surface effects during sapphire nitridation. The second part of this chapter will deal with electronic, morphologic and crystallographic properties of a set of InN layers grown after different nitridation procedures respectively by Hall, Total Integrated Scattering (TIS, an optical technique which measures an effective surface roughness [125]) and AFM, X-Ray diffraction. This study will help to identify the optimal nitridation procedure.

6.1 Nitridation at 1050°C

All experiments in this chapter were done with a reactor pressure of 100 mbar. In this section, temperature was kept at 1050°C, while the flows were 1 L/min ammonia and 3 L/min of Nitrogen carrier gas, resulting in an ammonia partial pressure of 25 mbar.

The nitridation of sapphire was first monitored in-situ by recording the ellipsometric parameters tanΨ and cosΔ at a fixed photon energy of 5.0 eV. When ammonia

is introduced in the reactor at 1050°C (t=0 s in Fig. 6.1) both parameters change instantaneously.

The value of tanΨ in Fig. 6.1 decreases steadily during the initial 45 s of nitridation and remains constant for the rest of the experiment. The value of cosΔ decreases following a slow exponential decay. Effects of physisorption of ammonia on the sapphire surface were ruled out because the measured tanΨ and cosΔ remain unchanged after ammonia flow is stopped, demonstrating that an irreversible process (chemi-sorption) is occurring. The spectral dependence of the ellipsometric parameters is given in Fig. 6.2 for different stages of sapphire nitridation. In this experiment ellipsometric spectra were recorded between ammonia exposures of different durations. The most prominent changes occur above 4 eV. After the first 60 s of nitridation the tanΨ spec-

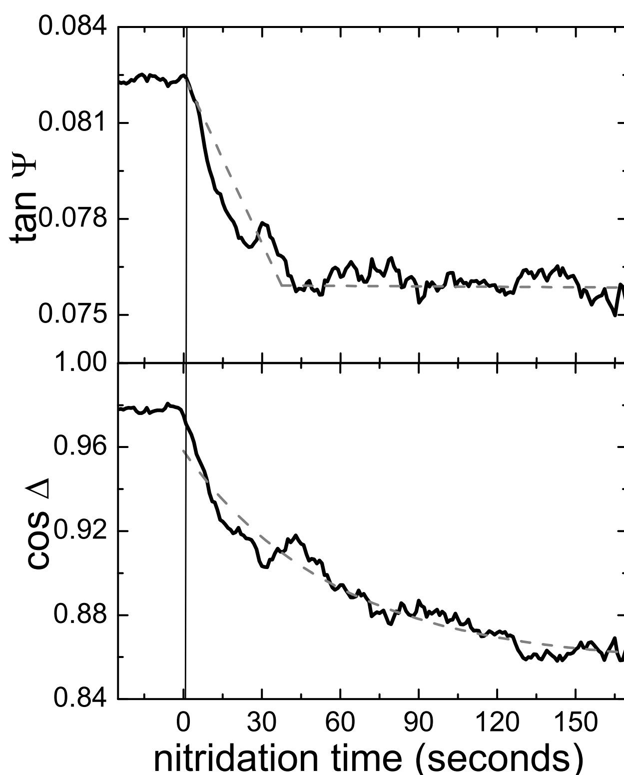

Figure 6.1: *Ellipsometric transient at 5 eV during sapphire nitridation with ammonia, tanΨ (top) and cosΔ (bottom) are shown. Both the signals change strongly when ammonia is introduced in the reactor at 0 s. Grey lines are a guide to the eye in the case of tanΨ, and an exponentioal decay fit in the case of cosΔ.*

tra do not change further, while cosΔ continues to decrease, in accordance with the behavior of the transients recorded at 5 eV (Fig. 6.1). tanΨ is mostly sensitive to the polarising angle of the topmost material and thus to the chemistry of the surface. Thus, the initial fast change is attributed to the exchange of the oxygen atoms of the sapphire surface (on the topmost 1-2 monolayers) with nitrogen. Subsequently, the tanΨ signal remains constant indicating no further changes of the chemistry at the surface.

The exponential decay of cosΔ during further nitridation may either originate from an increase of surface roughness or from a slowly increasing thickness of the

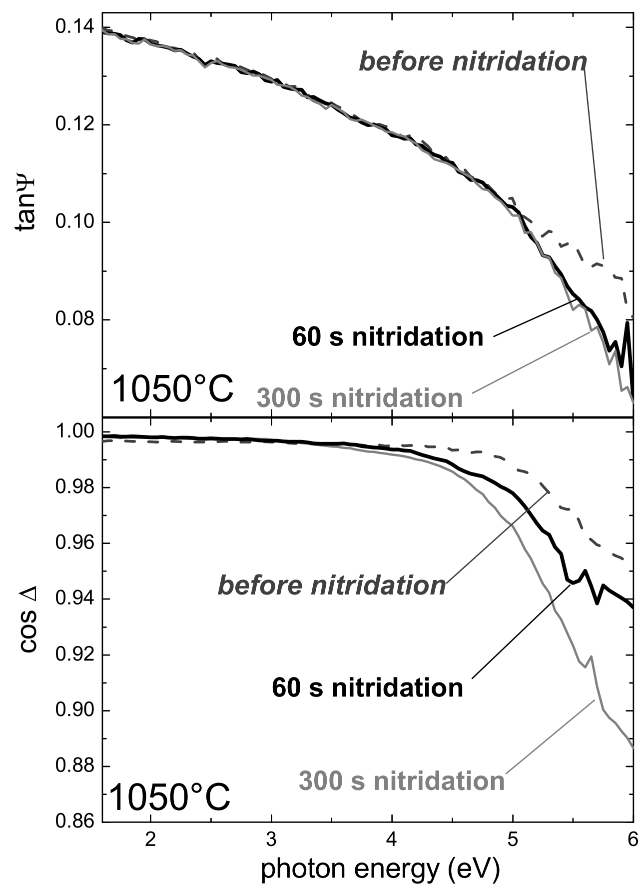

Figure 6.2: *Ellipsometric spectra after different sapphire nitridation times, tanΨ and cosΔ are shown. tanΨ is nearly constant after the first minute, while cosΔ decreases with increasing nitridation time.*

nitridated layer. Roughness may rise due to exposure to ammonia and need to be addressed for a careful interpretation of in-situ data.

Therefore, surface morphology was measured by ex-situ atomic force microscopy (AFM) on nitridated sapphire layers. Figure 6.3 shows the sapphire morphology after 5 min (a) and 10 min (b) nitridation. The corresponding calculated rms roughness is 0.13 nm and 0.18 nm. The small increase in roughness agrees well with previously reported values [123] and is too small to influence the ellipsometric measurements.

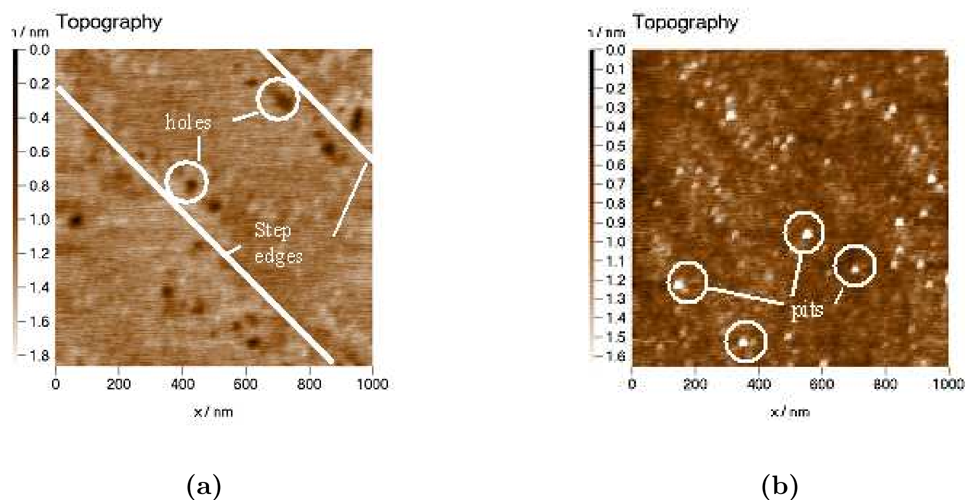

(a) (b)

Figure 6.3: *Typical AFM morphology of sapphire after 300 s (a) and 600 s (b) nitridation. Holes are decorating the step edges in (a), while the steps are not recognizable anymore in (b) and protrusions are formed instead of holes.*

There are extensive ex-situ studies of nitridation of sapphire (see [93] and references therein) and we will shortly summarize them here. It was strongly debated in literature whether ammonia produces an AlN layer or a defective, amorphous AlO_xN_y layer on top of sapphire. Several investigations support one or the other possibility. The reasons for these discrepancies were explained in reference [93] in terms of oxidation occurring during transfer of the sapphire samples from the growth reactor to the TEM measurement facility. A relatively unstrained AlN layer with a large density of point defects was observed in transmission electron micrographs, if nitridated sapphire was protected by an amorphous Si_xN_y cap during transfer of the sample from the MOVPE to the TEM chamber. On the other hand, unprotected samples showed an amorphous AlO_xN_y layer on the sapphire surface. The exposure of the unprotected AlN/sapphire layer to air was obviously leading to the oxidation of the very thin AlN layer and to the formation of amorphous material.

The exact mechanism of the reaction is also still unclear, but in this case it is generally accepted to assume an exchange reaction of oxygen atoms in αAl_2O_3 with nitrogen atoms from NH_3 molecules. Based on this result, in the following we assume

that ammonia produces crystalline AlN on the sapphire surface [93] to interpret the ellipsometric data.

The well-known optical properties of unstrained, perfect AlN are used in first appproximation to simulate the nitridated layer [126]. The dispersion of sapphire was approximated using a Sellmeyer model [127] for transparent layers. The dispersions were recalculated for 1050°C with a method described in detail in reference [30].

The calculated effective dielectric function resulted from a 3-layer-stack, which consisted of (1) sapphire substrate, (2) AlN, and (3) vacuum. The fitting parameter for the model calculation was the AlN thickness. Calculations of tanΨ, cosΔ are shown in Fig. 6.4. The spectra show the best fits of the AlN thickness to the measured spectra in Fig. 6.2. The comparison is very satisfying for tanΨ, while cosΔ suffers from differences between the sapphire database and the measured cosΔ of bare sapphire (Fig. 6.2 (a), bottom). The latter shows in fact a small dip starting at 5.4 eV. This feature persists also after thermal cleaning at 1050°C in hydrogen ambient. In

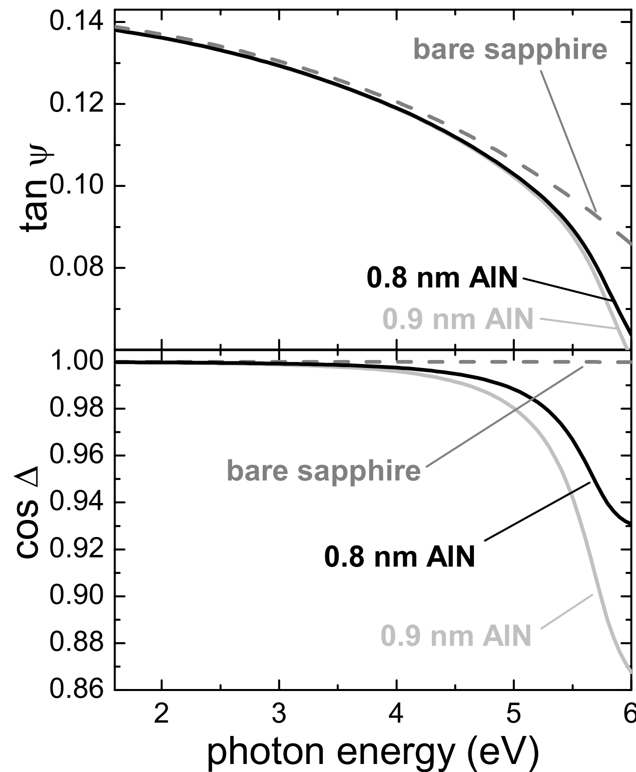

Figure 6.4: *3-layers model calculation of tanΨ and cosΔ after the best fit of the AlN thickness to the measurements in Fig. 6.2*

contrast, cosΔ of sapphire in the reference data remains constant at 1.0 eV up to 6 eV. This feature might originate from impurities in the substrates, or, alternatively, from the surface termination (reconstruction), where presumably hydrogen plays a role.

The result of the fits of the AlN layer thickness to sapphire spectra at different nitridation time is reported in Fig. 6.5, left axis. The thickness increases quickly during the first 60 s, reaching ∼0.8 nm. The subsequent AlN growth rate is less than 0.1 nm/min. The right axis of Fig. 6.5 shows the intensity of emission from the Nitrogen-1s core level by X-ray photoelectron spectroscopy (XPS) from reference [128]. The intensity data are plotted versus nitridation times in MOVPE. Their nitridation parameters were comparable with this work, and they interpreted the peak amplitude as a measurement of nitrogen incorporation into the layer. The comparison in Fig. 6.5 shows good agreement between in-situ (this work) and ex-situ results (reference [128]).

Concluding, the fast (30s) change of the tanΨ signal in Fig. 6.1 is due to modification of the surface chemistry involving (in terms of calculated thickness) the first 1-2 monolayers. It is convenient to address this as a first step of the nitridation process: the *fast step*, or *surface reaction step*. In fact, sapphire chemistry is not further modified afterwards. The reaction of sapphire into AlN after the surface reaction step is the origin of the exponential decay in cosΔ, since the roughness increase is negligible with respect to the increase of the AlN layer thickness (∼0.1 nm/60 s of AlN growth rate against ∼0.01 nm/60s of roughness increase rate). This is addressed as second step of the process: the *slow step* (∼10 times smaller than the surface reaction step), or the *growth and roughening step*.

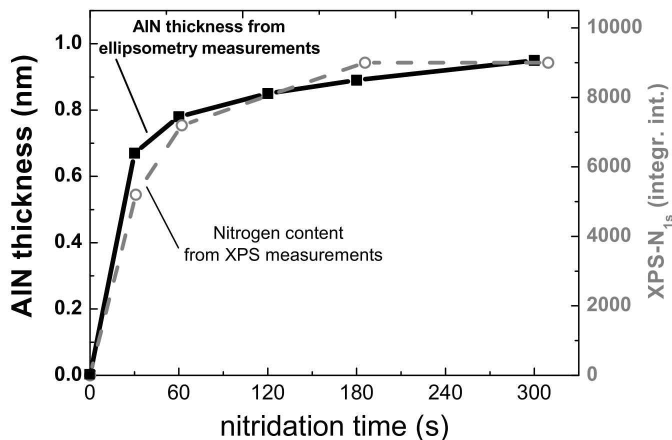

Figure 6.5: *Comparison between ellipsometric in-situ results (AlN thickness, left axis, this work) and ex-situ results (nitrogen content from XPS, right axis, ref. [128]). There is very good correlation between the two results obtained with two different MOVPE set-ups and two different investigation techniques.*

6.2 Nitridation kinetics

The nitridation process has been studied in the previous paragraph by assuming the formation of an AlN layer on top of sapphire due to exchange reaction of the oxygen atoms originally belonging to the sapphire lattice with the nitrogen atoms supplied by activated ammmonia molecules. The process is here further investigated by studying the growth kinetics. The growth rate of the AlN layer at 1050°C with 25mbar ammonia was determined in the previous section. Its dependence of the ammonia pressure and of temperature can indicate the process limiting the reaction rate. Thus, this section presents the results of studies of ammonia partial pressure and temperature during sapphire nitridation with ammonia.

6.2.1 Variations of ammonia partial pressure

Sapphire samples were heated at 1050°C in the MOVPE reactor and then nitridated with ammonia at different fluxes. All the other parameters were kept the same as described in the previous paragraph. Ammonia fluxes were 1 L/min (in a total flux of 4 L/min, ammonia partial pressure was 25 mbar) in the first nitridation experiment and at 0.1 L/min (in a total flux of 3 L/min, ammonia partial pressure was 3 mbar) in the second experiment. In Fig. 6.6 the exponential decay fits to two cosΔ transients at 5.2 eV for the two different ammonia fluxes are basically identical. Since the change in the cosΔ signal is dependent of the AlN growth rate (see Fig. 6.4), we can conclude that the growth rate is the same for both nitridation experiments. The inset in Fig. 6.6 shows also the corresponding tanΨ transients. The changes in tanΨ for the two different fluxes are also very similar, indicating that the reaction on the surface is independent of the ammonia supersaturation too.

In Fig. 6.7 the two cosΔ in-situ spectra measured at 1050°C belong to two sapphire samples after 15 minutes of nitridation with, respectively, 1 L/min (25 mbar ammonia partial pressure) and 3 L/min of ammonia flux (in a total flux of 4 L/min, ammonia partial pressure was 75 mbar). The cosΔ spectra of the layer nitridated with high ammonia flux seem to be lower in the energy range above 4.5 eV. Anyway, the spectral differences are small with respect to the experimental noise and accuracy. Again, also the tanΨ transient shows that the chemistry of the surface changes with a similar rate by using the two different ammonia fluxes and the surface top oxygen layers are exchanged with nitrogen in $\sim$45s.

In conclusion, the reaction rate dependence of the ammonia partial pressure at 1050°C is negligible. This indicates that the limiting step in the AlN growth is not the activation of ammonia molecules but rather a diffusion process involving either Nitrogen diffusion into the sapphire bulk or, alternatively, a bottom-up diffusion of Aluminium atoms or of Oxygen atoms. The measurement of the temperature dependence of the growth rate might indicate, through the determination of an activation energy, which process is actually limiting the growth rate. This is discussed in the following section.

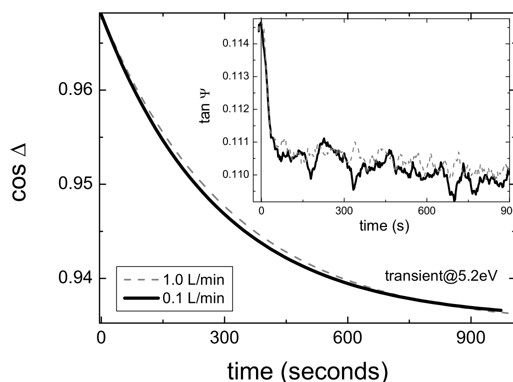

Figure 6.6: *Exponential decay fits to the cosΔ transients at a photon energy of 5.2 eV during sapphire nitridation using 1.0 L/min ammonia (dashed) and 0.1 L/ammonia (full). The influence of different partial pressure is negligible. tanΨ is shown in the inset. It indicates that the surface reaction dynamics is also independent of the ammonia partial pressure.*

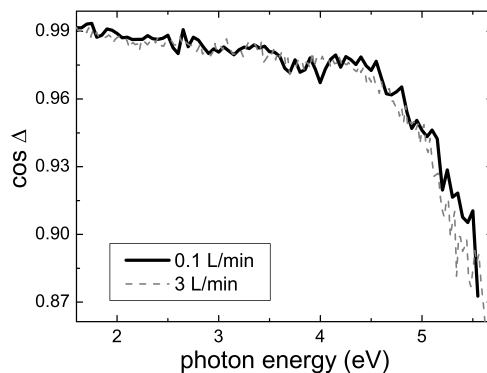

Figure 6.7: *Ellipsometric spectra at 1050°C of cosΔ for two sapphire layers nitridated with 0.1 L/min (dashed, grey) and 3L/min (solid, black) ammonia fluxes, respectively. 30 times different partial pressure of ammonia does not result in a significant difference in thickness of the grown AlN layer. It can then be concluded that at 1050°C the nitridation process is limited by diffusion and not by activation of ammonia molecules.*

6.2.2 Variations of temperature

A set of sapphire samples were heated in the MOVPE reactor at different temperatures and then nitridated with ammonia. Nitridation time was 15 minutes. The experiment was repeated at five different temperatures from 975°C to 1075°C. Transients were measured at 5 eV. In Fig. 6.8 tanΨ transient of the highest and of the lowest temperature shows that there is no significant difference in the nitridation rate of the surface. This demonstrates that the reaction rate of the surface is, in the investigated temperature range, independent of the nitridation temperature. On the other hand, the inset in Fig. 6.8 shows that the change in cosΔ has a strong temperature dependence. This is discussed more in detail in Fig. 6.9, showing the exponential decay fit for the cosΔ signal measured during sapphire nitridation at different temperatures. The dependence on the temperature is obvious: the faster the change in cosΔ, the higher is the growth rate of AlN.

The growth rates are shown in Fig. 6.10. The growth rate at 1050°C is known from model calculations and the datapoints are the same as in Fig. 6.5. For the other temperatures the datapoints have been extrapolated by the comparison of the respective cosΔ value with the cosΔ value for nitridation at 1050°C in Fig. 6.9. The

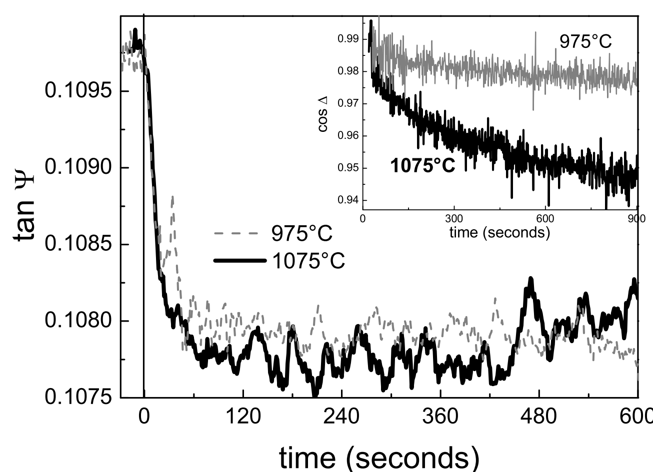

Figure 6.8: *Ellipsometric transients at 5 eV measured during sapphire nitridation at 975°C and 1075°C. tanΨ is not significantly different, which means that for these two temperatures the dynamics of the surface reaction step is not dependent on the temperature and that the chemistry of the surface changes always in ∼45 s. On the other hand, in the inset, cosΔ demonstrates a very strong difference in the growth rate of the AlN for the two nitridation temperatures, which means that the growth rate of AlN is influenced by temperature.*

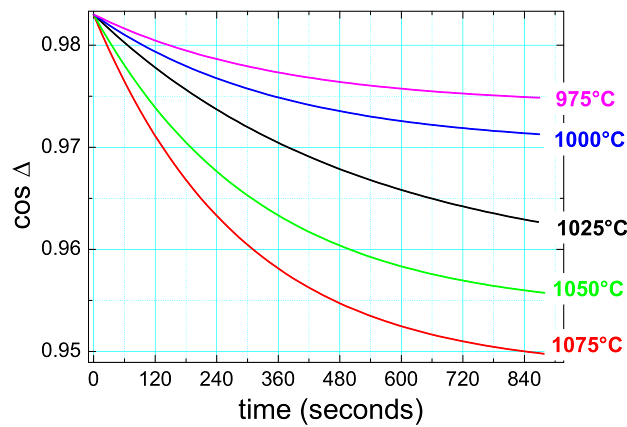

Figure 6.9: *Exponential decay fits to cosΔ transients measured during nitridation of sapphire at different temperatures. Increasing temperature leads to larger changes in cosΔ, which in turn means faster AlN growth rates.*

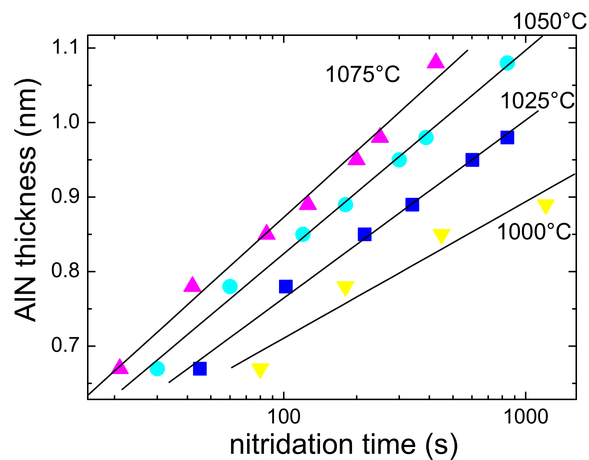

Figure 6.10: *Extrapolation of the AlN growth rates from Fig. 6.9 by comparison with the fit of the growth rate at 1050°C, which was obtained by fitting of model calculations. For all the temperatures the thickness of AlN increases logarithmically.*

full lines in Fig. 6.10 are linear fits to the extrapolated datapoints. For 975°C the growth rate was too slow to allow a sufficient comparison with the thickness values

actually fitted with model calculations to the measurements at 1050°C, therefore the minimum temperature shown in Fig. 6.10 is 1000°C. The linar fit in a logarithmic x-axis scale implies a first order kinetic.

The kinetic constant k can be defined as the growth rate $\frac{d(D_{AlN})}{dt}$:

$$k = \frac{d(D_{AlN})}{dt} = \frac{d[\alpha + \beta ln(t)]}{dt} = \frac{\beta}{t} \tag{6.1}$$

where t is the time and α and β are parameters of the linear fits to the calculated datapoints in Fig. 6.10. The calculated k values are presented in an Arrhenius plot in Fig. 6.11. Arrhenius equation can be written as:

$$ln(k) = ln(A_0) + \left(\frac{E_a}{K}\right)\frac{1}{T} \tag{6.2}$$

where A_0 is the so called *pre-exponential factor*, E_a is the activation energy, K is the gas constant and T the temperature in Kelvin. The time t at the denominator in equation 6.1 was chosen as a constant and it is not influencing the term containing the activation energy E_a in equation 6.2. The resulting activation energy is 0.9 eV.

A polynomial function with a quadratic term has better agreement to the datapoints. In this case the non-linear dependence suggests that kinetics is more complicated than a simple first order or that, perhaps, other processes are involved. One possible process has already been mentioned in the previous subsection: while it is proved that the ammonia supersaturation does not play a role at 1050°C, it must be proved that this is true also for lower temperatures. The lower point in Fig. 6.11

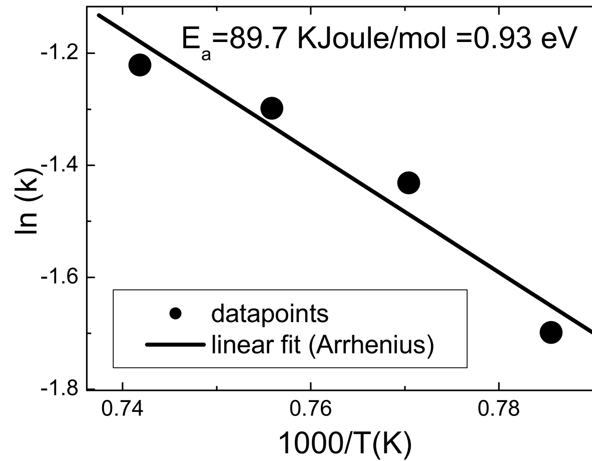

Figure 6.11: *Kinetic constant* k *calculated from the AlN growth rates versus reciprocal temperature. The activation energy resulting from a linear fit (full line) reads 0.93 eV for AlN formation from sapphire bulk.*

could in fact also be affected by a less effective activation of ammonia. As a result, it is interesting that the activation energy for the diffusion process would be lower. In this case, a further experiment with different ammonia fluxes at 1000°C should solve the issue.

An additional error is the etching of the AlN layer due to the exposure to ammonia at such high temperatures. Ellipsometry might in fact only be measuring an "effective" growth rate, that is the growth rate due to the exchange reaction minus the etching rate. Ammonia is in fact highly reactive not only as Nitrogen precursor, but also provides active Hydrogen that might reduce Aluminum and cause the decomposition of the layer. However, some preliminary experiments where hydrogen was used as gas carrier at 1050°C show that $\cos\Delta$ signal is not different from experiments where the carrier gas is nitrogen.

6.3 Sapphire nitridation for InN growth

Sapphire nitridation for GaN growth is well established. However, for InN growth only few results have been reported in the literature and further investigations are necessary. Therefore, we have grown a set of InN layers on sapphire after different nitridation procedures and preliminar ex-situ X-ray diffraction assessed the quality of the InN layers. Nitridation was performed with ammonia, varying conditions like carrier gas (N_2 or H_2), nitridation temperature (1000°C and 1050°C) and nitridation time (from 30 s to 900 s). Subsequently, InN layers were grown on top with a thickness of 350 nm following always the same growth procedure (see chapter 7 for details on the growth procedure of InN).

The broadening of the X-Ray diffraction peaks is related to defects in the crystal. Therefore, Fig. 6.12 shows the full-width at half-maximum (FWHM) of the (0002) reflection of InN layers in the ω-scans (top) and in the ω-2θ-scans (bottom). The narrowest FWHM and therefore the optimal nitridation conditions are found in Fig. 6.12 for nitrogen as carrier gas, nitridation times between 30 s and 60 s at 1050°C and around 300 s at 1000°C. Also, nitridation at 1050°C yields better InN samples than nitridation at 1000°C. In summary, the optimal sapphire nitridation procedure for InN growth is obtained for a nitridation temperature of 1050°C using nitrogen as carrier gas.

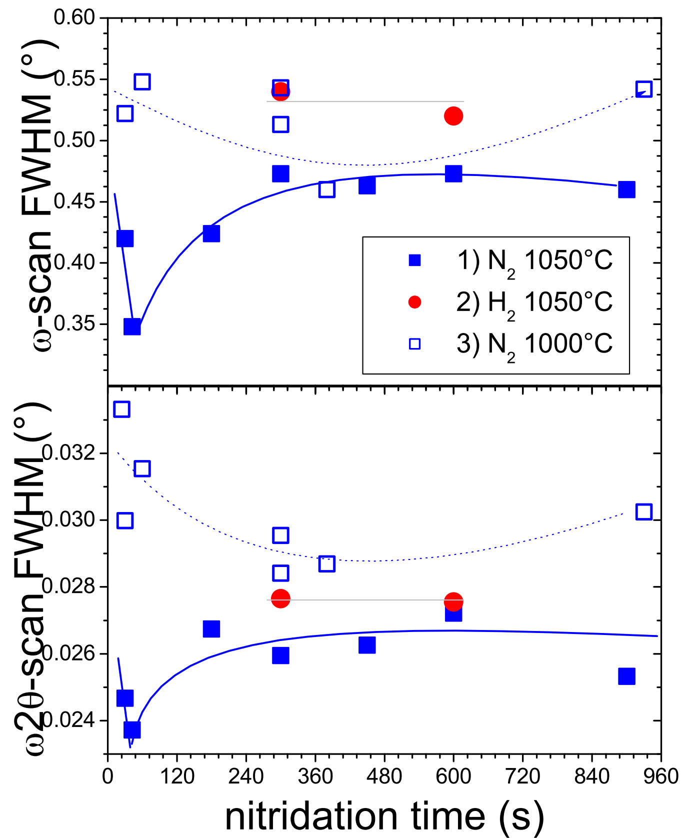

Figure 6.12: *Preliminary X-ray study of InN/sapphire with respect to the nitridation procedure. FWHM of X-ray diffraction peaks along the (00.2) reflection in the ω-scan (top) and the ω-2θ-scan (below) of InN films grown after different nitridation procedures. Hydrogen (circles) and nitrogen (squares) were used as carriers during nitridation, nitrogen at two temperatures: 1000°C (hollow squares) and 1050°C (full squares). Best InN layers are grown with nitrogen as carrier at 1050°C.*

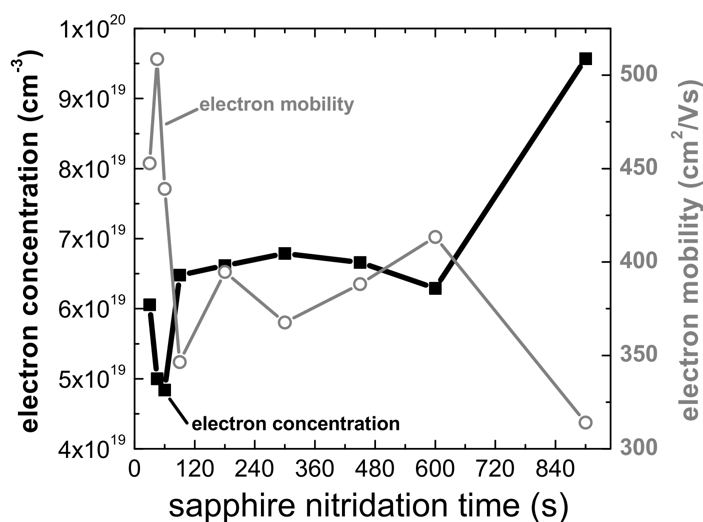

Figure 6.13: *Hall measurements of carrier concentration (left axis, full squares) and electron mobility (right axis, hollow circles) for 350 nm thick InN samples grown on sapphire after different sapphire nitridation times (x axis). The lower carrier concentration is measured on InN films after 45 s up to 60 s of sapphire nitridation. The highest mobility is obtained for a nitridation time of 45 s.*

To further optimize sapphire nitridation the mobilities and carrier concentration in Hall and asymmetric XRD was measured on InN layers grown after nitridation of sapphire at 1050°C for different nitridation durations.

The effects of nitridation on the electrical properties of the InN layers are shown by Hall measurements in Fig. 6.13. The measurements showed a n-type conductivity for all the samples. The lowest carrier concentration is obtained for short nitridation duration between 30 s and 60 s, although this value is still very high, $5 \cdot 10^{19}\,\mathrm{cm}^{-3}$. Prolonged nitridation leads to a strong increase, indicating a deterioration of the layers. The maximum mobility is accordingly also found for short nitridation times, the highest value ($500\,\mathrm{cm}^2/\mathrm{Vs}$) is obtained for 45 s.

To correlate the electrical data to structural properties of the InN layers, XRD ω-scans were measured for the studied samples. The symmetrical (00.2) reflection is sensitive to zero-dimensional defects, a-type dislocations[1], mixed (c+a) dislocations and stacking faults [129]. As shown in Fig. 6.14, left axis, the narrowest FWHM of the rocking curves is obtained for nitridation times between 30 s and 180 s. This result suggest that the optimum electrical properties originate from optimum structural properties of the InN layers.

On the other hand, symmetric reflections are insensitive to edge threading dislocations, which in turn affect e.g. the asymmetric (10.2) reflections. These are hence complementary to the (00.2) reflection. Fig. 6.14, right, shows that narrowest FWHM of the (10.2) reflection are found for nitridation times exceeding 3 min. This last result is anticorrelated with the electrical characterisation.

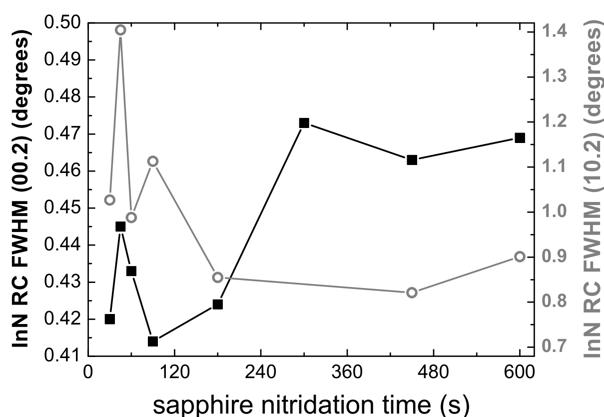

Figure 6.14: *On the left axis is FWHM of the X-ray ω-scan (rocking curve, RC) along the (0002) InN direction for 350 nm thick InN samples grown on sapphire after different sapphire nitridation times. The narrowest diffraction curves are obtained after less than 180 s of sapphire nitridation. On the right axis is FWHM of the ω-scan (rocking curve, RC) along the (10.2) reflection. The narrowest diffraction curves are obtained for sapphire nitridation longer than 180 s.*

[1]Dislocations are 2-dimensional (or linear) crystallographic defects which can also affect other material properties (electric, optical, etc.). Dislocations can be described by the Burgers vector and by the dislocation line. The dislocation line is the line where the defect and the resulting lattice distorsion can be found. The Burgers vector is the direction and the entity of atoms displacement. Dislocations are generally grouped into two types, edge and screw type dislocation, according to the angle of the Burgers vector with respect to the dislocation line. Mixed, partial and multiple dislocation can also be found. In nitrides, the dislocations are often grouped according to the direction of the Burgers vector with respect to the crystallographic directions [129]. The Burgers vector of c-type dislocations is parallel to the c-direction, i.e. the (0001) direction. An a-type dislocation has the Burgers vector perpendicular to the c-direction. The Burgers vector of (c+a) dislocation is neither parallel, nor perpendicular to the c-direction.

The overall X-ray characterisation picture suggests that a short sapphire nitridation time (below 180 s, in good agreement with Hall mobility) results in a InN layer with generally improved (0001) mosaicity. In terms of microstructure, a-type and mixed (c+a) dislocations decrease for a short sapphire nitridation time. On the other hand, above 180 s of sapphire nitridation c-type dislocations decrease in number. To address the dynamic with which dislocations are generated from differently nitridated sapphire, further investigations are required. In general, since it is still unknown which defects are electrically active in InN, it can be concluded that the X-ray crystallographic characterisation is not in disagreement with the electrical Hall data.

Finally, the morphology of the as-grown InN films must be characterized. For this purpose, we used Total Integrated Scattering (TIS) [125]. In Fig. 6.15 we show the effective rms roughness calculated from the total intensity of the scattered light. The smoother surfaces belong to InN films where sapphire was nitrated between 45 s and 90 s correlating with the carrier concentration and with the symmetric (00.2) reflection. As mentioned before, TIS rms cannot be compared with AFM rms. The smoothest sample has 1.5 nm rms roughness as determined on 1 μm^2 AFM images.

Since only very little data on InN properties exist, we compare our results with the well-studied GaN/sapphire. In the GaN system a short nitridation time of 60 s (for nitridation conditions similar to ours) produced better layer quality, as measured by photoluminescence, Hall and XRD [120]. These results correlated well with a narrow FWHM of the asymmetric (10.2) X-ray reflection. The symmetric (00.2) X-

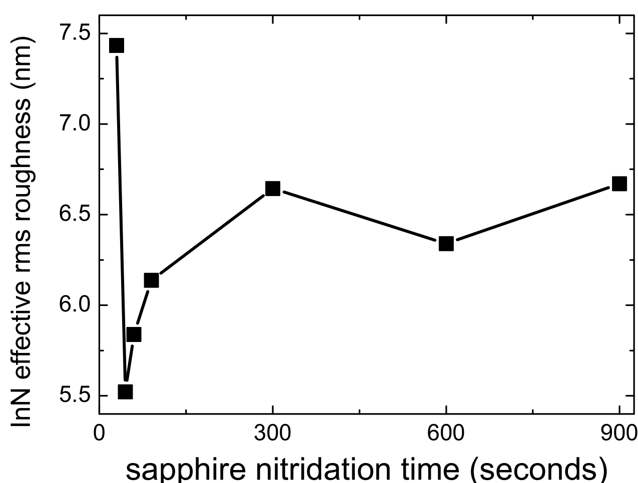

Figure 6.15: *Effective roughness for 350 nm thick InN samples grown on sapphire after different sapphire nitridation times. The rms is calculated from TIS. The smoothest layers are grown after 45 s of sapphire nitridation.*

ray reflection, however, was anticorrelated and narrower for samples with more than 400 s sapphire nitridation. Since in GaN edge threading dislocations provide a charge carrier recombination channel, the asymmetric (10.2) reflection was considered more indicative for high layer quality in reference [120]. Another study on the sapphire nitridation effect on GaN properties also measured best electronic properties for short durations between 30 s to 60 s under similar conditions [121]. In this case, however, the symmetric (00.2) reflection was correlating with electronic and morphological data, while the asymmetric (10.2) reflection was not. This indicates that different defects may dominate the electronic properties of GaN layers on sapphire. The important common conclusion of references [120, 121] is: best electronic properties of GaN layers are obtained for short nitration times of 30 s and 60 s.

Similar to these findings for GaN, in this study best InN electric properties are found for ∼45 s of sapphire nitridation. After this time, a complete AlN thin layer covers the whole sapphire surface and the surface chemistry does not change anymore. Then the morphology degrades with increasing nitridation time (pits and holes are formed on sapphire, see Fig. 6.3), influencing the quality of the InN film grown on top. Excessive nitridation of the sapphire layer may also favour diffusion of oxygen atoms from sapphire into the nitride layer [130], through channels such as the holes and pits visible in Fig. 6.3.

The very good correlation between morphologic and electric properties might be due to a strong electron accumulation layer in InN [64]. This seems to be an intrinsic InN property [62], though it is clear that surface contamination is enhancing the accumulation [67]. For the relatively thin InN layers the number of electrons on the surface might increase with increasing roughness, influencing the total number of electrons (surface and bulk) measured by Hall. To address this numerically further knowledge on InN is necessary. If the correlation between roughness and carriers is confirmed, a flat surface morphology would become even more important for InN layers.

6.4 Chapter Summary

Sapphire nitridation with ammonia at 1050°C was studied by in-situ ellipsometry. A fast surface modification step occurred within the first 45 s (fast step). This is followed by a slow bulk transformation of sapphire into AlN and a slow surface roughening (slow step). Ntridation has a kinetic of the first order and an activation energy of 0.9 eV.

A set of InN films were then grown with the same procedure on sapphire substrates nitrated for different times. Electrical properties determined by Hall measurements, crystal properties determined by symmetric X-ray diffraction and surface morphology studied with angle resolved scattering indicate best quality of the InN films when the nitridation process of sapphire is limited to its *fast step*. A close comparison with older results on the GaN/sapphire system where the optimal nitridation time was found to be below 60 s is very similar to the InN/sapphire system studied in this work. Also, the characterisation along the (10.2) asymmetric X-ray diffraction shows narrower rocking curves for a minimum nitridation time of 180 s, in contradiction with all

the other results. Assuming that the electronic properties are the relevant condition for the identification of the best InN films, we conclude that only the outermost sapphire layers need to be nitrated to achieve optimum quality of InN films. This is achieved within 60 s of nitridation with 25 mbar ammonia partial pressure at 1050°C. The contribution of SE to the optimisation of sapphire nitridation for InN growth now becomes clear: the distinct step-change of the ellipsometric parameter $\tan\Psi$ (Fig. 6.1, top) between 5 eV and 6 eV is a valuable tool to identify the end of the surface transformation. This ellipsometric analysis would lead to optimal nitridation for GaN growth as well.

7. Nucleation and growth

This chapter deals with details of the MOVPE growth of InN with respect to the nucleation (i.e. hetero-epitaxial growth) and homo-epitaxial growth. The focus will be on the growth strategy, on the effects of different growth parameters on the growth rate and on the crystal quality of the InN epitaxial layers.

7.1 Nucleation

The substrate preparation was the focus of the previous chapter. In this chapter it will be discussed what happens when the precursors are injected into the reactor. As already mentioned, the precursors used were TMIn to supply atomic Indium and ammonia to supply atomic Nitrogen for the growth and the carrier gas was nitrogen.

When material A is grown on material B, nucleation represents the stage of hetero-epitaxial growth, i.e. epitaxy on a foreign substrate. Due to the large lattice mismatch between InN and sapphire (or, similarly, to the AlN layer formed during nitridation), relaxation of the InN growing layer is expected to occur at the first monolayers. Relaxation implies 3-dimensional growth mode, very common in heteroepitaxy.

Model calculations are used to discuss ellipsometry measurements during growth of InN. For this, the dielectric function of InN at 5 eV was extrapolated from measurements on thick InN layers (∼400 nm) with good crystalline quality and good surface morphology.

The effects of different initial growth conditions were studied: ammonia and TMIn have been introduced into the reactor at the same time, or one of the two with a certain time delay. Figure 7.1 shows three different nucleation experiments monitored by the ellipsometric parameters tanΨ and cosΔ at a photon energy of 5 eV, angle of incidence of 65.0°. The other MOVPE growth parameters remained fixed to the values discussed in paragraph 6. At the initial nucleation, TMIn was offered either 10 s after ammonia (transient A in 7.1, our standard procedure), at same time with ammonia (transient B) or 2 s before ammonia (transient C).

Nucleation of type (A) (curve A in Fig. 7.1) is done with standard growth parameters (Table 4.1) and can be efficiently modelled using a simple 3-phase model: vacuum, InN, sapphire. This model calculates an *effective thickness* of the InN layer because of probable 3-dimensional growth mode.

The minimum in tanΨ corresponds to an effective InN thickness of 3 nm, and coincides with the change in sign of the 2nd derivative of cosΔ. It is remarkable that the signature of the nucleation of GaN on sapphire is extremely similar to the one of InN, shown in Fig. 7.1 [81]. This is due to the different Brewster angles of sapphire and InN (or GaN), which lie above and below the angle of incidence (65.0°), respectively. Nucleation (B) in Fig. 7.1 shows only a small divergence from (A), while (C) shows a clearly different behavior, due to the strong presence of metallic Indium. In spite

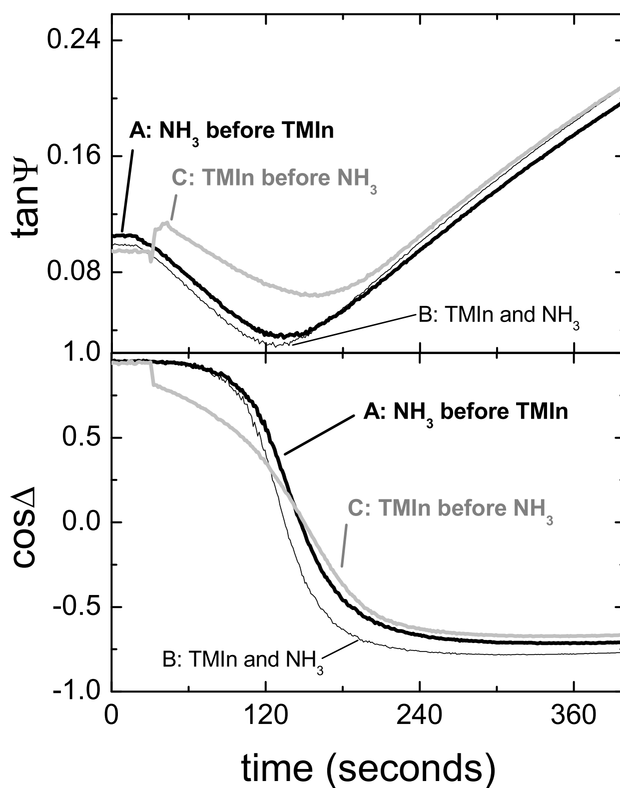

Figure 7.1: *Ellipsometric transients (tanΨ top, cosΔ bottom) at 5 eV photon energy during InN nucleation on sapphire at 520°C. Ammonia is always introduced after 10 s. In transient A (black, thin), TMIn is introduced 10 s after ammonia, in transient B (black, thick) it is introduced together with ammonia, in transient C (grey) it is introduced 2 s before ammonia. The nucleation dynamic of the latter is clearly different from the other two nucleation procedures.*

of the very different nucleation dynamics, the InN layers grown after the different nucleation do not show, surprisingly, remarkable differences (after characterization with X-ray diffraction: ω- and ω-2θ-scans). These different procedures were adopted mainly to find a solution to the layer peeling off but, as mentioned in the previous paragraph, none of these nucleation procedures were successful and partial peeling off of the layer was found in all the $\sim$300 nm thick InN layers.

7.2 Growth rate

In a preliminary study, the growth rate of InN was calculated from spectra of the effective dielectric function during a growth experiment performed at different temperatures, namely, from 800°C down to 350°C [81]. The growth rates have been verified later by further growth experiments performed at constant temperatures monitored by ellipsometry and by simultaneous evaluation of the growth rates through measurement of the InN layer thickness. Cross section SEM images of InN layers were used for this purpose.

It should be noted that since the growth mode is in most cases 3-dimensional, these values for growth rates can be overestimated. Only with 2-dimensional growth is it possible to measure and calculate growth rates in a more reproducible way. This is also the reason why the growth rate has not been studied systematically. The order of magnitude of these growth rates is anyway very important in order to analyze the growth process.

The results for low supersaturation (V/III=$6 \cdot 10^4$, ammonia flow=1 L/min) given in Fig. 7.2 are given between 375°C and 650°C (full circles). They show a typical behavior of the growth rate from the temperature [9, 18] where three main regions are identifiable. In the first region (grey, left), up to 400°C the growth rate increases with temperature, meaning that it is limited by the decomposition of the precursors (TMIn is fully decomposed at 400°C: kinetically limited regime). In the second region (center), between 400°C and 550°C, the growth rate is constant, in the typical behavior of a transport limited regime. In the third region (grey, right), above 550°C, the growth rate decreases with increasing temperature, meaning that the InN layer decomposes (desorption limited regime). The reader should note that the transport limited growth regime, which is most suited for MOVPE [18], lies in a narrow window of 150°C and at very low temperatures for typical nitride growth. In this region, the growth rates are still very low due to the small amount of ammonia available from decomposition. Furthermore, the 3-dimensional growth overestimates the growth rate in the kinetic and in the desorption limited regions, saturating to the growth rate of the transport limited region. Thus, the transport limited region might actually seem larger than in reality.

Figure 7.2 compares also the effects of different growth parameters on the growth rate in the close temperature range between 500°C and 550°C. By increasing the TMIn flux (see the following symbols in 7.2: full circles, triangles, hollow circle) the growth rate increases. This indicates a Indium limited growth rate. By increasing the ammonia flow, (hollow circle, squares) the growth rates *decreases*, which means that ammonia is actually also having an etching effect. By increasing the supersaturation,

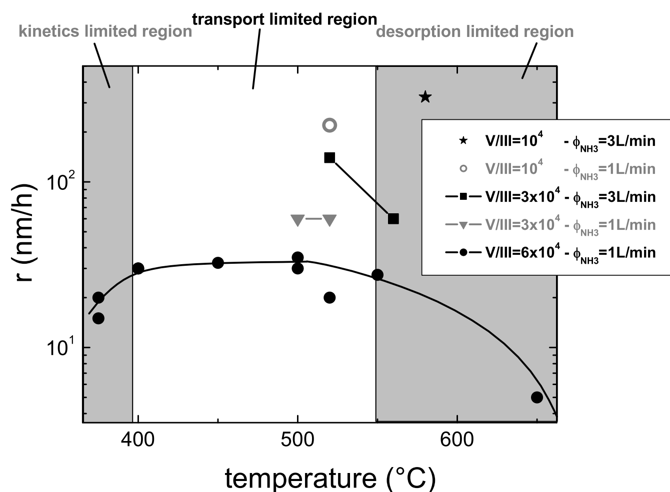

Figure 7.2: *Growth rate of InN evaluated by ellipsometry and by cross sections SEM images. The 3 regimes of growth for V/III ratio of $6 \cdot 10^5$ (full circles) are as follow: kinetically limited growth rate below 400°C, transport limited growth rate from 400°C up to 550°C, thermodynamically limited growth rate above 550°C. Different symbols refer to different growth parameters, given in the legend.*

i.e by keeping the same V/III ratio and by increasing the flow of both precursors (triangles, squares), the growth rate increases.

Finally, the growth at 580°C (Fig. 7.2, star) is performed with the highest supersaturation and the lowest V/III ratio. It also has the highest temperature, the growth rate being in the desorption limited range. The crystal quality of the layers grown with these growth parameters is much higher than for any other. The properties of these layers will be discussed in detail in the next sections.

7.3 Effects of growth temperature on crystal textures

Texture analysis of the InN/sapphire layers can lead to improvements of the growth procedure. A polar X-ray diffraction scan was obtained through a rotation by the normal of the Bragg planes referring to the asymmetric (10.2) reflection at fixed angles. Such a scan shows the epitaxial orientation of the nitride planes with respect to the plane of the sapphire substrate. As previously discussed in Chapter 3 and in Chapter 6, after nitridation an angle of 30° between the planes of InN and sapphire is expected, and has been previously observed [76, 87]. Fig. 7.3 shows the (10.2) polar scan for two samples grown on sapphire at 500°C (top) and at 520°C (bottom). The

thickness of the samples was 120 nm and they did not show layer peeling off with optical microscope analysis.

Sapphire is trigonal and shows three intense sharp peaks spaced 120° due to the three-fold symmetry. InN shows 6 peaks due to the wurtzite six-fold symmetry, shifted with respect to the sapphire peaks due to in-plane twist of InN with respect to sapphire. In Fig. 7.3, top, each InN peak is split into two peaks and the angle between sapphire peaks and the InN double peaks is of 24° and 26°. This demonstrate a texture twist of the crystal. Slightly higher growth temperature (20° higher) suppresses this phenomenon: the peak splitting is absent and the twist angle of InN to sapphire with respect to the growth (0001) direction is 30°, as expected.

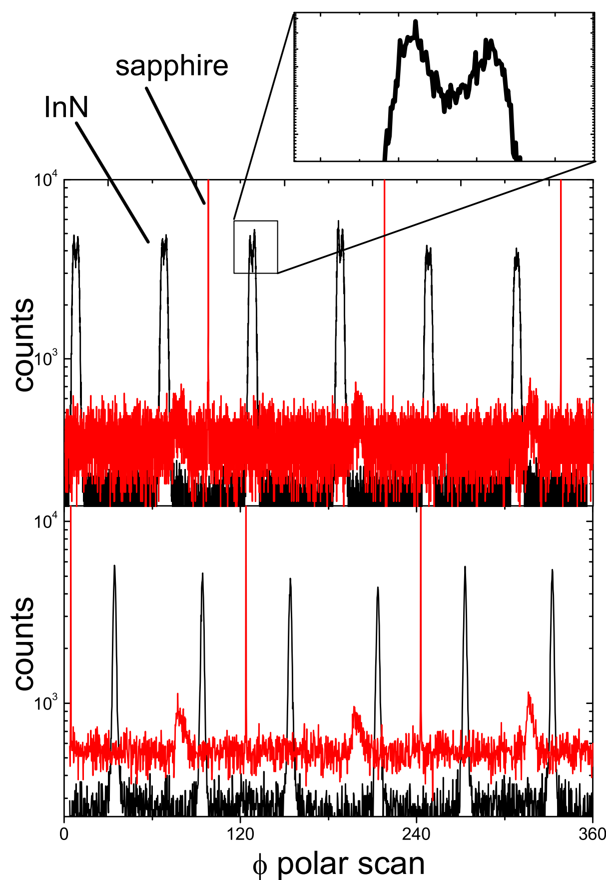

Figure 7.3: *XRD polar scan of the asymmetric (10.2) reflection for 150 nm thick InN layers grown on sapphire at 500°C (top) and at 520°C (bottom). Twist texture is not observed for growth temperatures above 500°C.*

7.4 Optimizing growth

In the last section and also in Chapter 4 it was often found that growth temperatures higher than 520°C result in improved InN quality. It is also worth recalling the work published in literature, summarized in Chapter 3, where most of the growth temperature studies indicate higher temperatures, often above the desorption limit of 550°C, as optimal for the growth of InN layer with best crystalline and electric properties. The principle advantages of higher temperature are evident: activation of the ammonia molecules will be more efficient and the diffusion of the atoms on the surface of the growing material will increase, with a higher chance for them to find (a) their equilibrium position (i.e. their most stable, wurtzitic structure) and (b) to grow layer by layer, giving rise to a 2-dimensional growth mode. The growth rate should be also higher due to improved decomposition of ammonia. Above desorption temperature the growth takes place in the *desorption limited range*, as discussed in a previous section. This limits the growth temperature, since layers grown at temperatures much higher that the desorption temperature for the material (below 540°C for InN, see Chapter 4) tends to roughen. Thus, this section deals with the development of growth strategies that allows to grow InN at temperature above the desorption limit and relies on in-situ spectroscopic ellipsometry to test and adjust the growth parameters in order to control the growth conditions.

In a first approach, after growth of a ~20 nm thick nucleation layer at 530°C, the temperature was increased up to 580°C and then growth was started. InN was exposed to an inert nitrogen ambient during ramping of the temperature. However, the nucleation layer started to decompose even before 550°C because of its high reactivity, originating from its highly defective structure. This eventually resulted in early formation of Indium droplets and a poor quality of the epitaxial layer. A further approach was to avoid the low temperature nucleation layer and to deposit the epitaxial layer directly at high temperature after sapphire nitridation. However, samples grown entirely at 580°C and at 600°C show a very poor quality, with formation of Indium droplets, bad crystallinity and rough surfaces. Decreasing the V/III ratio from 30000 to 10000 did not improve the layer quality. Therefore, growth above 550°C requires a nucleation layer to be deposited at lower temperatures. A possible approach is to ramp the temperature during growth after the deposition of the nucleation layer.

The growth procedure developed in this work is outlined in Fig. 7.4. First, the temperature is ramped up to 580°C with a progressively decreasing slope to avoid roughening of the layer. A further improvement of the growth procedure is a simultaneous slow increase of the TMIn flux. The final V/III was 10^4 (ammonia flux was kept constant at 3 L/min). Between 500°C and 530°C such a low V/III ratio produced highly defective layers covered with In droplets, while at 580°C delivered best quality layers at the highest growth rate of 400 nm/h. These findings agree with recent results from Maleyre et al. [85], who also proposed V/III ratios as low as $5 \cdot 10^3$ to be used for InN growth. Applying the procedure described above, growth above the desorption temperature of InN (550°C, see Chapter 4) could be demonstrated.

The graphs in Fig. 7.5 and Fig. 7.6 show sequences of in-situ SE spectra of the imaginary part of the effective dielectric function $\langle\varepsilon_2\rangle$ at different times during two examples of growth above desorption temperature. In the first example, growth was

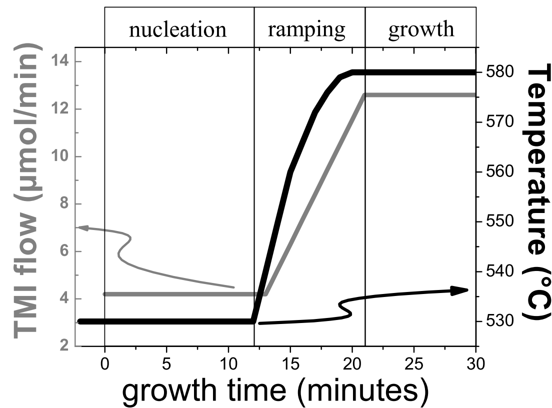

Figure 7.4: *Adjustment of TMIn flux (left axis) and temperature (right axis) during InN growth. After 12 minutes growth at 530 °C (∼15 nm) the temperature is slowly increased to 580 °C. TMIn flux is increased simultaneously while ammonia flux is kept constant at 3 L/min, resulting in a V/III ratio decreased from $3 \cdot 10^4$ to 10^4.*

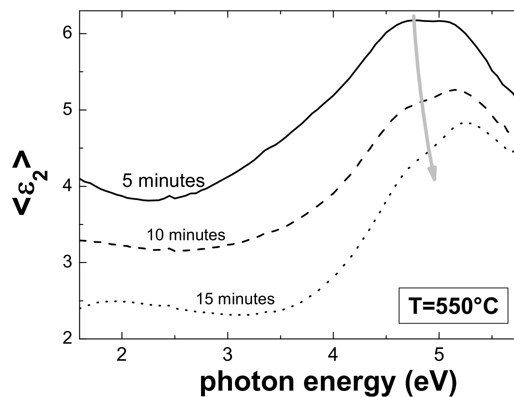

Figure 7.5: *Imaginary part of the effective dielectric function $\langle\varepsilon_2\rangle$ versus photon energy, recorded during growth at 550 °C with high V/III ratio of 40.000, with low supersaturation. The decrease of the amplitude indicates surface roughening. The curved grey arrows indicate the change of amplitude in $\langle\varepsilon_2\rangle$ during growth.*

at 550°C with low supersaturation, resulting in a rough surface and to worse layer quality. In the second example, we used the growth procedure outlined in Fig. 7.4, resulting in improved layer quality.

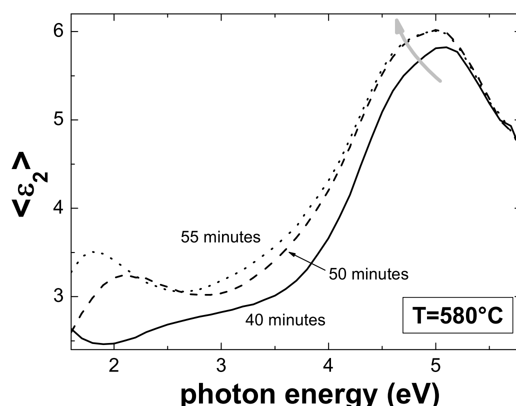

Figure 7.6: *$\langle \varepsilon_2 \rangle$ versus photon energy during growth at 580°C with low V/III ratio of 10.000. At 580°C the first slightly increasing and then finally constant amplitude above 4 eV indicates stable growth conditions: lower V/III ratio allowed growth above the onset of decomposition. The curved grey arrows indicate the change of amplitude in $\langle \varepsilon_2 \rangle$ during growth.*

In the first example of growth at 550°C, the flux of precursors was constant and supersaturation was small (1 L/min ammonia with a high V/III ratio of $4 \cdot 10^4$). These parameters lead to stable growth conditions at temperatures lower than 530°C. The temperature was increased from 500°C to 550°C when the layer thickness was ~60 nm. (Fig. 7.5) shows ellipsometric spectra after 5, 10 and 15 min of growth at 550°C. The decrease of $\langle \varepsilon_2 \rangle$ indicates progressive decrease of the optical density of the layer. This is interpreted in terms of a formation of a rough layer on top. Due to the small supersaturation the growth rate was very small and, most probably, the desorption of the layer led to the roughening of the surface.

In the second growth example we applied the growth procedure outlined in Fig. 7.4. Figure 7.6) shows ellipsometric spectra after 40, 50 and 55 min of growth at 580°C. The interference structures below 4 eV clearly indicate an increase of layer thickness with time, e.g. growth. The amplitude of the layer thickness-related interference structures progressively decreases with increasing thickness, since the penetration depth of the light becomes negligible with respect to layer thickness. Above 4 eV the amplitude does not decrease, as expected for a smooth surface not becoming rough. It can be concluded that the sequence of spectra measured at 580°C shows stable growth conditions.

Further studies on InN layers grown with the improved growth procedure outlined in Fig. 7.4 confirmed their excellent properties. Hall measurements show a reduction of the free electron concentration by a factor of 10 down to the low $10^{19}\,\mathrm{cm}^{-3}$ was obtained. An electron mobility of $500\,\mathrm{cm}^2/(\mathrm{Vs})$ is achieved for samples of 350 nm thickness, almost twice the value of the samples grown at 530°C and lower tempera-

tures and approaching the highest mobility of 800 $cm^2/(Vs)$ reported for InN layers grown by MOVPE [85] (which was measured on layers thicker than the layers grown in this work). This result places these samples among the best MOVPE grown InN samples up to now.

Photoluminescence (PL) was measured on these InN samples (growth procedure of Fig. 7.4) by using an Argon excimer laser with an excitation wavelength at 488 nm. In Fig. 7.7 PL was measured by using a InGaAs detector on two InN/sapphire layers of different thickness. The PL measurements were performed at 20 K. Sample (a) was ~120 nm thick and was grown at 520°C, while sample (b) was ~350 nm thick and was grown with the procedure outlined in this section.

Sample (b) has a much higher intensity and the near-band-edge emission is also shifted towards higher wavelength (lower energies). The actual energy peak maximum of sample b) might also be hidden by the decrease of the sensitivity of the InGaAs detector. Sample (a) also shows a decrease in intensity due to the detector limits at around 1661nm. The difference in energy between the two peaks is then at least 0.86 eV-0.75 eV=0.11 eV. The number of carriers as determined by Hall experiments

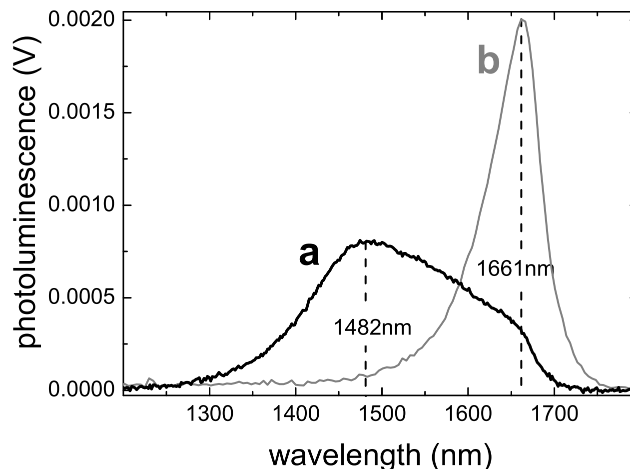

Figure 7.7: *Photoluminescence emission at 20 K after excitation with an Argon excimer laser at 488 nm. An InGaAs detector was used. Measurements of two InN/sapphire samples are shown: sample (a) is ~120 nm thick and was grown at 520°C, sample (b) was ~350 nm thick and was grown with the growth procedure outlined in section 6.4. The detector sensitivity starts to decrease at the maximum of the peak of sample (b), therefore the exact peak position cannot be given. It is however clear that the two layers have a different response, peak (a) is broader and shifted at higher energies.*

was in the case of sample (a) almost a factor of three higher. According to the interpretation of the peak position given by other authors [2], the larger the number of carriers, the larger is the filling of the conduction band. The band-to-band recombination responsible for the photoluminescence peak is then occurring at higher energies due to the Moss-Burstein shift. This result is in line with previous published works on optical properties of InN [2, 131] and shows, also, that layers which are thicker and which are grown at higher temperature (sample b) display improved optical and electronic properties.

7.5 Growth with low ammonia flow

As discussed already in Chapter 4 a low ammonia flow can be used together with a high V/III ratio for successful preparation of InN layers thicker than 300 nm which do not display layer peeling off. This is occurring for example for V/III ratio of $7.5 \cdot 10^3$ and an ammonia flux of 1 L/min, growth temperature 520°C. The growth rate measured in this case is ~220nm/hour, two times higher than when 3 L/min ammonia flux are used. A typical surface of these InN layers was shown in Fig. 4.5. The surface is covered by droplets but, in turn, it displays low roughness, with AFM rms equal to less than 3 nm when calculated on (1×1) μm^2 images and, most remarkably, no peeling off of the layer.

On the other hand, good morphology does not correlate with improved crystal quality. XRD on these samples show a large contribution from polycrystalline InN in the X-Ray reflection at $2\theta \sim 33.4°$. Also, the InN peaks are broader than for other InN samples. The electric properties characterized by Hall show that the layer has a very low mobility, in the range of 130 cm^2/Vs but the number of carriers is surprisingly low: $1.3 \cdot 10^{17}$ cm^{-3}, the lowest ever measured on MOVPE samples and one of the lowest ever measured on InN layers. InN layers with similar mobilities display, typically, carrier concentrations higher than 10^{20} cm^{-3}. The reasons for this apparent incongruence is not yet clear. It is possible that either the grain boundaries are strongly decreasing the electron mobility or that an equally large number of traps due to defects is present in these layers, which is strongly decreasing the number of the free electrons.

These layers grown at 520°C with low V/III ratio do not show a PL peak when measured with an InAs detector, which leads to the conclusion that the near-band-edge recombination is very weak, comparable with other layers with low mobility. The reason for the low carrier concentration is not clear up to now. A further evidence that these InN layers grown with low ammonia flow have unusual properties is the ellipsometric measurement. The effective dielectric function measured on these layers is shown in Fig. 7.8 (a) in comparison with a measurement on a typical InN layer grown at 580°C (b). In the low energy range, sample (a) grown at 520°C shows a higher background, probably due to the effects of metallic Indium on the surface, as shown also by the AFM images. In the high energy range the electronic interband transitions of the two layers are also different. Measurement (b) presents a typical lineshape for layers with good crystalline and electronic properties. The three peaks were previously assigned to higher electronic interband transitions (see Chapter 4).

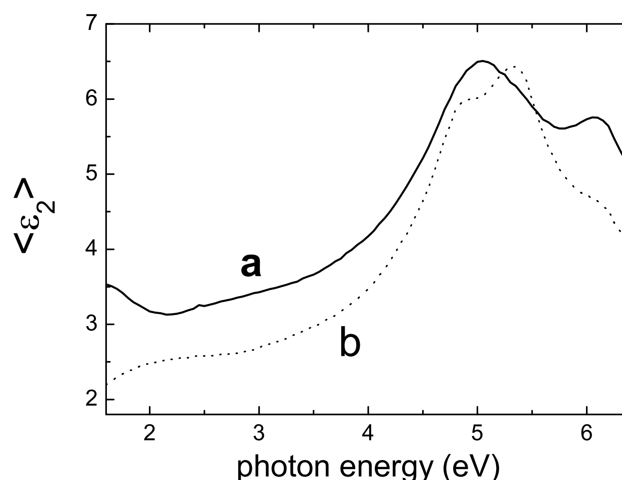

Figure 7.8: *$\langle \varepsilon_2 \rangle$ measured in-situ at room temperature on two InN layers. The dotted line belongs to a layer grown at high temperature with 3 L/min ammonia flow. The solid line belongs to a layer grown at lower temperature, 520°C, with lower ammonia flow, 1 L/min. The lineshape of $\langle \varepsilon_2 \rangle$ for the two layers is very different, probably due to different dielectric properties of the two layers.*

For measurement (a) the first two peaks are merged together and the third peak is unusually well defined. The significance of this difference lies in different dielectric properties of the two materials. In other terms, the large number and/or the different nature of the defects in the layer grown with low ammonia flow, resulting from various characterization, lead to material properties different from the material properties of other InN layers which are less defective. XRD analysis suggests strong presence of cubic inclusions, which are also a possible reason for the different lineshape of layer (a).

In summary, the layers grown with a low ammonia flow are most probably largely defective and are not well defined InN layers. On the other hand, the smooth morphology and the suppression of layer peeling-off open new possibilities for developing the ideal nucleation layer for the growth of InN on sapphire.

7.6 Growth on GaN nucleation layers

The use of a GaN buffer layer further improves the crystalline quality and allows for growth of thicker InN layers. 50 nm thick GaN buffer layers were grown directly on sapphire at low temperature after nitridation. Subsequent annealing was performed at 1050°C. Some samples were additionally prepared with a 300 nm thick GaN layer

grown at 1050°C. By this procedure InN layers with thickness up to 300 nm have been successfully grown on 50 nm and 350 nm thick GaN layers, showing good crystal quality. Ellipsometry transients at 5 eV showed only constant values for the ellipsometric parameters up to these thicknesses. The surface morphology of a 250 nm InN layer investigated by SEM clearly shows a close layer free from damages produced by the peeling off (see Chapter 4). Further optimization of the growth conditions is still necessary for a close, defect free thick layer. In this case, it is demonstrated that GaN buffer layers allow for growth of InN layers with thicknesses beyond 150 nm (the critical thickness for peeling off of InN layers from sapphire) with complete suppression of layer peeling off.

In Fig. 7.9 the PL measurement on an InN/sapphire layer (a) is compared with the measurement on a InN/GaN/sapphire layer (b). Sample (a) was grown on sapphire after 1 minute of nitridation, while sample (b) was grown on top of a GaN layer 50 nm thick, which was grown at 550°C and then annealed for 5 minutes at 1050°C prior to InN growth. Both InN layers were $\sim$120 nm thick and were grown at 520°C. PL was measured by using an InAs detector. The sensitivity of InAs detectors is at least two order of magnitudes smaller than InGaAs (used for the measurements shown in Fig. 7.7, but, on the other hand, the fundamental bandgap of InAs is narrow enough (0.354 eV) to allow the detector to measure in the region where the InN bandgap is expected. The maximum peak intensity of sample (a) is 200 times smaller than that of sample (b) (InN/GaN/sapphire). The energy of the peak center is shifted to lower energy in the case of the InN layer grown on GaN, but there is not corresponding measurement of the crystal properties neither of the electronic properties showing a corresponding improvement of the quality of the layer. In this case, the Hall measurement is not useful for determining the number of carriers on the InN layer grown on GaN, since the measurement would be affected by the properties of the GaN nucleation layer. On the other hand, X-ray measurements on the (0002) reflection of InN do not clearly indicate superior crystallinity of the InN/GaN layer.

A Transmission Electron Microscopy (TEM) measurement of InN/GaN samples is shown in Fig. 7.10. The image of the InN/GaN sample shows four regions with different contrast. They are, from the bottom, the sapphire substrate, the GaN thin buffer layer, the InN nucleation layer on GaN, the thick InN layer. The InN nucleation on GaN was done at 450°C, and the thicker layer on top was grown at 520°C. The contrast of the InN layer is very good when compared with InN layers grown directly on sapphire (TEM images of InN/sapphire in Fig. 5.10). This may be an indication for higher crystal quality of the InN/GaN sample. Also, the InN surface is smooth. However, the InN/GaN interface is not continuous and it is characterized by voids. The voids are also present when InN is grown directly on sapphire and this is probably the reason for the peeling off (delamination) of the InN layer. This result shows that a GaN nucleation layer is very promising for InN growth, but also that the InN/GaN interface needs further optimization.

InN was grown also on 300 nm thick GaN templates (at this thickness the surface of GaN reaches coalescence [98]). A cross section SEM image measured on this wafer is shown in Fig. 4.4. The GaN/InN interface looks continuous on this layer. The reason could lie in the improved properties of the GaN template after coalescence. Cathodoluminescence (CL) was measured on this layer and it is shown in Fig. 7.11.

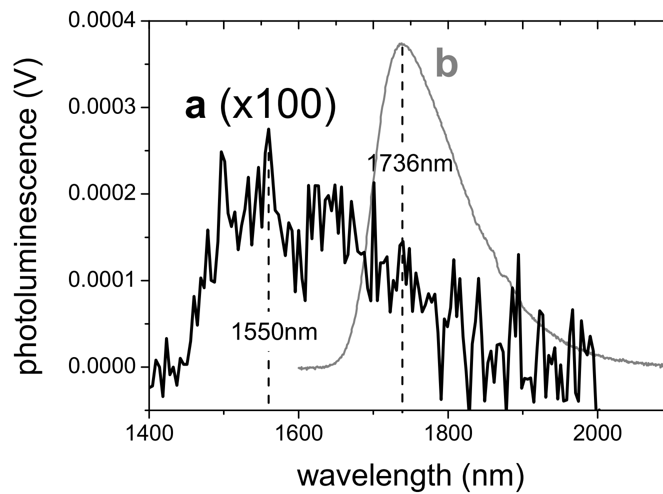

Figure 7.9: *Photoluminescence emission at 20 K of InN layers, excitation with an Argon ion laser at 488 nm measured with a InAs detector. Both layers were ∼120 nm thick. The maximum peak intensity of the InN/GaN/sapphire sample (b) is approximately 200 times higher than for the InN/sapphire sample (a). The peak position of sample (a) is shifted toward lower wavelength (higher energies).*

Figure 7.10: *Transmission electron microscope image of a InN/GaN/sapphire sample. The three layers are recognizable by regions with different contrast. At the interface between InN and GaN it is possible to recognize voids of the size of several tens of nanometers.*

The interpretation of the CL peak is similar to the interpretation scheme adopted for PL: the band-to-band recombination which indicates the fundamental bandgap apart for a Moss-Burstein shift. The CL peak occurs at ∼0.8 eV.

Scanning Tunnelling Spectroscopy (STS) measured the value of the bandgap at the surface by measuring I/V characteristics. A typical measurement result for both InN/GaN sample and for InN/sapphire sample is shown in Fig. 7.12 in terms of dI/dV versus V, and the corresponding value for the bandgap at the surface is ∼1.4 eV. The

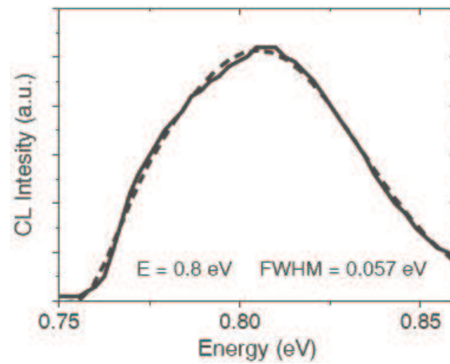

Figure 7.11: *Cathodoluminescence emission at 80 K centered (solid line), the dashed line shows the Gaussian curve fit which calculated the peak center at 0.81 eV, a FWHM of 0.06 eV. The sample was a 250 nm thick InN/GaN/sapphire sample investigated using 10 kV, 8 nA and a scan area of 89 µm×71 µm. A 1.3 eV long band pass filter was used to block second-order emission from the sapphire substrate. This measurement was done on samples grown at the TU-Berlin and it is published in [132].*

large difference with the PL and CL measurements is not clear, but most probably arises from the formation of an oxide on top of the InN surface. The oxide form of In_2O_3 has a bandgap of ~3.5 eV and the STS has probably measured an average value between bulk InN and the contaminated top surface layers.

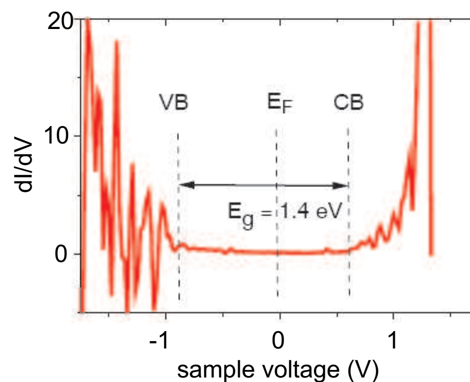

Figure 7.12: *Typical differential conductance (dI/dV) curve measured on InN/sapphire (100 nm thick InN) and on InN/GaN/sapphire (250 nm thick InN) showing a surface bandgap of 1.4 eV. These data were collected at many locations on two different layers (an 120 nm thick InN/sapphire layer and a 250 nm thick InN grown on a GaN/sapphire template), indicating that the tunneling onsets are not spatially localized. This measurement was done on samples grown at the TU-Berlin and it is published in [132].*

7.7 Chapter Summary

In this chapter nucleation of InN on sapphire and homoepitaxial growth were discussed. Growth on GaN buffer layers was also reported. The results show that the InN layer quality strongly depends on temperature and that temperatures higher than the decomposition temperature, simultaneously with high flux of TMIn, can be used to grow InN layers with improved quality. InN can be grown on GaN without layer peeling off and with improved crystal properties. A procedure for growing InN on sapphire without peeling off was developed, which should result in a suitable procedure for an optimal InN nucleation layer. The nucleation of InN on sapphire and GaN must be, on the other hand, further investigated.

One of the aims of this work was the in-situ study of the dielectric function of InN (focus of Chapter 8) and this task is more easily accomplished when measuring on a InN/sapphire system rather than on a InN/GaN/sapphire system where the GaN layer is not well defined and the properties of the InN layer are only partially improved. As an outlook, in light of the preliminary results presented in this section the choice to grow InN on thick, well defined GaN/sapphire templates with good surface morphology or even on GaN wafers is very promising for improving the quality of the InN layers. Also, the knowledge gained on the dielectric properties of InN (discussed in the next chapter) will result in a powerful tool for an analytical discussion of the ellipsometry spectra of InN during growth on GaN or on an improved InN/sapphire nucleation layer.

8. Dielectric function

This chapter deals with the development of a model for the dielectric function of InN which can be used for in-situ monitoring. This includes also comments on the most common surfaces which could occur during growth and the study of the temperature dependence. The advantage of the model proposed here over the few results already published ([32, 33]) is that the optical properties of the layers are measured before any exposure to air, avoiding a still not well defined contamination (oxygen or carbon) that seems to contribute strongly to the surface accumulation layer in InN [67]. Given this, the effort of deriving the InN dielectric function ε from in-situ measurements is of clear relevance.

8.1 Room temperature dielectric function

The dielectric function of InN at room temperature was evaluated from the following steps: (i) among a large set of measurements, the InN spectrum of the layer with best crystalline, morphologic and optical properties was selected; (ii) substraction of the effect of the layer roughness; (iii) evaluation of the effect of the InN nucleation layer (sapphire/InN interface); (iv) development of a parametric model composed of a set of harmonic oscillators to simulate the InN dielectric function. The whole evaluation process is reported in Appendix A, here only the result is shown in Fig. 8.1.

The approximations that were used can be summarized in the following 4 points:

1) The reference spectrum is measured on state-of-the-art InN layers, which display a high background carrier concentration and a relatively high content of defects.

2) The subtracted roughness is still arbitrary. Measurements on smooth layers can improve the confidence on this analysis step.

3) The electronic transition over the non-parabolic fundamental bandgap has been simulated with an energy of 0.7 eV and with a set of oscillators to arbitrarily fit the *plateau* in $\langle\varepsilon_2\rangle$. Thus, with the presented model no conclusion can be drawn about the bandgap behavior.

4) The effects of the nucleation layer were neglected: care has to be taken for the evaluation of spectra in the low energy range (below 3.5 eV);

The harmonic oscillators used for fitting the imaginary part of Fig. 8.1 are shown in Fig. 8.2. Their energy center position and broadening is, strictly speaking, depending on the dielectric properties of the grown material. Thus, the harmonic oscillators can be now used as a fitting parameter for measurements on different layers in order to discuss, for example, the effect of point- and extended- defects, of dopants, of different polymorphs.

Presently, the exact assignment of the critical points of the Brillouin Zone of wurtzite InN is not yet clear [58]. Therefore, the labelling used here for the electronic interband transitions (E_1, E_2, E_3 etc.) follows an empirical scheme.

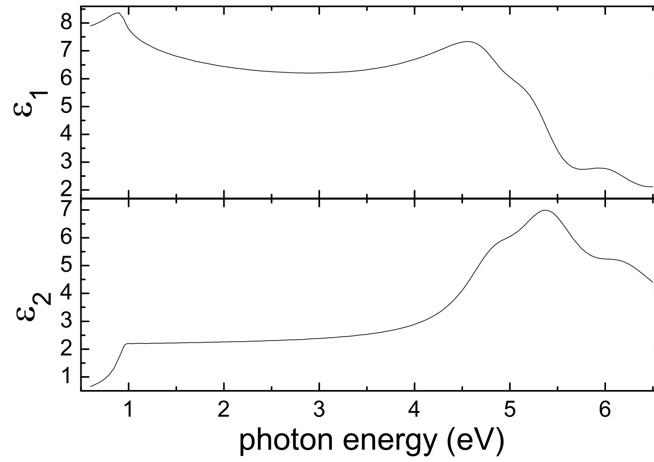

Figure 8.1: *Material dielectric function for InN. The analytical procedure utilized for the extrapolation is reported in Appendix A. The range of validity is summarized in the text.*

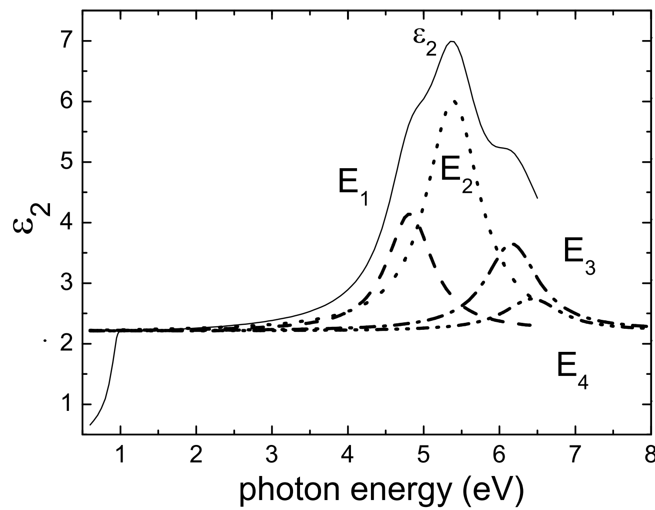

Figure 8.2: ε_2 *for InN. The harmonic oscillators used to approximate the higher electronic interband transitions are shown.*

8.2 Effects of roughness and metallic In

The surface of InN during growth can strongly vary depending on the growth conditions. Typically, growth can influence changes in morphology and in the transition between In-rich and N-rich surfaces. The most prominent features of a surface of the as grown InN layers are the formation of droplets of metallic Indium and the roughness.

Metal-rich surfaces can be simulated by using a multi-layer approach where the metal is used as top layer. Metallic Indium can appear with homogeneous distribution, made up of a few monoatomic layers (as for epitaxy of GaN by MBE [25], where the GaN surface is covered by a bi-atomic layer). The multilayer model uses again four layers, with a thin metallic Indium layer instead of the rough layer on top of InN. The dielectric function of pure metallic Indium from reference [133] (spectroscopic ellipsometry measurement) is used. The effects of different thicknesses of the Indium metallic layer is given in Fig. 8.3, top.

Metallic In can also form droplets on the surface, leading to the formation of small crystallites on the top of the growing surface. In this case in the 4-layer model the third layer, above InN, is a Maxwell-Garnett-EMA, with 3% Indium as guest in vacuum, the host. The effects of different thickness of the layer simulating Indium droplets is plotted in Fig. 8.3, center. Compared to the formation of a metallic thin layer (Fig. 8.3, top), the changes due to droplets are similar for $\langle\varepsilon_1\rangle$ but weaker for $\langle\varepsilon_2\rangle$

For changes in morphology of the InN layer a Bruggemann-EMA of 50% air and 50% InN can be used as a top layer, where increasing roughness corresponds to an increase in thickness. The model calculations are shown in Fig. 8.3, bottom. They were performed for a 4-layer model: vacuum/roughness/InN/sapphire. InN layer was 400 nm thick: interferences are visible in the low energy range, below 3.5 eV and roughness was simulated by a Bruggemann-EMA 50% vacuum and 50% InN. The thickness of the rough layer was the varying parameter. According to this model rougher surfaces lead to lower amplitudes of $\langle\varepsilon_2\rangle$ at E_2 and E_3 and to higher amplitudes below E_1. $\langle\varepsilon_1\rangle$ decreases over the whole spectral range.

With increasing roughness, $\langle\varepsilon_2\rangle$ in Fig. 8.3, bottom, shows a decrease in amplitude in the high energy range (in the region of the high interband transitions) and an increase in amplitude in the low energy range. Spectral changes in $\langle\varepsilon_2\rangle$ in Fig. 8.3, top (metallic overlayer) are also different from the changes in Fig. 8.3, center (droplets) in the low energy range: in the first case the increase is much stronger in the high energy range (like a simple addition of the In plasmon characteristic feature to the dielectric function of InN).

The comparison between the model calculations in this section leads to two main conclusions: first, the effective dielectric function is very sensitive (at the submonolayer level) to changes in morphology and to presence of metallic In on the surface; second, the simulation of the three surface effects leads to characteristic features in the $\langle\varepsilon_2\rangle$ spectra (while in the $\langle\varepsilon_1\rangle$ the spectral changes are comparable) and can therefore be identified.

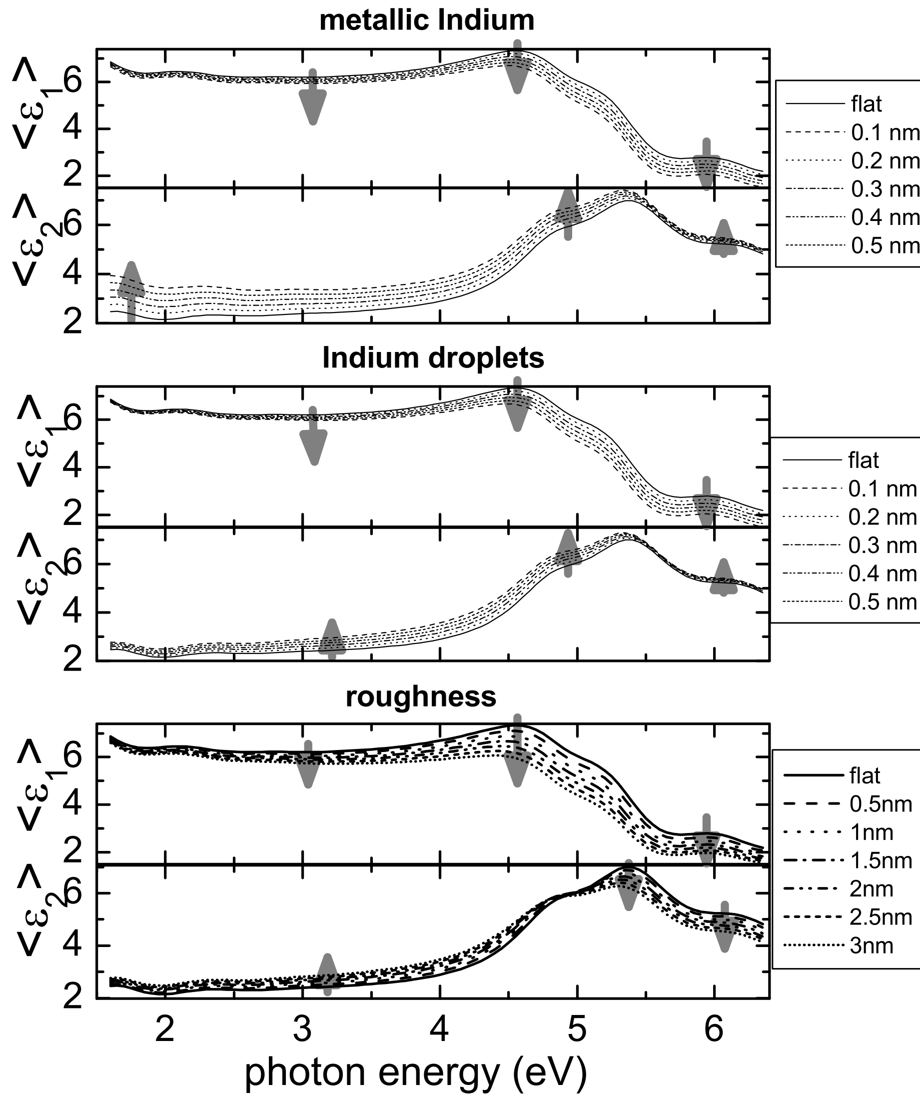

Figure 8.3: *Model calculations of $\langle\varepsilon\rangle$ for 400 nm InN on sapphire with different surfaces. The grey arrows indicate changes in $\langle\varepsilon\rangle$ due to surface deterioration. The legend at the side of each graph shows the increasing thickness of the layer of interest, top: metallic Indium, center: Indium droplets (MG-EMA 3%In in air), bottom: roughness (B-EMA 50%air-50%InN).*

8.3 High-temperature dielectric function

A material dielectric function is useful for in-situ growth applications only if it is known as a function of temperature. Experimental results are necessary to evaluate the red-shift of each critical point and their respective broadening (among semiconductors only few exceptions display a blue shift, namely the Lead-VI compounds). An evaluation procedure of ε as a function of temperature is described in detail in reference [30].

As discussed in Chapter 2 the main effects of increasing temperature on the dielectric function can be summarized as: (i) a red-shift of the peaks of the electronic transitions and (ii) thermal broadening of the peaks.

The effective dielectric function of InN measured at temperatures between 25°C and 500°C is shown in Fig. 8.4. The InN layer was about 100 nm thick and grown directly on sapphire. The energy region of interest is above 4 eV, where the peaks identified as higher interband transitions are shifting to lower energies with increasing temperature. The grey arrow is indicating the shift, the structure below 4 eV is due to interferences.

For analysis of the critical points the second derivative of the dielectric function allows for a more precise determination of the position and of the broadening of peaks

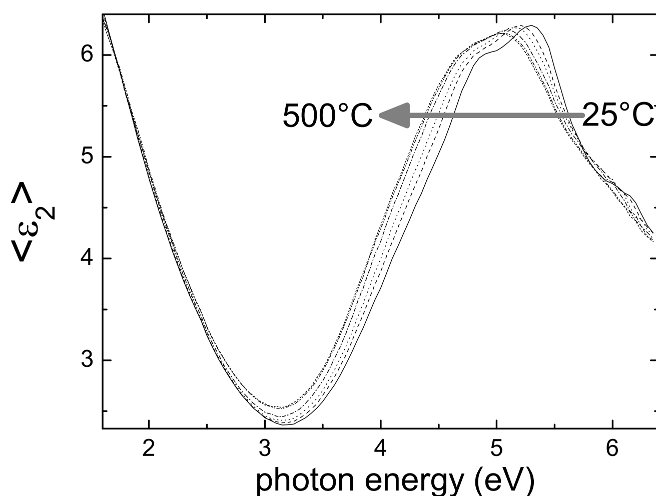

Figure 8.4: *Imaginary part of the effective dielectric function measured on a 100 nm thick InN layer grown on sapphire. Directly after growth, the layer temperature was decreased to room temperature. After that, and prior to air exposure, the layer was heated to 100°C and then in 100°C steps up to 500°C, measuring an ellipsometry spectrum at every step.*

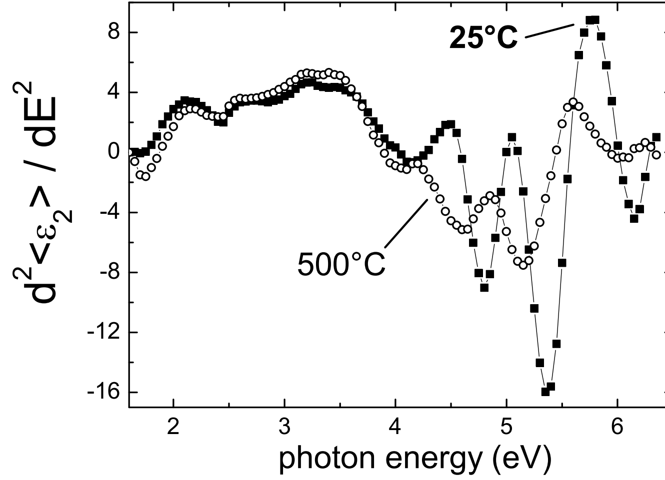

Figure 8.5: *Smoothed second derivative of the imaginary part of the effective dielectric function for measurements at 25°C and at 500°C. The derivation allows for a better separation and a clear identification of the interband transitions.*

[11, 134]. The second derivative of the smoothed $\langle\varepsilon_2\rangle$ curves is shown in Fig. 8.5 for 25°C and 500°C. This mathematical operation allows for a more precise identification of the peak positions (the minima in Fig. 8.5). It can be seen that the interference features in the low energy range are not giving rise to structures in the second derivative.

The second derivative is shown together with the fit of harmonic oscillators in Fig. 8.6 at different temperatures for the relevant energy range. The shift in energy and the broadening is indicated by grey arrows in the figure.

The energy position of the critical points is extrapolated for all the measured temperatures and plotted in Fig. 8.7 together with the broadening. With these results, the dielectric function of InN in the temperature range 300 K to 800 K could be calculated and it is shown in Fig. 8.8.

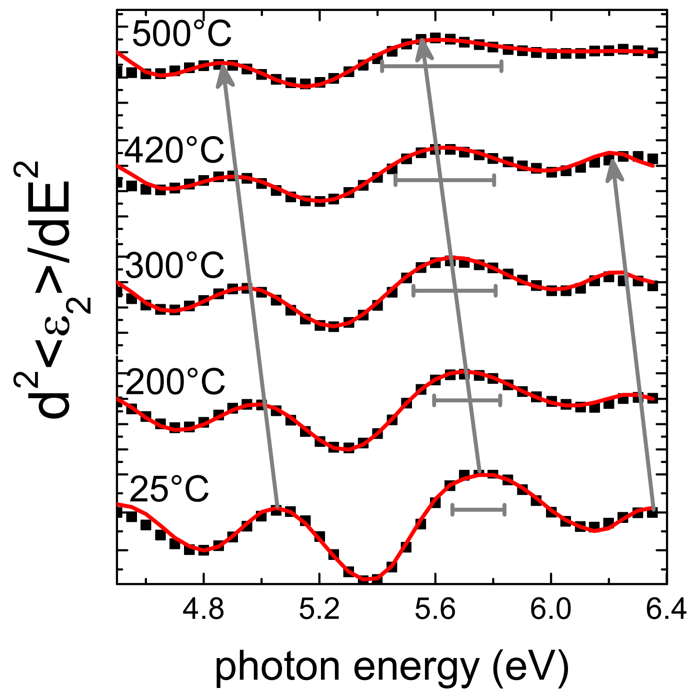

Figure 8.6: *Second derivative of the imaginary part of the effective dielectric function for measurements at 25°C to 500°C (dots). The measurements are the squares, the oscillator fits are the full lines. Arrows and bars are guide to the eye for the shift of the peaks and the broadening of E_2, respectively.*

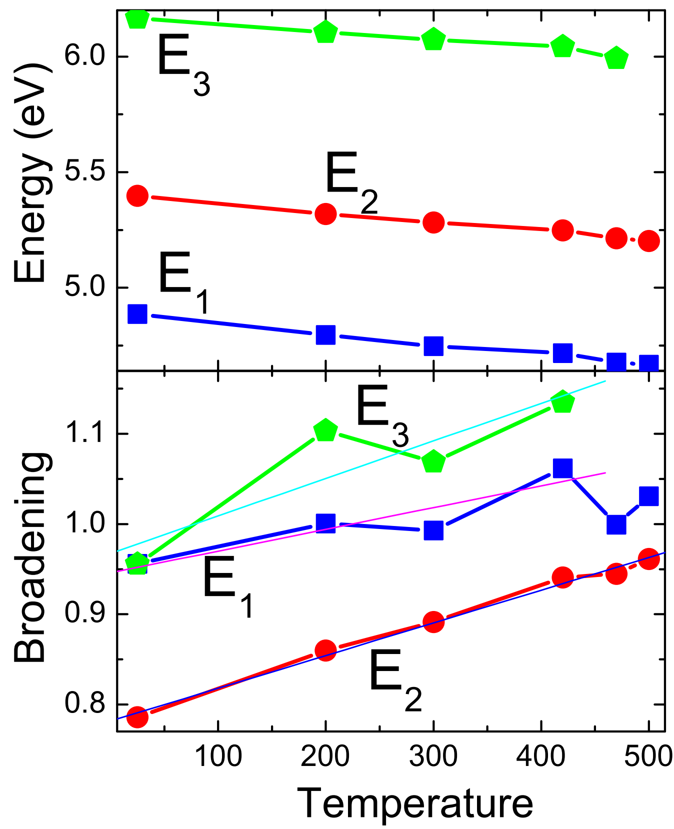

Figure 8.7: *Shift of the energy position and broadening of E_1, E_2 and E_3 resulting from the fit of the oscillators to $\langle\varepsilon_2\rangle$" for temperatures from 25°C to 500°C. The Varshni fit leads to the following values for the α paramter: $\alpha(E_1)$=4.5×10^{-4} eV/K ; $\alpha(E_2)$=4×10^{-4} eV/K ; $\alpha(E_3)$=3.6×10^{-4} eV/K.*

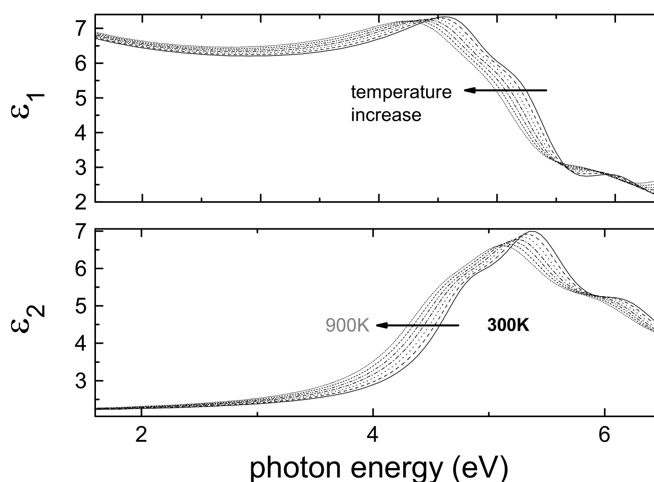

Figure 8.8: *InN dielectric function calculated in the temperature range 300 K to 800 K in 100 K steps.*

A Varshni fit of the temperature behavior (see Chapter 2, reference [28]) leads to the fit of parameter α of equation 2.19 which reads: $\sim 4 \cdot 10^{-4}$ eV/K for the 3 electronic transitions. The constant α is related to the electron-phonon interaction. The complete set of values for each of the three critical points is given in Fig. 8.7.

8.4 Examples

With a known InN material dielectric function and its dependence of temperature it is possible to fit to in-situ measurements. For this purpose in Fig. 8.10 the real part $\langle \varepsilon_1 \rangle$ and the imaginary part $\langle \varepsilon_2 \rangle$ of $\langle \varepsilon \rangle$ for the measurement (squares) and for the fit of a model calculation (full lines) are compared for different growth times, from 45 minutes to 70 minutes. The 6-layer model shown in figure Fig. 8.9 was used, where the surface of InN was modelled by considering roughness and metallic Indium as droplets and as a thin overlayer. The number of parameters is high (each of the six layers carries at least one fitting parameter, the thickness) but this only reflects the complicated growth of InN. The results of the fit should be judged by the comparison between measurement and calculation in Fig. 8.10. Below 3 eV the inhomogeneities of the InN layer lead to differences and difficulties to fit the overall thickness of the InN layer. On the other hand, above 3 eV the position and the shape of the electronic interband transitions is reproduced very well by the model calculation. The results of the fit are plotted in Fig. 8.11. The calculated growth rate is the same as determined by other methods. By growing thicker layers, the roughness of the InN surface increases. The

thickness of the Indium metallic layer on the InN surface is plotted on the right of Fig. 8.11. It is given as the total amount of metallic Indium, since the droplets do not play a significant role in the fitting. Fig. 8.11 (c) shows that Indium appears to initially increase and then to decrease again after ~55 minutes of growth. At this time, the maximum of Indium on the surface might be related to a critical moment of the growth of InN. This preliminary analysis sets the initial question of this work: "how to improve InN growth?" at a new level, paving the way for further improvements of MOVPE grown InN layers.

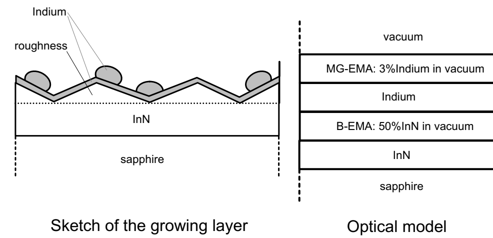

Figure 8.9: *Schematic representation of the surface of InN during growth (left) and the corresponding optical model which was adopted for the model calculations in Fig. 8.10 (right).*

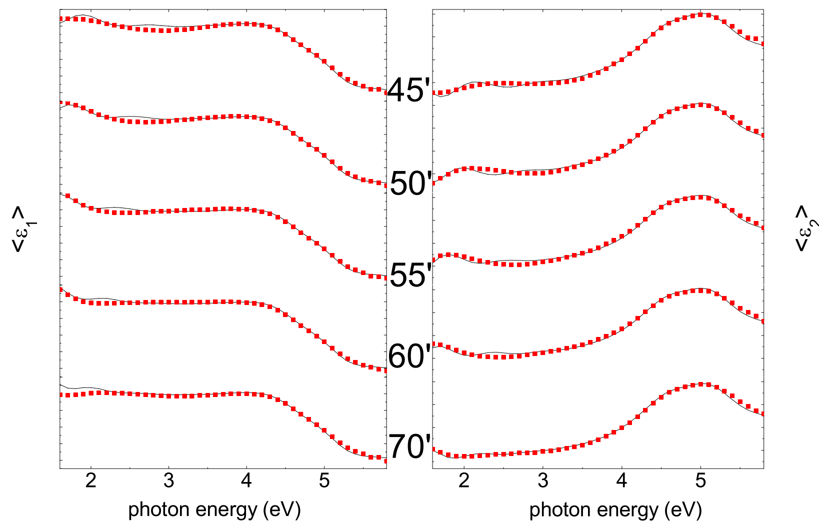

Figure 8.10: *In-situ measurement spectra (symbols) of the effective dielectric function during growth at different growth times, as indicated in between the two graphs. The fits of the model calculations from the model in Fig. 8.9 are shown as full line.*

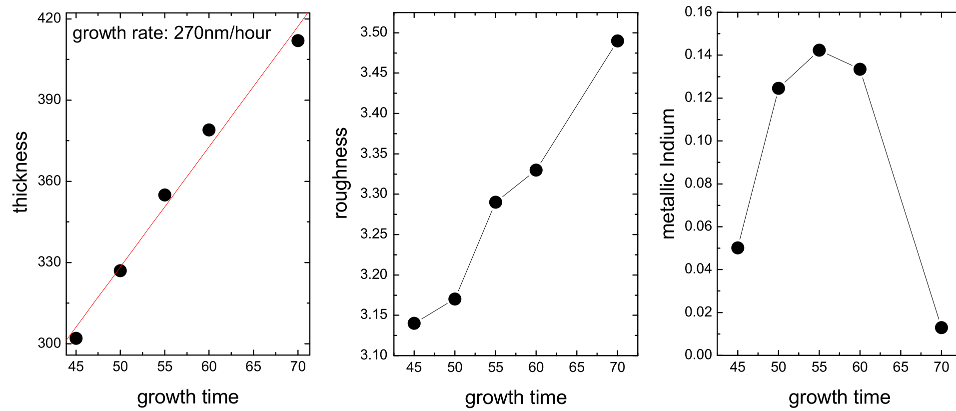

Figure 8.11: *Results of the fit to the measurement spectra of Fig. 8.10 for the different growth times. Shown on the left is the thickness of the InN layer, in the middle the surface roughness (the Bruggemann-EMA InN-air), on the right metallic Indium (essentially the thickness of the thin metallic overlayer).*

8.5 Chapter summary

A model for the dielectric function of InN was suggested and the most important effects on the surface of InN layer during growth were simulated qualitatively and quantitatively. With this model for the InN dielectric function is possible to fit the optical properties of the InN layers measured during growth. As an outlook, the possibility to understand the growth of InN and to improve the quality of the MOVPE grown crystal can be dramatically improved by the use of the material dielectric function.

9. Summary

InN was grown on sapphire and on GaN/sapphire layers by MOVPE. Growth was analyzed by in-situ spectroscopic ellipsometry but also by several ex-situ techniques for different aspects.

The peeling off of InN/sapphire layers was characterized. When the InN layer coalesces, it form bulges and then, at ~150 nm thickness it partially breaks off (or peels off), leaving large holes the size of some μm. This phenomenon can be partially suppressed by using nitrogen as carrier gas during sapphire nitridation or by growing on a GaN template. A promising solution is the growth of an InN nucleation layer on sapphire at low temperature with low ammonia flow. This procedure leads to layers which are up to 300 nm thick and do not have peeling off. Even if crystal quality is lower, they can be still used as templates for InN growth at higher temperature.

Epitaxial InN desorbs in nitrogen above 520°C, above 500°C in ammonia, above 340°C in hydrogen. Annealing in nitrogen ambient at 540°C leads to smoothing of the InN surface.

Nitridation of sapphire with ammonia forms AlN due to exchange reaction of Oxygen with Nitrogen. It has kinetics of the first order and an activation energy of 0.9 eV. The ellipsometric parameter $\tan\Psi$ can monitor the surface reaction, which lasts always for 45 s at temperatures between 950°C and 1075°C, using different ammonia partial pressures. Nitridation longer than 45 s leads to growth of the AlN layer and to surface roughening. At 1050°C nitridation temperature, the InN layers with best electric properties are also grown after 45 s nitridation of sapphire.

We developed a novel procedure for InN epitaxy. Nucleation was done at low temperature (520°C). Temperature was then increased during growth up to 580°C (above its thermal desorption limit), simultaneously with the increasing of TMIn flux. We achieved higher growth rate and layers with improved crystalline and optical properties.

Finally we have evaluated the optical properties of InN and their dependence on the temperature. The model developed for the dielectric function of InN can now be used to determine analytically the state of the bulk and of the surface of InN during epitaxy.

This work answers basic questions of epitaxy of InN. It develops a growth procedure for layers with improved properties and it suggests, as outlined, several possible improvements. The optical properties of InN can be used for an analytical evaluation of in-situ experiments during InN epitaxy. The quality of the InN layers was strongly improved, giving a positive indication towards the possibility of a better understanding of InN and towards its use in electronic devices.

A. Extrapolation of the InN dielectric function

The steps to evaluate the dielectric function of InN at room temperature are as follows: (i) among a sufficiently large set of measurements, selection of the best data to be used for further analysis; (ii) subtraction of the effect of the layer roughness; (iii) comment on the effect of the InN nucleation layer (sapphire/InN interface); (iv) development of a model of the InN dielectric function and fit it to the experimental data. Each of these steps is extremely delicate and has introduced uncertainties in the development of the model. Several iterations were done in order to improve the evaluation process.

A.1 Evaluation of the measured spectra

The aim of this section is to select a suitable measurement of the effective dielectric function of InN to be used as a base for the interpretation of the in-situ spectra measured during growth. The selected spectra will be called "reference spectra".

A large amount of in-situ measurements is available. Only room temperature (RT) effective dielectric functions will be considered. Measurements at room temperature are in fact more accurate since they are less influenced by thermal effects on the ellipsometric set-up or by position changes of the sample.

Since InN is virtually a new material it is also important to compare measurements with literature results and to analyze criteria to identify the layers with dielectric properties as close as possible to single crystal hexagonal InN.

References for comparisons are experimental results published by Kasic [32], Goldhahn [33] and Cobet [58], together with ab-initio calculations from Bechstedt [42]. At this point, it is worth reminding the reader again that the relevance of this work is the unique possibility of discussing InN optical properties directly after epitaxy and *prior* to any contamination of the surface which, in turn, might have affected the measurements of other authors.

The morphology of the InN samples grown in this work have been assessed through AFM, SEM and optical microscopy, the structural characterization with X-Ray diffraction and the electronic properties with Hall. The optical properties have been studied also by PL and Raman spectroscopy. In summary, these results show that the vast majority of samples display properties comparable to the ones measured by other groups and summarized in Chapter 3. The ex-situ characterization has restricted our focus on a set of samples grown with an improved growth procedure at 580°C with different nitridation of the sapphire substrate. These samples are the thickest grown up to now in our laboratory (between 300 nm and 400 nm) and display the best quality. The dielectric function of other layers with different thickness, different surface morphology and also with different dielectric properties (i.e. defects

influenced the dielectric function) will also be shown for comparison.

The main discussion will start with the imaginary part of the measured effective dielectric function which is proportional to absorption. The real part will be discussed in a second stage. In Fig. A.1 (a) are shown the imaginary part of the dielectric function of several InN layers grown at 580°C with different nitridation of the sapphire substrates. To simplify the discussion, the main features in the spectra can be divided in two regions, the first above 3.5 eV and the second below.

The fundamental bandgap is still discussed, but the results of this work fit best when a narrow bandgap is assumed. Therefore a bandgap for InN at around ∼0.7 eV is assumed, as suggested by other authors [2, 42, 135]. Between 1.6 eV and around 3.5 eV the penetration depth of the light is still comparable with the InN layer thickness. Therefore we find features related to interferences between the InN/air and the sapphire/InN interfaces. This is reasonable, because the penetration depth of the light for other semiconductors is generally in the range of some 100 nm between the fundamental bandgap and the higher interband electronic transitions [7]. All the layers display a maximum at around 2 eV in Fig. A.1 (a), meaning that these layers have very similar thickness. Their thickness was measured by cross section SEM and via measuring the sample mass (weight) before and after growth and evaluating the amount of InN present on the sapphire substrate. The layers resulted in having different thicknesses, between 300 nm and 350 nm, in spite of the fact that the interferences measured by ellipsometry (Fig. A.1 (a)) shows that the layers should have more or less similar thicknesses. This misfit with the ellipsometric result might be due to the non-homogeneity of the layers. Ellipsometry measures on a sample surface of circa 2 mm^2. The thickness of the InN sample may vary strongly in this area, as discussed in Chapter 4. The ellipsometric measurement would then result from an average over the different thickness sampled. It is therefore safe to assume that the average thickness sampled by ellipsometry is reasonably similar for all the samples in Fig. A.1 (a).

The differences among the spectra in this energy range lies in the different amplitudes of epsilon imaginary. There are at least two possible reasons for this difference: increasing roughness of the layer surface leads to higher amplitude and increasing amount of metallic In on the samples surface leading also to higher amplitude (these tendencies are shown in Chapter 8). In both cases, a lower amplitude is preferable in this energy range. With this requirement, the energy spectra with a solid line in Fig. A.1 (a) is the best candidate for the database. It is also noticeable that these spectra show a somewhat lower thickness, being the maximum of the interference structure shifted at slightly higher energies.

Above 3.5 eV the dominant structures are three distinguishable peaks. By comparison with literature they are assigned to electronic interband transitions. They are, up to now, not yet assigned to specific critical points of the Brillouin zone. The most suitable spectra is in principle the one with the highest amplitude at the higher electronic interband transitions. Lower amplitudes will result from increasing amounts of defects that will in turn lead to damping and to broadening of the spectral features. The higher amplitude might also derive from the presence of metallic In on the InN surface. This is very likely the case if the amplitude is high also in the low energy range (below 3.5 eV). The spectra displaying the higher amplitude above 3.5 eV is the

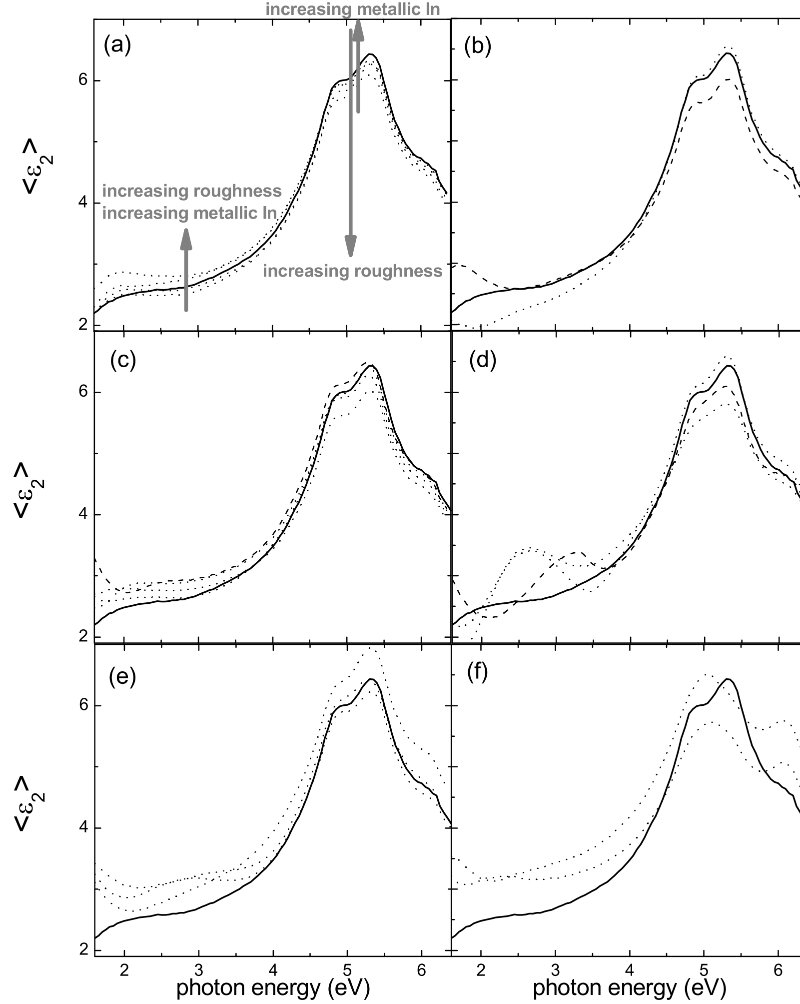

Figure A.1: *Measured $\langle \varepsilon_2 \rangle$ spectra on different InN epitaxial layers. In (a) and (b) is shown the serial of samples with best structural properties (after X-Ray characterization) and electronic properties (after Hall measurements). In (a) all samples have similar thickness (~350 nm), the sample which correspond to the best description of the material dielectric function of InN, according to the criteria described by the grey arrows, is represented with a solid line (sample "A"). In (b), sample "A"is compared with InN layers with slightly different thickness. The dotted line represents sample "B", thinner than sample "A"but even more fitting to the requisites (a). In the remaining, sample "A"is compared with a different sets of InN/sapphire layers. In (c) is shown a set with similarly good properties. In (d) is a thin (100 nm) InN/sapphire layer and two InN/GaN/sapphire layers (InN 100 nm thick, GaN 50 nm thick) showing marked interferences. In (e) similarly thick InN/sapphire layers show less marked interferences and are not describing InN dielectric function as well as sample "A". In (f) is a set of InN/sapphire layers of similar thickness to sample "A"but with improved morphology. Their crystal and electric properties are lower than for sample "A", their dielectric properties appear also to be different.*

dashed line spectra. Since the amplitude of this spectra in the low energy range is among the lowest displayed, one can exclude a predominant presence of In on to the surface of this InN layer.

In summary, solid arguments indicate the solid-line spectra among the others shown in Fig. A.1 (a) as reference spectra that for simplicity from now on will be called sample "A". In Fig. A.1 (b) sample "A" is compared with other spectra from other InN layers. In this case the layers have different thickness, resulting in different interference structures in the low energy range. The difference in thickness is noticeable from the ellipsometric measurement and confirmed by thickness data achieved with other techniques. The shift of the maximum of the interference structure towards low energy indicates the increasing thickness of the layers. From previous criteria (highest amplitude at the higher interband transition and lowest amplitude in the low energy range), the spectra of the thinner layer (dotted line) is also, according to the chosen criteria, the spectra of the best quality layer. From now on, the dotted line is named sample "B". Both sample "A" and sample "B" will be still considered in the following.

The solid line spectra of sample "A" is reported again in Fig. A.1 (c,d,e,f) every time compared with a different set of layers. In Fig. A.2 the spectra already shown in Fig. A.1 (b), with both sample "A" and sample "B", is shown again, this time shown together with $\langle\varepsilon_1\rangle$ and with a guide to the eye for the electronic interband transitions.

A.2 Estimation of roughness

The selection of the reference spectra "B" allows one to start this section about the influence of roughness with the most suitable among the available measured samples. Sample "B" is characterized by a certain roughness, as well as interface effects. These effects can be, partially, evaluated and subtracted from the measurement with a suitable model.

To evaluate the roughness of the sample we have used AFM. The measured rms roughness must be carefully used in an appropriate ellipsometric model. The usual model for the roughness in ellipsometry is a Bruggemann effective medium approximation (BEMA). The rough layer is treated as a layer at the surface composed for 50% of a host (the material) and for 50% of a guest (air). The thickness of this Bruggemann roughness can be compared to the rms roughness measured by AFM taking in account a factor of two [81]. By AFM measurements, rms roughness was between 2 nm and 3 nm. The solid line in Fig. A.3 is the result of the subtraction of 3 nm of roughness, simulated by a Bruggemann-EMA 50% air, 50% InN, from the spectra of sample "A"

A.3 Effects of the InN/sapphire interface

The nucleation layer and, in general, the InN/sapphire interface represents an uncertainty in the model under development, because the interface will possess different dielectric properties with respect to the outer layers because of strain, possible cubic inclusions and voids. Because of these intrinsic difficulties, the discussion of the nucleation layer should be postponed. In terms of penetration depth of the light, it is safe

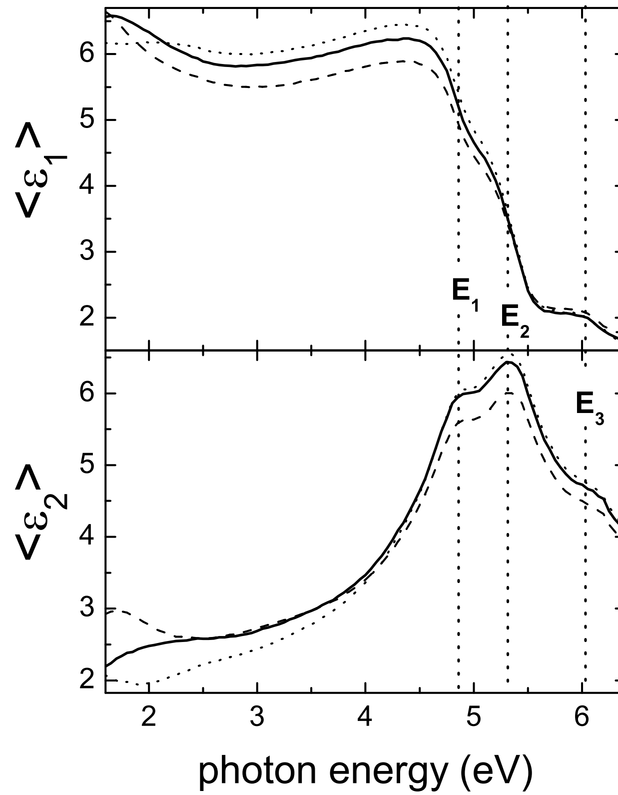

Figure A.2: *$\langle \varepsilon_1 \rangle$ and $\langle \varepsilon_2 \rangle$ measured on 3 different InN layers. The dotted line refers to sample "B", while the solid line refers to sample "A" (previously defined in Fig. A.1). The dashed line belongs to a layer with lower quality, from the interferences below 3 eV results also to be the thicker of the three. $\langle \varepsilon_1 \rangle$ of sample "B" displays an unusual lineshape below 3 eV.*

to consider that the nucleation layer has no influence on the optical measurements above 3.5 eV for the considered InN layers (all thicker than 300 nm). The consequence is that the model developed here is reliable only above ∼3 eV.

A.4 Extrapolation

A.4.1 Approach I: line shaping of ε_2

In a first approach, a test dielectric function is obtained by *flattening* the low energy part (from 1.6 eV to 3.5 eV). The test dielectric function is then used in a 3-phase model, air/InN/sapphire using for the InN layer its real thickness (evaluated with SEM cross section images) in order to be compared with the actual spectra of sample "B". The dashed-line in Fig. A.3 defines the line shape obtained by "flattening" the line shape of sample "B", dotted-line (after removal of 3nm roughness).

Though this is an arbitrary approach, it allowed to obtain a first reference for the imaginary part of the dielectric function. The first simulations performed with this test dielectric function allowed to identify the effects of roughness and metallic Indium with more precision. Roughness causes a damping, as expected, where metallic Indium causes an increase in amplitude over all the investigated energy range. Therefore, the criteria for the choice of the reference spectra were adopted according to these findings.

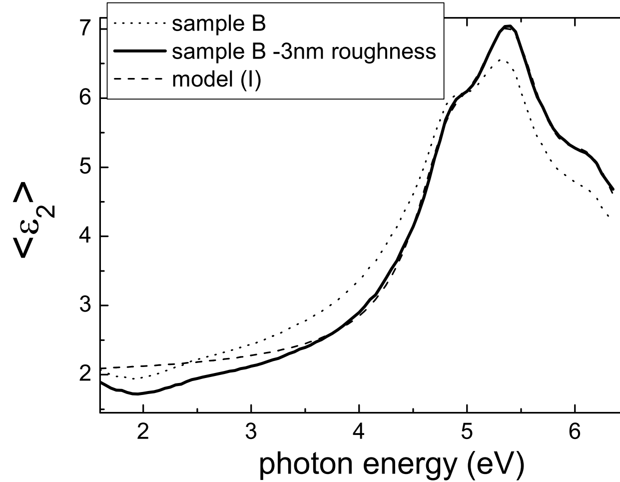

Figure A.3: $\langle\varepsilon_2\rangle$ *of InN/sapphire sample "B" as measured (dotted), after the subtraction of 3 nm roughness (solid) and after modification of the lineshape at low energy (dashed) to eliminate the effects (interferences) originating from the low thickness of the layer grown on sapphire.*

A.4.2 Approach II: harmonic oscillators for ε_2

In a more analytical approach, the imaginary part of the dielectric function is fitted by three harmonic oscillators for each high electronic interband transition. The fundamental bandgap is simply simulated, in this energy range, by a flat plateau of amplitude 2. This is assumed because of the non-parabolicity of the conduction bands (see chapter 2). The 3-dimensional oscillator (originating from the 3-dimensional electronic transition) is then producing the flat plateau shown also from other authors [32, 33, 42]. The model of harmonic oscillators generates a real part which is diverging in the low energy range due to the lack of a model for the 3-dimensional electronic transition (the fundamental bandgap) out of (below) the measurement range. This is shown in Fig. A.4: ε_1 is presented, the dotted line is the Kramers-Kronig calculation of ε_2 where only the interband transitions over 4 eV were considered. The expected line shape is represented by the dashed line (see also [32, 33, 42]). The latter is obtained by a fourth oscillator centered at 0.8 eV, only for the real part of the dielectric function after some rearrangement. The validity of the ε_1 result is confirmed by the Kramers-Kronig consistency with ε_2.

The weak point of this approach is the low energy range of ε_1, that was arbitrarily drawn to fit to the experimental results and only approximately cross-checked with Kramer-Kronig consistency. In view of these considerations, we are going to propose a third approach for extrapolating the ε of InN.

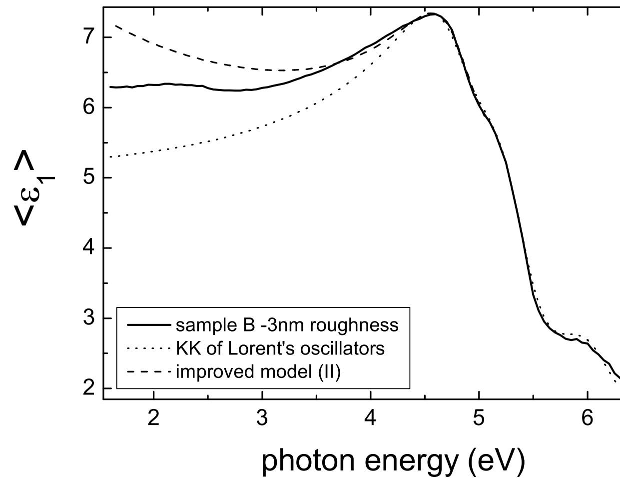

Figure A.4: *$\langle\varepsilon_1\rangle$ of InN/sapphire sample "B" as measured (solid), as result of a Kramers-Kronig transformation of $\langle\varepsilon_2\rangle$ (Fig. A.3, dotted) and after modification of the lineshape at low energy (dashed) to correct for the presence of the bandgap (out of the energy measurement range).*

A.4.3 Approach III: Effects of the fundamental bandgap

In a third approach, the ε of InN is simulated only with harmonic oscillators and with a suitable oscillator for the bandgap. The influence of the bandgap on this measurement range, as seen, is the presence of its peak-tail in ε_1 of InN. This means that, in terms of lineshape, in the energy range 1.6 eV-6.5 eV the effects of the fundamental bandgap below 1 eV cannot be neglected.

In technical terms, an oscillator below 1 eV is needed to take in account the effects of the bandgap in the measured region. Based on what it seems the most appropriate value for the InN fundamental bandgap, [33, 34, 42, 135] we assume a bandgap of 0.8 eV.

The following step is to find the appropriate model for the electronic transition at the fundamental bandgap. The characteristic *plateau* in ε_2 originating from the electronic transition to a strong non parabolic band at the Γ point of the Brillouin zone has been already shown. The main problem is to develop a model for an electronic transition to a non-parabolic conduction band.

As shown in Fig. A.5, a 3-dimensional critical point with parabolic bandgap tran-

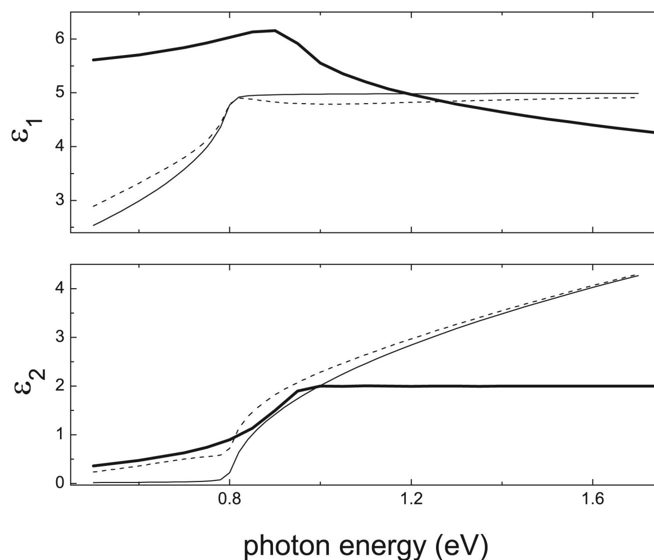

Figure A.5: *Simulation of the dielectric function at the fundamental bandgap. Dotted and solid (thin) lines correspond to different broadenings of a 3-dimensional oscillator which assume a parabolic bandgap. They cannot properly fit the lineshape of a non-parabolic bandgap [34, 42], which is simulated with a set of harmonic oscillators (thick solid line).*

sitions [10] is steadily increasing (dashed and thin solid line), while the non-parabolic bandgap forms a plateau in ε_2 (thick solid line) [42]. Also, the marked peak in ε_1 is hardly reproduced by the electronic transition to the parabolic conduction band. Therefore, such a model gives a poor approximation of the InN dielectric function, even at energies above 1.6 eV (in the case of a fundamental bandgap of 0.8 eV), which is of interest in this work.

Since the aim of this work is beyond the bandgap issue, the *plateau* in ε_2 will be simulated by a set of harmonic oscillators. The resulting bandgap transition is shown in Fig. A.5. The ε_1 spectra calculated with the KK-relations shows the peak at the bandgap position. Such an approach has the following advantages over the previous ones: (i) it will be KK consistent, (ii) it will allow a simultaneous fit to ε_2 and also to ε_1 and (iii) it will allow for the red-shift of its energy position when the dielectric function will have to be calculated at high temperature. At this point the lineshape of $\langle\varepsilon_1\rangle$ for samples "A" and "B" should be revisited. In Fig. A.2, sample "B" (dashed line) does not show in $\langle\varepsilon_1\rangle$ the expected increase below 2.3 eV (which should lead to a peak at ∼0.7eV). The reason for this might lie in the interferences. This means that sample "B" is not typical and also difficult to reproduce: thus, the reference sample used for approach III is sample "A".

After the bandgap has been simulated in this fashion, the dielectric function of sample A can be fitted with the addition of the three oscillators of the high interband electronic transitions already used in approach II with the only difference being a simultaneous fit to ε_1 and to ε_2. In this case, an additional oscillator at high energy and the value of ε_∞ were also fitting parameters, to account for the limited energy range of the measurement.

The resulting model is shown in Fig. A.6, in comparison with InN dielectric functions already published.

A.5 Summary

The InN dielectric function was evaluated from in-situ ellipsometric measurements on InN MOVPE layers prior to any contamination to air. The validity of the model is limited by the approximations of the extrapolation process. A list of these approximation is reproduced in the first section of Chapter 8. What could not be evaluated is the effect of vacancies, oxygen, carbon and other impurities, dislocations, inversion domains, etc. Such defects are present in the layers due to a growth process still in development and are affecting the dielectric properties of InN in a way that it is not possible to foresee yet. In general, it can be concluded that improvement of the layer quality, morphology and thickness is necessary for further refining of the model for the dielectric function of pure InN.

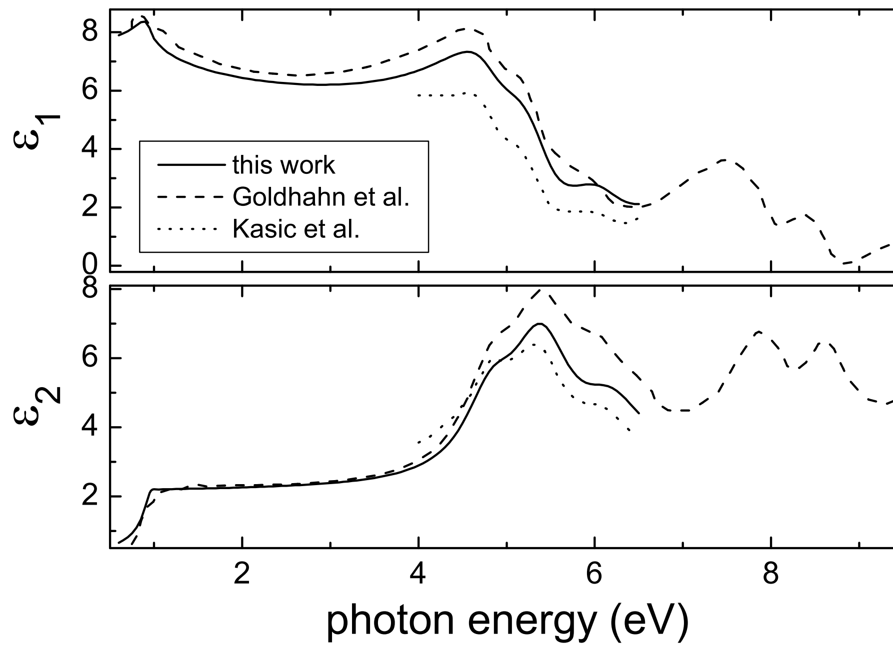

Figure A.6: *The dielectric function of InN proposed in this work (solid line) is shown and compared with results from [32] (dotted line) and from [33]. The spectra are all very similar in lineshape, but differ in amplitude because different roughness were assumed for the surface of the InN layers. Literature results have to care also for the presence of oxygen, since all the spectra ar measured ex-situ.*

Acknowledgements

I would like to express my thank to a lot of people. The list is long, but each of them has had at least a line in this thesis, or a comment during my experiments, or he has cheered me up during the bad times.

The first mention goes here to Professor Wolfgang Richter: without him this work would not exist and I would not have learnt so much. All in all, it was a great professional and personal experience, therefore I am much grateful to him.

Dr. Torsten Schmidtling, with whom I share some of the results of my thesis and of his thesis, for teaching me nitrides in MOVPE and for all the discussions about physics and entertaining topics.

Christoph Werner, for the work together and the time spent in the clean room. For we have learnt a lot together.

George Manolis for his contribution with temperature dependent experiments during sapphire nitridation and for his good nerves also when things do not want to work.

Dr. Udo Pohl for his advices, for his very friendly nature and for his great attitude at teaching physics: everything seemed easy after his explanations.

Dr. Markus Pristovsek for the many, many discussions, for his immense knowledge on MOVPE and for being able, in spite of his *realism* (some would say *pessimism*) to effectively motivate students to learn more about physics. And last but not least, for intense proof reading of a large part of this work.

Dr. Patrick Vogt for his humor and for sharing his jokes, but also for showing great leadership abilities and skills in managing his own group, so surprising for one still so young.

Professor Kneissl for his kindness and for his interest in InN and in this thesis.

All the now-gone generation of PhD students, in particular Christoph Cobet and Karsten Fleischer. A brilliant generation of physicists that helped me with ellipsometry, padminton, and (Karsten) with great fantasy books.

Theo Hermann, for the great time together swimming and drinking a strange German beverage which is made with fermentation of malt.

Sandhia Chandola, for the great time in the Biergarten, drinking the same as above and for a bottle of Paddy she brought me from Ireland, which helped me a lot to

make things work.

And now my generation, starting with Christian Kaspari and Stefan Weeke for the great time spent in the teelabor and in the office speaking about Physics and much, much else.

Tobias Schenk and Eugen Speiser, for the skills they shared with me, for the great discussions, for many other things, but most of all, for their friendship.

Fabian Jachman for hosting me the very first days I have arrived in Berlin and for keeping to invite me to his fantastic parties, but also for helping me with my exam in Experimental Physics.

Bert Rähmer for helping me speaking German and for spending time correcting my German love letters.

And the new generation, starting with Martin Leyer, a good friend in this world and in the role playing one.

Raimund Kremzow and Regina Passman for the evening spent playing and seeing movies at the "teelaborkino", which made fun the late hours spent at university.

Jan Robert Van Look for his stories about girls that he still has to tell me... better he hurries up!

Christian Meissner, the last arrived in the group, nevertheless he has done the last, boring, proof reading of this thesis, pointing to a enormous number of little spelling and formatting errors. Which I could not even fix all!

Outside my colleauge-circle, Nicole deserves a special mention for choosing the hard, painful life of being the girlfriend of a physicist.

Mia sorella Antonella, mamma Lucia, papá Giuseppe e nonna Elena, per avermi continuato a volere bene anche se sono scappato via centinaia di chilometri, lontano lontano.

Andrea, Alessandro and Massimiliano, for being still my friends after all this long time abroad.

Bibliography

[1] T. L. Tansley and C. P. Foley, *Optical band gap of indium nitride*, *J. Appl. Phys.* **9**, 3241 (1986).

[2] V. Y. Davydov, A. A. Klochikhin, R. P. Seisyan, V. V. Emtsev, S. V. Ivanov, F. Bechstedt, J. Furthmüller, H. Harima, A. V. Mudryi, J. Aderhold, O. Semchinova, and J. Graul, *Absorption and emission of hexagonal InN. Evidence of narrow fundamental band gap*, *phys. stat. sol. (b)* **229**, R1 (2002).

[3] W. Walukiewicz, J. W. Ager III, K. M. Yu, Z. Lilienthal-Weber, J. Wu, S. X. Li, R. E. Jones, and J. D. Denlinger, *Structure and electronic properties of InN and In-rich group III-nitride alloys*, *Journal of Physics D: Applied Physics* **39**, R83 (2006).

[4] Shuji Nakamura and Gerhard Fasol, *The Blue Laser Diode - GaN Based Light Emitters and Lasers*, 1997.

[5] J. Wu, W. Walukiewicz, K. M. Yu, W. Shan, J. W. Ager III, E. E. Haller, H. Lu, W. J. Schaff, W. K. Metzger, and S. Kurtz, *Superior radiation resistance of InGaN alloys: Full-solar-spectrum photovoltaic material system*, *J. Appl. Phys.* **94**, 6467 (2003).

[6] B. E. Foutz, S. K. O´Leary, M. S. Shur, and L. F. Eastman, *Transient electron transport in wurtzite GaN, InN, and AlN*, *J. Appl. Phys.* **85**, 7727 (1999).

[7] D. E. Aspnes, *Characterisation of semiconductors and semiconductor structures by photometric and ellipsometric techniques*, In *Proc. SPIE: International conference on physical concepts of materials for novel Optoelectronic device applications*, 1990.

[8] M. Zorn, *Optical in-situ studies and on-line growth control of binary and ternary semiconductors with respect to the (001) surface*, PhD thesis, TU Berlin, 1999.

[9] M. A. Hermann, W. Richter, and H. Sitter, editors, *Epitaxy. Physical Principles and Technical Implementation*, Springer-Verlag, Berlin, Heidelberg, 2004.

[10] Peter Y. Yu and Manuel Cardona, *Fundamentals of Semiconductors*, Springer Verlag, 2nd edition, 1999.

[11] P. Lautenschlager, M. Garriga, L. Viña, and M. Cardona, *Temperature dependence of the dielectric function and interband critical points in silicon*, *prb* **36**, 4821 (1987).

[12] J.-T. Zettler, *Characterization of epitaxial semiconductor growth by reflectance anisotropy spectroscopy and ellipsometry*, *Prog. Cryst. Growth Charact. Mat.* **35**.

[13] D. E. Aspnes and J. B. Theeten, *Investigation of effective medium models of microscopic surface roughness by spectroscopic ellipsometry*, *Phys. Rev. B* **20**, 3292 (1979).

[14] H. M. Manasevit, *Single-Crystal Gallium Arsenide on Insulating Substrates*, *Appl. Phys. Lett.* **12**, 156 (1968).

[15] *Aixtron AG*, URL `http://www.aixtron.com/`.

[16] *Thomas Swan Scientific Equipment*, URL `http://www.thomasswan.co.uk/`.

[17] *Veeco*, URL `http://www.veeco.com/`.

[18] Gerald B. Stringfellow, *Organometallic Vapor-Phase Epitaxy: Theory and Practice*, Academic Press, Inc., 2nd edition, 1999.

[19] J. B. Theeten, F. Hottier, and J. Hallais, *On-time determination of the composition of III-V ternary layers during VPE growth*, *Appl. Phys. Lett.* **32**, 576 (1978).

[20] G. Laurence, F. Hottier, and J. Hallais, *Growth monitoring and characterization of (Al,Ga)As-GaAs heterostructures by ellipsometry*, *J. Cryst. Growth* **55**, 198 (1981).

[21] D. E. Aspnes, W. E. Quinn, M. C. Tamargo, M. A. A. Pudensi, S. A. Schwartz, M. J. S. P. Brasil, R.E. Nahory, and S. Gregory, *Growth of Al(x)Ga(1-x)As parabolic quantum wells by real-time feedback control of composition*, *Appl. Phys. Lett.* **60**, 1244 (1992).

[22] A. Bonanni, K. Schmidegg, A. Montagne-Ramil, H. Sitter, K. Hingerl, and D. Stifter, *Virtual interface approximation model applied to spectroscopic ellipsometry for on-line composition determination of metal organic chemical vapor deposition grown ternary nitrides*, *J. Vac. Sci. Technol. B* **21**, 1825 (2003).

[23] M. Losurdo, P. Capezzuto, and G. Bruno, *Remote Plasma MOCVD Growth and Processing of GaN: A Study by Real Time Ellipsometry*, *phys. stat. sol. (a)* **176**, 733 (1999).

[24] M. Losurdo, P. Capezzuto, and G. Bruno, *The impact of SiC substrate treatment on the heteroepitaxial growth of GaN by plasma assisted MBE*, *Crys. Res. Technol.* **40**, 997 (2005).

[25] C. Cobet, T. Schmidtling, M. Drago, N. Wollschlaeger, N. Esser, W. Richter, and R. M. Feenstra, *Surface termination during GaN growth by metalorganic vapor phase epitaxy determined by ellipsometry*, *J. Appl. Phys.* **94**, 6997 (2003).

[26] K. Seeger, *Semiconductor Physics*, Springer Verlag, Berlin, 2004.

[27] N. M. Ravindra, S. Auluck, and V. K. Srivastava, *Temperature dependence of the energy gap in PbS, PbSe and PbTe*, *phys. stat. sol. (a)* **52**, K151 (1979).

[28] Y. P. Varshni, *Temperature dependence of the energy gap in semiconductors*, *Physica* **34**, 149 (1967).

[29] P. B. Allen and M. Cardona, *Theory of the temperature dependence of the direct gap of germanium*, *Phys. Rev. B* **23**, 1495 (1981).

[30] Thomas Trepk, *Optical properties of III-V semiconductors at high temperatures*, PhD thesis, TU Berlin, 2005.

[31] Y. Ishitani, K. Xu, W. Terashima, N. Hashimoto, M. Yoshitani, T. Hata, and A. Yoshikawa, *Infrared measurements of InN films at low temperatures*, *phys. stat. sol. (c)* **0**, 2838 (2003).

[32] A. Kasic, E. Valcheva, B. Monemar, H. Lu, and W. J. Shaff, *InN Dielectric function from the midinfrared to the ultraviolet range*, *Phys. Rev. B* **70**, 115217 (2004).

[33] R. Goldhahn, A. T. Winzer, V. Cimalla, O. Ambacher, C. Cobet, W. Richter, N. Esser J. Furthmüller, F. Bechstedt, H. Lu, and W. J. Schaff, *Anisotropy of the dielectric function for wurtzite InN*, *Superlatt. Microstruct.* **36**, 591 (2004).

[34] F. Bechstedt, J. Furthmüller, M. Ferhat, L. K. Teles, L. M. R. Scolfaro, J. R Leite, V. Y. Davydov, O. Ambacher, and R. Goldhahn, *Energy gap and optical properties of $In_xGa_{1-x}N$*, *phys. stat. sol. (a)* **195**, 628633 (2003).

[35] *Periodic table of the elements PTable*, URL `http://www.familiataboada.com/IQ/page4.html`.

[36] A. F Holleman and E. Wiberg, *Lehrbuch der Anorganischen Chemie*, Walter de Gruyter - Berlin - New York, 1976.

[37] Linus Pauling, *The Nature of the Chemical Bond*, Cornell Univ. Press, Ithaca, New York, 3rd edition, 1960.

[38] C. Stampfl and C. G. Van de Valle, *Density functional calculations for III-V nitrides using the local density approximation and the generalized gradient approximation*, *Phys. Rev. B* **59**, 5521 (1999).

[39] DÁns-Lax, *Taschenbuch für Chemiker und Physiker, Band I, ed. by E. Lax and C. Synowietz*, Springer, Berlin, 1967.

[40] Kathrin Knese, *Magnetotransport an AlGaN/GaN-Heterostrukturen in hohen Magnetofeldern*, Master's thesis, TU Karolo Wilhelmina zu Braunschweig, 2006.

[41] S.-H. Wei, *III-nitride semiconductors for photovoltaic applications*, NCPV and Solar Program Review Meeting 2003, National Renewable Energy Laboratory, 1617 Cole Boulevard, Golden, Colorado 80401, USA, 1st edition, 2003.

[42] J. Furthmüller, P. H. Hahn, F. Fuchs, and F. Bechstedt, *Band structures and optical spectra of InN polimorphs: Influence of quasiparticle and excitonic effects*, *Phys. Rev. B* **B72**, 205106 (2005).

[43] M. Ueno, M. Yoshida, A. Onodera, O. Shimomura, and K. Takemura, *Stability of the wurtzite-type structure under high pressure: GaN and InN*, *Phys. Rev. B* **49**, 14 (1994).

[44] R. Juza and H. Hahn, *Über die Kristallstrukturen von Cu3N GaN und InN - Metallamide und metallnitride*, *Z. Anorg. Allg. Chem.* **244**, 111 (1940).

[45] K. Kubota, Y. Kobayashi, and K. Fujimoto, *Preparation and properties of III-V nitride thin films*, *J. Appl. Phys.* **66**, 2984 (1989).

[46] V. Cimalla, J. Pezoldt, G. Ecke, R. Kosiba, O. Ambacher, L. Spieß, G. Teichert, H. Lu, and W. J. Schaff, *Growth of cubic InN on r-plane sapphire*, *Appl. Phys. Lett.* **83**, 3468 (2003).

[47] J. Wu, W. Walukiewicz, K. M. Yu, J. W. Ager III, E. E. Haller, H. Lu, W. J. Schaff, Y. Saito, and Y. Nanishi, *Unusual properties of the fundamental band gap of InN*, *Appl. Phys. Lett.* **80**, 3967 (2002).

[48] T. Matsuoka, H. Okamato, and M. Nakao, *Growth of wurtzite InN in MOVPE and its optical characteristics*, *phys. stat. sol. (c)* **0**, 2806 (2003).

[49] J. Wu, W. Walukiewicz, K. M. Yu, J. W. Ager III, E. E. Haller, H. Lu, and W. J. Schaff, *Small band gap bowing in $In_{1-x}Ga_xN$ alloys*, *Appl. Phys. Lett.* **80**, 4741 (2002).

[50] V. Y. Davydov, A. A. Klochikhin, V. V. Emtsev, A. N. Smirnov, I. N. Goncharuk, A. V. Sakharov, D. A. Kurdyukov, M. V. Baidakova, V. A. Vekshin, S. V. Ivanov, J. Aderhold, J. Graul, A. Hashimoto, and A. Yamamoto, *Photoluminescence and Raman study of hexagonal InN and In-rich InGaN alloys*, *phys. stat. sol. (b)* **240**, 425 (2003).

[51] S. H. Wei, X. Nie, I. G. Batyrev, and S. B. Zhang, *Breakdown of the band-gap-common-cation rule: The origin of the small band gap of InN*, *Phys. Rev. B* **67**, 165209 (2003).

[52] S. H. Wei and A. Zunger, *Role of metal d states in II-VI semiconductors*, *Phys. Rev. B* **37**, 4958 (1988).

[53] T. V. Shubina, S. V. Ivanov, V. N. Jmeric, D. D. Solnishkov, V. A. Vekshin, P. S. Kopev, J. Leymarie A. Vasson, A. Kavokin, H. Amano, K. Shimono, A. Kasic, and B. Monemar, *Mie Resonances, Infrared Emission and the bandgap of InN*, *Phys. Rev. Lett.* **92**, 117407 (2004).

[54] O. Briot, B. Maleyre, S. Ruffenach, B. Gil, C. Pinquier, F. Demangeot, and J. Frandon, *Absorption and raman scattering processes in InN films and dots*, *J. Cryst. Growth* **269**, 22 (2004).

[55] B. Maleyre, S. Ruffenach, O. Briot, B. Gil, and A. van der Lee, *Investigation of the influence of buffer and nitrided layers on the initial stages of InN growth on sapphire by MOCVD*, *phys. stat. sol. (c)* **2**, 2309 (2005).

[56] R. Intartaglia, B. Maleyre, S. Ruffenach, O. Briot, T. Taliercio, and B. Gil, *Radiative and nonradiative recombination processes in InN films grown by metal organic chemical vapor deposition*, *Appl. Phys. Lett.* **86**, 142104 (2005).

[57] P. Specht, J. C. Ho, X. Xu, R. Armitage, E. R. Weber, R. Erni, and K. Kisielowsky, *Zincblende and wurtzite phases in InN epilayers and their respective band transitions*, *J. Cryst. Growth* **288**, 225 (2006).

[58] Christoph Cobet, *Linear optical properties of III-nitride semiconductors between 3 and 30 eV*, PhD thesis, TU Berlin, 2005.

[59] K. T. Tsen, C. Poweleit, D. K. Ferry, H. Lu, and W. J. Schaff, *Optical studies of high-field carrier transport of InN thick film grown on GaN*, *J. Cryst. Growth* **288**, 289 (2006).

[60] B. R. Nag, *Electron mobility in indium nitride*, *J. Cryst. Growth* **269**, 35 (2004).

[61] V. W. L. Chin, T. L. Tansley, and T. Osotchan, *Electron mobilities in gallium, indium, and aluminum nitrides*, *J. Appl. Phys.* **75**, 11 (1994).

[62] I. Mahboob, T. D. Veal, C. F. McConville, H. Lu, and W. J. Schaff, *Intrinsic Electron Accumulation at Clean InN Surfaces*, *Phys. Rev. Lett.* **92**, 036804 (2004).

[63] A. Laakso, J. Oila, A. Kemppinen, K. Saarinen, W. Egger, L. Liszkay, P. Sperr, H. Luc, and W. J. Schaff, *Vacancy defects in epitaxial InN: identification and electrical properties*, *J. Cryst. Growth* **269**, 41 (2004).

[64] H. Lu, W. J. Schaff, L. F. Eastman, and C. E. Stutz, *Surface charge accumulation of InN films grown by molecular-beam epitaxy*, *Appl. Phys. Lett.* **82**, 1736 (2003).

[65] K. A. Rickert, A. B. Ellis, F. J. Himpsel, H. Lu, W. Schaff, J. M. Redwing, F. Dwikusuma, and T. F. Kuech, *X-ray photoemission spectroscopic investigation of surface treatments, metal deposition, and electron accumulation on InN*, *Appl. Phys. Lett.* **82**, 3254 (2003).

[66] I. Mahboob, T. D. Veal, , F. J. Piper, C. F. McConville, H. Lu, W. J. Schaff, J. Furthmüller, and F. Bechstedt, *Origin of electron accumulation at wurtzite InN surfaces*, *Phys. Rev. B* **69**, 201307 (2004).

[67] V. Cimalla, G. Ecke, M. Niebelschütz, O. Ambacher, R. Goldhahn, H. Lu, and W. J. Schaff, *Surface conductivity of epitaxial InN*, *phys. stat. sol. (c)* **2**, 2254 (2005).

[68] R. Garcia, G. A. Hirata, M. H. Farias, and J. McKittrick, *A novel method for the synthesis of sub-microcrystalline wurtzite-type In(x)Ga(1-x)N powders*, *Mat. Sci. Eng.* **B90**, 7 (2002).

[69] A. G. Bhuiyan, A. Yamamoto, and A. Hashimoto, *A novel two-step method for improvement of MOVPE grown InN film on GaP(111)B substrate*, *phys. stat. sol. (b)* **228**, 27 (2001).

[70] A. G. Bhuiyan, A. Yamamoto, A. Hashimoto, and Y. Ito, *High temperature growth of InN on GaP(111)B substrate using a new two-step growth method*, *J. Cryst. Growth* **236**, 59 (2002).

[71] A. Yamamoto, Y. Yamauchi, M. Ohkubo, and A. Hashimoto, *A comparative study of OMVPE-grown InN heteroepitaxial layers on GaAs (111)B and α-Al_2O_3(0001) substrates*, *J. Cryst. Growth* **174**, 641 (1997).

[72] A. Yamamoto, M. Adachi, T. Arita, T. Sugiura, and A. Hashimoto, *A Comparative Study of MOVPE Growth of InN on GaAs(111) Substrates Using a Nitrided or Grown GaN Buffer Layer*, *J. Cryst. Growth* **176**, 595 (1999).

[73] A. Yamamoto, Y. Yamauchi, M. Ohkubo, A. Hashimoto, and T. Saitoh, *Heteroepitaxial growth of InN on Si(111) using a GaAs intermediate layer*, *Solid-State Electron.* **41**, 149 (1997).

[74] T. Ive, O. Brandt, M. Ramsteiner, M. Giehler, H. Kostial, and K. Ploog, *Properties of InN layers grown on 6H-SiC(0001) by plasma-assisted molecular beam epitaxy*, *Appl. Phys. Lett.* **84**, 1671 (2004).

[75] A. Yamamoto, T. Kobayashi, T. Yamauchi, M. Sasase, A. Hashimoto, and Y. Ito, *MOVPE InN on a 3c-SiC/Si(111) template formed by C+ ion implantation into Si(111)*, *phys. stat. sol. (c)* **2**, 2281 (2005).

[76] Y. Nanishi, Y. Saito, and T. Yamaguchi, *RF-molecular beam epitaxy growth and properties of InN and related alloys*, *Jpn. J. Appl. Phys.* **42**, 2549 (2003).

[77] A. G. Bhuiyan, A. Hashimoto, and A. Yamamoto, *Indium nitride (InN): A review on growth, characterisation and properties*, *J. Appl. Phys.* **94**, 2779 (2003).

[78] O. Ambacher, *Growth and applications of group III-nitrides*, *J. Phys.D: Appl. Phys.* **31**, 2653 (1998).

[79] S. Nakamura, *GaN growth using GaN buffer layer*, *Jpn. J. Appl. Phys.* **30**, L1705 (1991).

[80] S. Peters, T. Schmidtling, T. Trepk, U. W. Pohl, J.-T. Zettler, and W. Richter, *In-situ monitoring of GaN metal-organic vapor phase epitaxy by spectroscopic ellipsometry*, *J. Apl. Phys.* **88**, 4085 (2000).

[81] Torsten Schmidtling, *MOVPE growth and characterization of group III nitrides using in-situ spectroscopic ellipsometry*, PhD thesis, TU Berlin, 2005.

[82] T. Schmidtling, U. W. Pohl, W. Richter, and S. Peters, *In situ spectroscopic ellipsometry study of GaN nucleation layer growth and annealing on sapphire in metal-organic vapor-phase epitaxy*, *J. Appl. Phys.* **98**, 033522 (2005).

[83] O. Briot, B. Maleyre, and S. Ruffenach, *Optimization of the MOVPE growth of GaN on sapphire*, *Mat. Sci. Eng.* **B43**, 147 (1997).

[84] Markus Pristovsek, *Fundamental growth processes on different Gallium Arsenide surfaces in Metal-Organic Vapor Phase Epitaxy*, PhD thesis, TU Berlin, 2000.

[85] B. Maleyre, O. Briot, and S. Ruffenach, *MOVPE growth of InN films and quantum dots*, *J. Cryst. Growth* **269**, 15 (2004).

[86] M. Drago, C. Werner, M. Pristovsek, U. W. Pohl, and W. Richter, *Development of InN metalorganic vapor phase epitaxy using in-situ spectroscopic ellipsometry*, *Crys. Res. Technol.* **40**, 993 (2005).

[87] S. Yamaguchi, M. Kariya, S. Nitta, T. Takeuchi, C. Wetzel, H. Amano, and I. Akasaki, *Structural properties of InN on GaN grown by metalorganic vapor-phase epitaxy*, *J. Appl. Phys.* **85**, 7682 (1999).

[88] A. Yamamoto, N. Imai, K. Sugita, and A. Hashimoto, *Employment of a GaN buffer in the OMVPE growth of InN on sapphire substrates*, *J. Cryst. Growth* **261**, 271 (2004).

[89] A. Jain and J. M. Redwing, *Study of the growth mechanism and properties of InN films grown by MOCVD*, *Mat. Res. Soc. Symp. Proc.* **798**, Y12.8.1 (2004).

[90] H. Lu, W. J. Schaff, J. Wang, H. Wu, W. Yeo, A. Pharkya, and L. F. Eastman, *Improvement on epitaxial grown of InN by migration enhanced epitaxy*, *Appl. Phys. Lett.* **77**, 2548 (2000).

[91] K. Xu and A. Yoshikawa, *Effects of film polarities on InN growth by molecular-beam epitaxy*, *Appl. Phys. Lett.* **83**, 251 (2003).

[92] Andreas Able, *Untersuchungen zur metallorganischen Gasphasenepitaxie von Gruppe III Nitriden auf Silizium*, PhD thesis, Universitaet Regensburg, 2004.

[93] P. Vennéguès and B. Beaumont, *Transmission electron microscopy study of the nitridation of the (0001) sapphire surface*, *Appl. Phys. Lett.* **75**, 4115 (1999).

[94] T. Tsuchiya, H. Yamano, O. Miki, A. Wakahara, and A. Yoshida, *Improvement of the Crystalline Quality of InN Layers Grown on Sapphire (0001) by Surface Nitridation*, *Jpn. J. Appl. Phys.* **38**, 1884 (1999).

[95] T. Schmidtling, M. Drago, U. W. Pohl, and W. Richter, *Spectroscopic ellipsometry during metalorganic vapor phase epitaxy of InN*, *J. Cryst. Growth* **248**, 523 (2003).

[96] O. Ambacher, M. S. Brandt, R. Dimitrov, T. Metzger, M. Stutzmann, R. a: Fischer, A. Miehr, A. Bergmaier, and G. Dollinger, *Thermal stability and desorption of Group III nitrides prepared by organic chemical vapour deposition*, *jovstb* **14**, 3532 (1996).

[97] Q. Guo, O. Kato, and A. Yoshida, *Thermal stability of indium nitride single crystal films*, *J. Appl. Phys.* **73**, 7969 (1993).

[98] Olivier Briot in, *Group III nitride semiconductor compounds - physics and applications*, Oxford science publications, ed. by B. Gil, 1st edition, 1997.

[99] R. M. Graham, A. C. Cones, N. J. Mason, S. Rushworth, A. Salesse, T. Y. Seong, G. Booker, L. Smith, and P. J. Walker, *Improved materials fro MOVPE growth of GaAs and InSb*, *Sem. Sci. and Tech.* **8**, 1797 (1993).

[100] Kolja Haberland, *Optical in-situ studies during metal-organic vapor phase epitaxy with respect to III-V device production*, PhD thesis, TU Berlin, 2002.

[101] K. Haberland, A. Kaluza, M. Zorn, M. Pristovsek, H. Hardtdegen, M. Weyers, J.-T. Zettler, and W. Richter, *Real-time calibration of wafer temperature, growth rate and composition by optical in-situ techniques during $Al_xGa_{(1-x)}As$ growth in MOVPE*, *J. Cryst. Growth* **240**, 87 (2002).

[102] S. Keller, I. Ben-Yaacov, P. Denvers, and U. K Mishra, *Proceedings of the IWNS2000-Nagoya, Japan, September 24-27, 2000, IPAP conference series*, *Proc. Int. Workshop on Nitride Semiconductors (IWN2000), IPAP Conf. Series* **1**, 233 (2000).

[103] A. Yamamoto, Y. Murakami, K. Koide, M. Adachi, and A. Hashimoto, *Growth temperature dependences of MOVPE InN on sapphire substrates*, *phys. stat. sol. (b)* **228**, 5 (2001).

[104] F.-H. Yang, J.-S. Hwang, Y.-J. Yang, K.-H. Chen, and J.-H. Wang, *Growth of High-Quality Epitaxial InN Film with High-Speed Reactant Gas by Organometallic Vapor-Phase Epitaxy*, *Jpn. J. Appl. Phys.* **41**, L1321 (2002).

[105] K. Sugita, H. Takatsuka, A. Hashimoto, and A. Yamamoto, *Photoluminescence and optical absorption edge for MOVPE-grown InN*, *phys. stat. sol. (b)* **240**, 421 (2003).

[106] A. Yamamoto, K. Sugita, H. Takatsuka, A. Hashimoto, and V. Y. Davydov, *Correlations between electrical and optical properties for OMVPE InN*, *J. Cryst. Growth* **261**, 275 (2004).

[107] M. Drago, T. Schmidtling, U. W. Pohl, S. Peters, and W. Richter, *InN metalorganic vapour phase epitaxy and ellipsometric characterisation*, *phys. stat. sol. (c)* **0**, 2842 (2003).

[108] A. Jain, S. Raghavan, and J. M. Redwing, *Evolution of surface morphology and film stress during MOCVD growth of InN on sapphire substrates*, *J. Cryst. Growth* **269**, 128 (2004).

[109] A. Yamamoto et al., *Poster presented at the International Conference of Nitride Semiconductors-6, Bremen (2005). Unpublished.*

[110] C. H. Swartz, R. P. Tomkins, T. H. Myers, H. Lu, and W. J. Schaff, *Demonstration of nearly non degenerate electron conduction in InN grown by Molecular Beam Epitaxy*, *phys. stat. sol. (c)* **2**, 2250 (2005).

[111] R. E. Jones, K. M. Yu, S. X. Li, W. Walukiewicz, J.W. Ager, E. E. Haller, H. Lu, and W. J. Schaff, *Evidence for p-Type Doping of InN*, *Phys. Rev. Lett.* **96**, 125505 (2006).

[112] Thorsten Wethkamp, *Optical properties of group-III-nitrides in the visible to vacuum-ultraviolet spectral range investigated by spectroscopic ellipsometry*, PhD thesis, TU Berlin, 1999.

[113] D. Huang, P. Visconti, M. A. Reshchikov, F. Yun, T. King, A. A. Baski, C. W. Litton, J. Jasinski, Z. Liliental-Weber, and H. Morkoç, *Polarity of GaN grown on sapphire by molecular beam epitaxy with different buffer layers*, *phys. stat. sol. (a)* **188**, 571 (2001).

[114] A. Munkholm, C. Thompson, C. M. Foster, J. A. Eastman, O. Auciello, G. B. Stephenson, P. Fini, S. .P DenBaars, and J. S. Speck, *Determination of the cubic to hexagonal fraction in GaN nucleation layers using grazing incidence x-ray scattering*, *Appl. Phys. Lett.* **72**, 2972 (1998).

[115] E. Kurimoto, M. Hangyo, H. Harima, M. Yoshimoto, T. Yamaguchi, T. Araki, Y. Nanishi, and K. Isoda, *Spectroscopic observation of oxidation process in InN*, *Appl. Phys. Lett.* **84**, 212 (2004).

[116] M. Drago, P. Vogt, and W. Richter, *MOVPE growth of InN with ammonia on sapphire*, *phys. stat. sol. (a)* **203**, 116 (2006).

[117] A. Koukitu, T. Taki, N. Takahashi, and H. Seki, *Thermodynamic study on the role of hydrogen during the MOVPE growth of group III nitrides*, *J. Cryst. Growth* **197**, 99 (1999).

[118] K.M. Yu, Z. Liliental-Weber, W. Walukiewicz, W. Shan, J. W. Ager III, S. X. Li, R. E. Jones, E. E. Haller, H. Lu, and W. J. Schaff, *On the crystalline structure, stoichiometry and bandgap of InN thin films*, *Appl. Phys. Lett.* **86**, 071910 (2005).

[119] P. Ruterana, M. Morales, F. Gourbilleau, P. Singh, M. Drago, T. Schmidtling, U. W. Pohl, and W. Richter, *Effects of the low temperature buffer and annealing on the properties of InN layers grown by MOVPE*, *phys. stat. sol. (a)* **202**, 781 (2005).

[120] S. Keller, B. P. Keller, Y. F. Wu, B. Heying, D. Kapolnek, J. S. Speck, U. K. Mishra, and S. P. DenBaars, *Influence of sapphire nitridation on properties of GaN grown by metal organic chemical vapor deposition*, *Appl. Phys. Lett.* **68**, 1525 (1996).

[121] K.S. Kim, K.Y Lim, and H.J. Lee, *The effects of nitridation on properties of GaN grown on sapphire substrate by metal-organic chemical vapour deposition*, *Sem. Sci. and Tech.* **14**, 557 (1999).

[122] T. Hashimoto, Y. Terakoshi, M. Yuri, M. Ishida, O. Imafuji, T. Sugino, and K. Itoh, *Quantitative study of nitridated sapphire surfaces by x-ray photoelectron spectroscopy*, *J. Appl. Phys.* **86**, 3670 (1999).

[123] T. Hashimoto, Y. Terakoshi, M. Ishida, M. Yuri, O. Imafuji, T. Sugino, A. Yoshikawa, and K. Itoh, *Structural investigation of sapphire surface after nitridation*, *J. Cryst. Growth* , 254 (1998).

[124] Y.-C. Pan, W. Lee, C. Shu, H. Lin, C. Chiang, H. Chang, D. Lin, M. Lee, and W. Chen, *Influence of Sapphire Nitridation on Properties of InN Prepared by Metalorganic Vapor Phase Epitaxy*, *Jpn. J. Appl. Phys.* **38**, 645 (1999).

[125] J. M. Bennett and L. Mattson, *Introduction to Surface Roughness and Scattering*, Optical Society of America, Washington D.C., 1989.

[126] L. X. Benedict, T. Wethkamp, K. Wilmers, C. Cobet, N. Esser, E. L. Shirley, W. Richter, and M. Cardona, *Dielectric function of wurtzite GaN and AlN thin films*, *Sol. State Commun.* **112**, 129 (1999).

[127] W. Sellmeier, *Ueber die durch die Aetherschwingungen erregten Mitswingungen der Körpertheilchen und deren Rückwirkung auf die ersteren, besonders zur Erklärung der Dispersion und ihrer Anomalien*, *Ann. Phys.* **147**, 3292 (1872).

[128] K. Uchida, A. Watanabe, F. Yano, M. Kouguchi, M. Tanaka, and S. Minagawa, *Nitridation process of sapphire substrate surface and its effect on the growth of GaN*, *J. Appl. Phys.* **79**, 3487 (1996).

[129] Fernando Ponce in:, *Group III nitride semiconductor compounds - physics and applications*, Oxford science publications, ed. by B. Gil, 1st edition, 1997.

[130] K. Fleischer, M. Toth, M. R. Phillips, J. Zou, G. Li, and S. J. Chua, *Depth profiling of GaN by cathodoluminescence microanalysis*, *Appl. Phys. Lett.* **74**, 1114 (1999).

[131] J. Wu, W. Walukiewicz, W. Shan K. M Yu, J. W. Ager III, E. E Haller, H. Lu, W. J. Schaff, Y. Saito, and Y. Nanishi, *effects of the narrow band gap on the properties of InN*, *Phys. Rev. B* **66**, 201403 (2002).

[132] M.R. Phillips, M.H. Zareie, Gelhausen, M. Drago, T. Schmidtling, and W. Richter, *Scanning tunneling and cathodoluminescence spectroscopy of indium nitride*, *J. Cryst. Growth* **269**, 106 (2004).

[133] K. Y. Koyama, N. V. Smith, and W. E. Spicer, *Optical properties of Indium*, *Phys. Rev. B* **8**, 2426 (1973).

[134] P. Lautenschlager, M. Garriga, S. Logothedis, and M. Cardona, *Interband critical points of GaAs and their temperature dependence*, *prb* **35**, 9174 (1987).

[135] R. Goldhahn, S. Shokhovets, V. Cimalla, L. Spiess, G. Ecke, O. Ambacher, J. Furthmüller, F. Bechstedt, H. Lu, and W. J. Schaff, *Dielectric function of "narrow"band gap InN*, *Mat. Res. Soc. Symp. Proc.* **743**, L.5.9.1 (2003).